Experimental and numerical study of reference standards for fatigue cracks using eddy current NDE

by

Steven Gerard Ross

A Thesis Submitted to the

Graduate Faculty in Partial Fulfillment of the

Requirements for the Degree of

MASTER OF SCIENCE

Department: Electrical Engineering and Computer Engineering
Major: Electrical Engineering

Signatures have been redacted for privacy

Signatures have been redacted for privacy

Iowa State University
Ames, Iowa

1992

TABLE OF CONTENTS

LIST OF SYMBOLS

A	Magnetic vector potential	Weber/m
a.c.	alternating current	
B	Magnetic flux density	Tesla (Weber/m^2)
D	Electric flux density	Coloumb/m^2
E	Electric field intensity	Volt/m
f	frequency	Hertz
H	Magnetic field intensity	Ampere/m
J	Current density	Ampere/m^2
σ	Electrical conductivity	mhos/m
μ	Magnetic permeability	Henry/m
ε	Permittivity	Farad/m

ACKNOWLEDGEMENTS

I would like to express my most sincere thanks to my advisor Dr. William Lord. He has introduced me to the field of nondestructive testing which I find fascinating and rewarding. Since I first started working with Dr. Lord he has guided me and always kept me enthusiastic in my studies. He has been a great influence on me both as a friend and an advisor. I am very grateful for all he has done for me and I am excited about working with him in the coming years.

I would also like to thank the members of my committee, Dr. Lalita Udpa, Dr. Satish Udpa, and Dr. Tom Rudolphi. They have always been more than willing to spend time with me and offer advice when I drop by unexpectedly. Their guidance was essential to the ideas studied in this thesis.

I would like to give a special thanks to Shridhar Nath who spent many hours giving me assistance, advice and encouragement over the past year and a half. Without his assistance this study would have undoubtably been a much more difficult task.

I would like to thank the staff of Ames Laboratory who have been generous in letting me use their machining equipment. I would especially like to thank Dr. Tom Lograsso who took the time to help me prepare the EDM notches. I would like to thank the people in Mechanical Engineering, especially Gay Scandrett, who was very helpful with the generation of fatigue cracks. I would also like to thank Dr. Bill Larson and Dr. John Patterson for spending time with me in analyzing the fatigue cracks.

Finally, I would like to thank NASA Langley for the financial support which made this research possible.

ABSTRACT

Nondestructive testing (NDT) has been used for many years to detect fatigue cracks in structures such as airplanes and nuclear power plants. A major application is detecting fatigue cracks in tubing units such as heat exchangers and steam generators. One method of NDT particularly effective in detecting fatigue cracks is eddy current testing. Eddy current NDT is very effective in testing conducting materials because it is very sensitive to small defects. One drawback to the eddy current method is that it is difficult to classify defects once they are detected. This is because eddy current phenomena are governed by diffusion effects rather than wave effects and are thus difficult to image. Thus, when an eddy current response is obtained it must be compared to a reference standard to determine what type of defect induced that response.

The reference standard is used to determine if the eddy current response is obtained from a defect and if so, the type and size of defect. Thus, it is critical that the reference standard be accurate and reliable. Often reference standards for fatigue cracks are produced from electrical discharge machined (EDM) notches. However, there has been much disagreement as to the accuracy of EDM notches to fatigue cracks. Another method which can be used to obtain data for reference standards is a numerical model. This thesis investigates the eddy current responses of fatigue cracks in thin-walled stainless steel tubing and compares them to EDM notches and a two-dimensional numerical finite element model. This thesis also introduces a finite element method for modeling a fine crack by an adaptation of the finite element formulation.

The results of this study show that EDM notches give similar responses to some fatigue cracks. However, eddy current fatigue crack responses in thin-walled tubing are very sensitive to crack path and microcracking associated with the crack. Thus, these factors need to be taken into account when determining a reference standard from an EDM notch. The finite element model was found to be an accurate means of simulating fatigue cracks, however, since it is a two-dimensional model the type of fatigue cracks it can simulate are limited.

CHAPTER 1. INTRODUCTION

A. Background

Today the reliability of structures such as airplanes, bridges and nuclear power plants is critical to human life. Though safe operation is often taken for granted, with today's complex structures it is important that we are assured of a product's reliability. In the past a method of testing the reliability of a product was to push the product to a certain critical stage to see if failure ensued. The obvious drawback to this method is that the product must be destroyed or at least damaged in the test. An alternative method of testing is known as nondestructive testing where the integrity of the product is not impaired. The field of nondestructive testing (NDT) has come to the forefront in industry for the following reasons: [1]

1. To ensure product reliability.
2. To prevent accidents and save human life.
3. To make a profit for the user.
    a. To ensure customer satisfaction.
    b. To aid in better product design.
    c. To lower manufacturing costs.
    e. To maintain a uniform quality level.

There are many methods of NDT which are used effectively in industry such as radiation, ultrasonic, magnetic particle, liquid penetrant and

electromagnetic tests. The main idea in all of the tests is to induce energy in the test specimen that can then be interpreted without causing damage to the specimen. The NDT method used in the research discussed here is known as eddy current (ET) NDT which is an electromagnetic method.

B. Motivation

The motivation and funding for this research was brought about by the need for the automated nondestructive testing of the space shuttle main engine (SSME) heat exchanger unit. The unit is used to transport liquid oxygen through the intense heat of the engine chamber. It consists of 316L stainless steel tubing with 0.330″ I.D. and 0.0265″ wall thickness and other tubing with 0.190″ ID and 0.0125″ wall thickness. A diagram of the heat exchanger unit is shown in Figure 1.1 with a close-up of the tubing used in Figure 1.2. One particular application of ET has been for the testing of metal tubing [3-4] and in particular heat exchangers [5-6]. The NASA SSME heat exchanger project involves an artificial intelligence neural network classification scheme to categorize defects in the heat exchanger tubing. The neural network is a means of classifying defects with a backpropagation network as shown in Figure 1.3. The weights used in the backpropagation scheme are iterated until they converge on optimum values. A critical part of the iteration process is the acquisition of training data from various types of defects. The purpose of this study is to find a reliable and accurate means of simulating fatigue cracks in stainless steel tubing which can then be used as training data for the neural network.

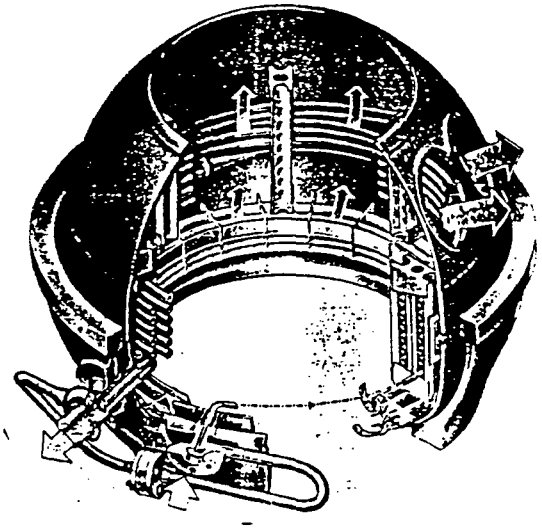

Figure 1.1. Space Shuttle Main Engine Heat Exchanger Unit [2].

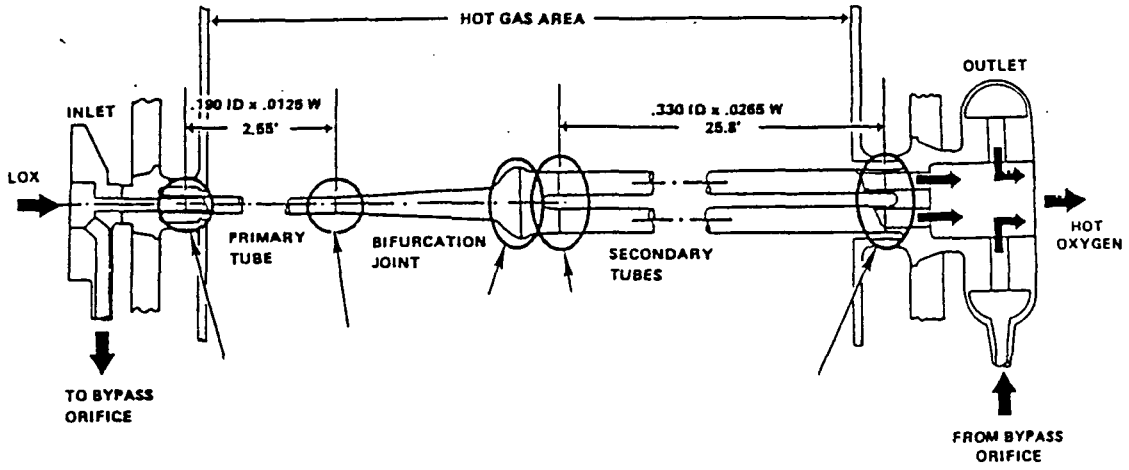

Figure 1.2. Heat exchanger tubing [2].

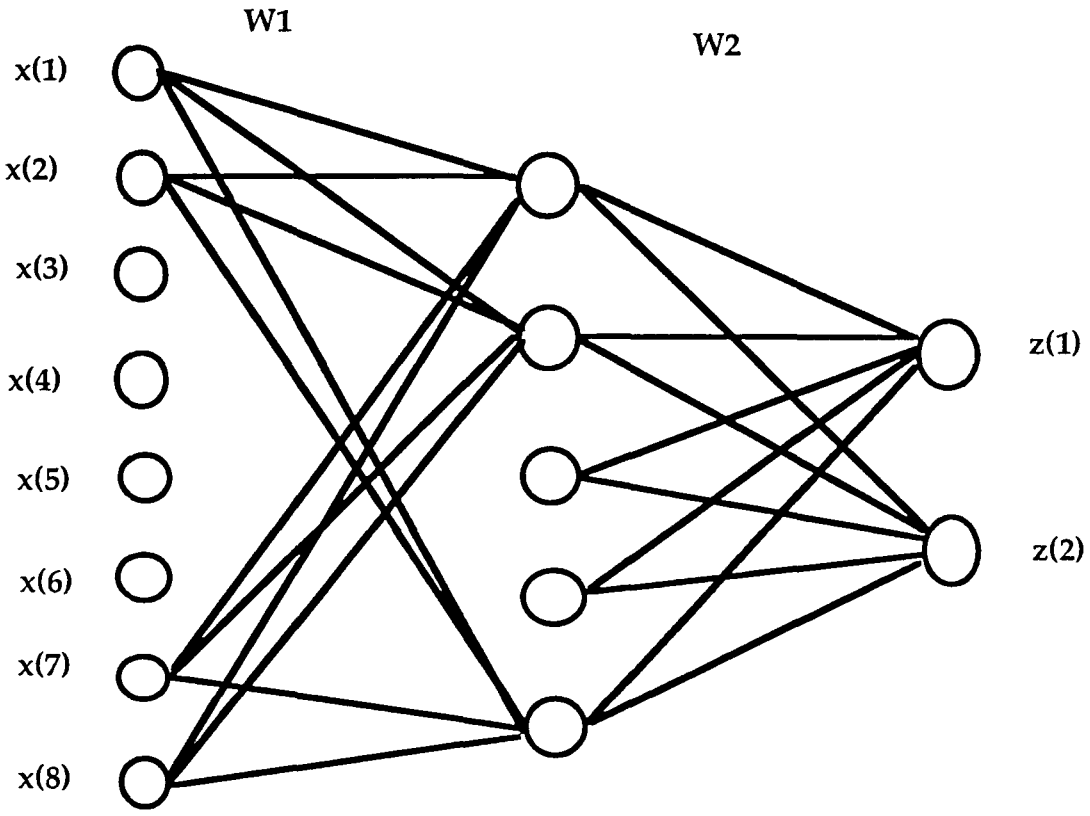

Figure 1.3. Neural Network

C. Eddy Current NDT

The eddy current technique has been used for many years in nondestructive testing and there are many excellent references pertaining to the basic principles and applications [7-9]. The basic underlying principle of eddy current NDT involves placing a conducting specimen in a varying ac field. The test is usually conducted at relatively low frequencies (less than 2 Mhz) and is governed by the diffusion equation rather than the wave equation, i.e., the process does not constitute a wavefront travelling, but rather a current decaying.

When the a.c. field interacts with the test specimen, eddy currents are induced in the opposite direction to that of the primary excitation current, according to Lenz's law. In this study the excitation device is an internal differential probe.

The theory of the differential probe has been studied extensively [10]. A diagram of a typical differential probe is shown in Figure 1.4. The differential probe consists of two coils each carrying opposing a.c. current. The coils create magnetic fields which induce currents in a test object. These induced currents are known as eddy currents and in turn affect the impedance of the coils. The impedance of the two coils can then be balanced as in a typical bridge circuit. If there is any disruption to the eddy currents the impedance between the two coils will be altered. This impedance change could be caused by any disruption in current flow such as a flaw, inclusion, wall thinning or a conducting support plate. This impedance change is then traced out on an eddyscope as shown in Figure 1.5. This impedance trace is known as an impedance plane trajectory (IPT). The vertical axis of the IPT is reactance, with the horizontal axis being resistance. Depending on the type of defect a unique size and shape IPT is traced out.

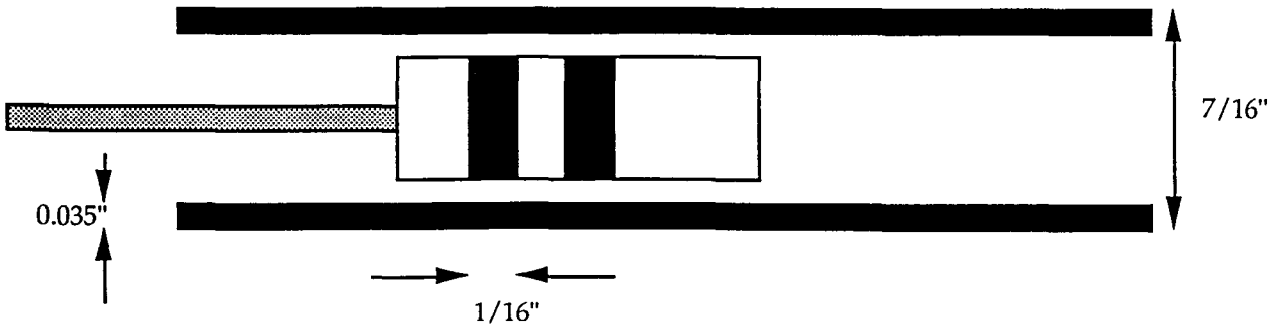

Figure 1.4. Differential probe in stainless steel tubing.

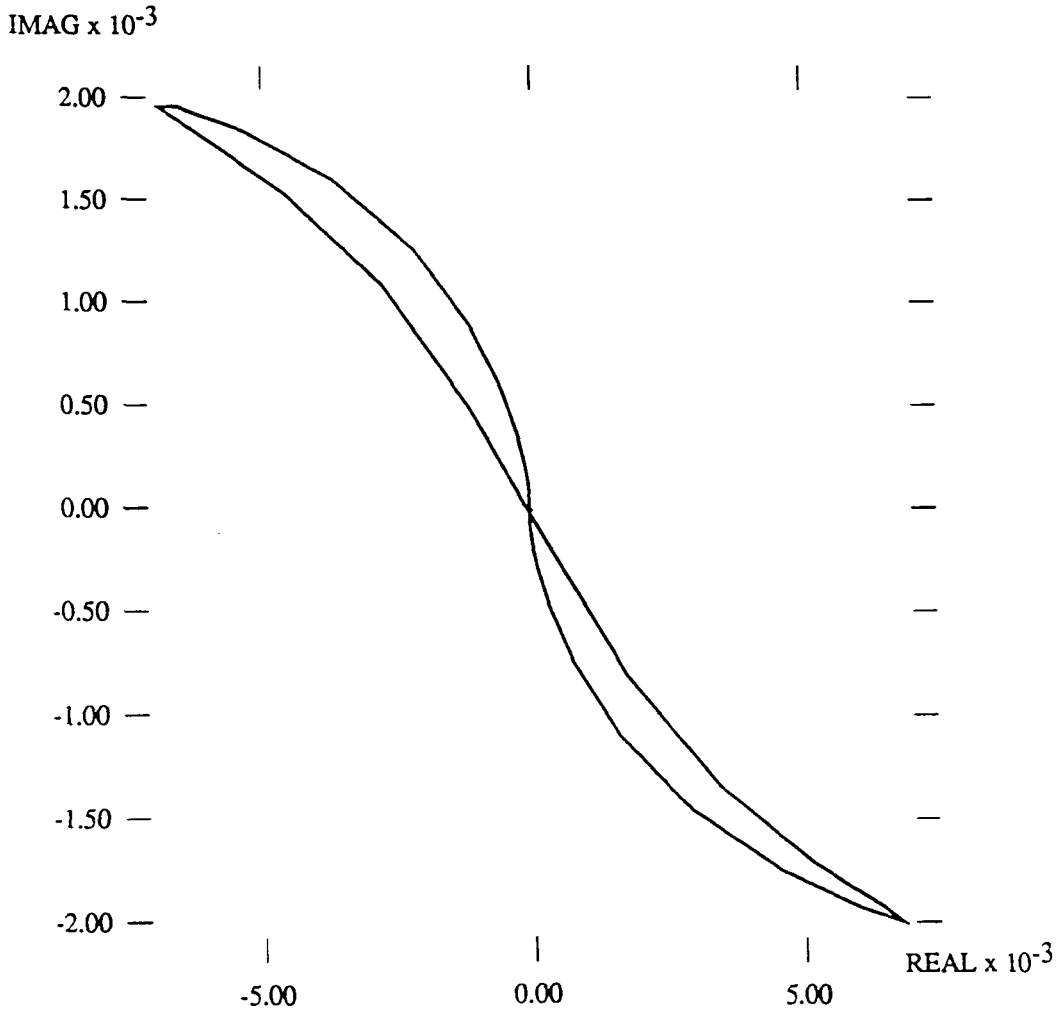

Figure 1.5. Example of a impedance plane trajectory with normalized reactance on the vertical axis and normalized resistance on the horizontal axis.

The current is at a peak value on the inside diameter of the tube when an internal probe is used. In the simplest analytical model of eddy current effect the current then decays exponentially into the tube according to

$$J_r = J_o \exp(-x\sqrt{\Pi f \mu \sigma}) \tag{1.1}$$

where J_o is the eddy current density at the inside diameter of the tube, σ is the conductivity of the tube, μ is the permeability of the tube ($\mu = \mu_0$ for stainless steel), and f is the frequency of the probe. The eddy current disruption is generally larger for defects which cause more current interrupt. This implies that a circumferential defect will cause very little current to be disrupted compared to the amount of current disrupted by an axial defect. This is because the eddy currents produced are circumferential around the tube. This has been used by many researchers as support to the claim that small circumferential defects are impossible to detect with probes which produce circumferential eddy currents [11].

The differential equation governing eddy current phenomena in conducting materials can be derived from Maxwell's equations listed below.

$$\nabla x \overline{H} = \sigma \overline{E} + \frac{\partial \overline{E}}{\partial t} \tag{1.2}$$

$$\nabla x \overline{E} = -\frac{\partial \overline{B}}{\partial t} \tag{1.3}$$

$$\nabla \cdot \overline{D} = \rho_v \tag{1.4}$$

$$\nabla \cdot \overline{B} = 0 \tag{1.5}$$

where the constitutive relationships are

$$\overline{D} = \varepsilon \overline{E} \tag{1.7}$$

and

$$\overline{B} = \mu \overline{H} \tag{1.8}$$

Also, the current density is given as

$$\overline{J} = \sigma \overline{E} \tag{1.9}$$

Magnetic vector potential can now be defined as

$$\nabla \times \overline{A} = \overline{B} = \mu \overline{H} \tag{1.10}$$

then substituting into equation 1.4 gives

$$\nabla \times \overline{E} = -\nabla \times \frac{\partial \overline{A}}{\partial t} \tag{1.11}$$

which gives

$$\overline{E} = -\frac{\partial \overline{A}}{\partial t} - \nabla \phi \tag{1.12}$$

where ϕ is the electric scalar potential. Next, using equation 1.9, equation 1.12 becomes

$$\bar{J} = -\sigma\frac{\partial\overline{A}}{\partial t} + \bar{J}_s \tag{1.13}$$

where

$$J_s = -\sigma\,\nabla\cdot\phi$$

Thus, equation 1.2 becomes

$$\frac{1}{\mu}\left(\nabla \times \nabla \times \overline{A}\right) = \bar{J}_s - \sigma\frac{\partial\overline{A}}{\partial t} \tag{1.14}$$

using Stokes' theorem

$$\nabla \times \nabla \times \overline{A} = -\nabla^2\overline{A} + \nabla\left(\nabla\cdot\overline{A}\right) \tag{1.15}$$

and

$$\nabla\cdot\overline{A} = 0 \tag{1.16}$$

equation 1.14 becomes

$$\frac{1}{\mu}\nabla^2\overline{A} = -\bar{J}_s + \sigma\frac{\partial\overline{A}}{\partial t} \tag{1.17}$$

using phasor notation where

$$\frac{\partial}{\partial t} = j\omega \tag{1.18}$$

results in the diffusion equation for eddy current phenomena as

$$\frac{1}{\mu}\nabla^2\bar{A} = -\bar{J}_s + j\omega\sigma\bar{A} \tag{1.19}$$

This analysis assumes that the material permeability μ is that of free space μ_0, and the material conductivity σ is that of 316L stainless steel.

D. Geometry of EC Test

For this study a differential eddy current probe was used to detect defects in stainless steel tubing. Since the actual heat exchanger unit could not be used similar stainless steel tubing samples were obtained to simulate the heat exchanger tubing. The 316L stainless steel samples had an outer diameter of 7/16" and a wall thickness of 0.035". An internal differential eddy current probe was used as shown in Figure 1.4. The probe has an outer diameter of 0.33" and a coil thickness of .0625". The geometry is completely axisymmetric which is beneficial for numerical modeling.

E. Fatigue Crack Detection

One important use of EC testing is for the detection of fatigue cracks in metal [12-14]. When testing a specimen it is crucial to not only find the crack, but also to determine just how large the fatigue crack in question is. The presence of a fatigue crack does necessarily imply that the structure will fail [15]. It is more important to monitor the fatigue crack to observe if any growth is taking place. Then, if the crack is growing, it is crucial to know when it reaches the point where the structure is no longer safe to operate. This is the true essence of nondestructive testing which involves both detection and classification of the fatigue crack into a safe or unsafe category.

F. Reference Standards

To determine if a defect has reached a critical stage, a certain threshold or standard must be used as a guideline. If the response from the impedance plane is greater than or less than this certain threshold, the defect can usually be properly categorized. This threshold or guideline for defect detection is obtained from previous impedance plane trajectory data. Ideally, a researcher could use data acquired from previous defects that occurred through actual structural wear from normal operation. This, however, would obviously require many defective structures which are usually difficult to acquire, in large part because most structures are safe. For example, in the SSME heat exchanger unit there have thus far been no defects detected, so acquiring a threshold for the detection

of defects would be an extremely difficult task if one were limited to the use of operational structures only.

This limitation can be overcome through two methods. One is by acquiring data from similar defects which are machined in samples of similar geometry. Another is by modeling on a computer the defect and geometry in consideration. These can then be used to gain access to an accurate reference standard. When used together the two methods can be even more powerful because they can be used for natural verification. The computer model is particularly effective because with it one can not only observe the impedance plane trajectory, but one can also look at the field/defect interactions, thus gaining insight into the physics of the problem. Using these two methods, reference standards can be obtained and used to determine how severe a defect is. This is of vital importance in nondestructive testing [16].

G. EDM Notches

One method of obtaining reference standards for fatigue cracks is through the use of electrical-discharge-machined (EDM) [17-18] defects. Although they have been used widely for automated classification in nondestructive testing [19-21] there is disagreement as to their effectiveness as a true reference standard [22-23]. For example, Hagaimier [24] has implied that EDM notches and fatigue cracks give very similar eddy current responses and thus, EDM notches can be used as a reference standard for fatigue cracks. Rummel and Moulder [25], on other hand, say that because of the large volume of EDM notches they give larger eddy current responses than fatigue cracks and this must be taken into account

when using an EDM notch as a reference standard. It should be noted that these two studies were performed with a probe over a flat block while this study considers a probe inside a tube. Thus, the results of this study should not necessarily be compared to the results of references 24 and 25 which were cited as an example of how EDM notches and fatigue cracks are viewed by the research community.

H. Numerical Modeling

Numerical modeling of electromagnetic NDT phenomena is a process developed in the last decade [26-27]. It has been used in NDE to study field/defect interactions. Such numerical simulations can be used to gain physical insight of a problem which could not be obtained from an experimental study alone. Another advantage of numerical simulation is that it is a simple process to model different defects or to alter the defect being simulated. It has been shown that the finite element numerical model gives results similar to those obtained experimentally [28].

I. Scope of Thesis

The scope of this these is to investigate an accurate reference standard for fatigue cracks in stainless steel tubing. This involves using experimental EDM notches and a numerical finite element code to produce signals similar to those obtained from fatigue cracks. One motivation is to determine what kind of IPTs growing fatigue cracks give in stainless steel tubing.

This task was accomplished by first preparing fatigue cracks in thin walled (t<<d) stainless steel tubing. The eddy current responses to these fatigue cracks was determined and recorded. Next, EDM notches were prepared in identical stainless steel tubing. Then, the eddy current responses were analyzed to determine how fatigue crack and EDM notch signals compare in stainless steel tubing. Along with this experimental procedure a two-dimensional numerical finite element model was used to model eddy current fatigue crack responses.

This study addresses the problem of whether EDM notches and fatigue cracks have similar eddy current responses in stainless steel tubing. It also investigates how well the predicted IPTs from a two-dimensional axisymmetric numerical model compare to actual three-dimensional fatigue cracks.

CHAPTER 2. NUMERICAL MODELING

A. Introduction

Numerical modeling is being used increasingly in NDE studies as a forward model to predict field/defect interactions. A forward model can be an excellent way to gain insight into the expected fields associated with any given defect. Analytical approaches which could be expected to model field/defect interactions have proven to be very cumbersome, as boundary conditions are imposed on the problem. A viable alternative to the analytical solution is one obtained using numerical methods of computing [29-31]. With the continuing advances in computer speed and memory capability, numerical models are able to handle complex geometries and defects which earlier could not be considered. In this chapter a numerical method known as the finite element method is discussed.

B. The Finite Element Method

1. Introduction

The numerical method used for this study is the finite element method [32-34]. Finite element modeling grew in importance through its use in solid mechanics [35] and fluid mechanics [36]. It has only been in the last decade that finite element modeling gained wide use in electromagnetic methods of

nondestructive testing. Much of the pioneering work in the area of electromagnetic NDT was done by Lord and associates [37-41].

2. Governing Equations

In modeling electromagnetic phenomena, and particularly eddy current phenomena, the Poisson's equation for quasi static excitation can be derived from Maxwell's equations as:

$$\frac{1}{\mu}\nabla^2\overline{A} = -\bar{J} + j\omega\sigma\overline{A} \tag{2.1}$$

where μ is the permeability, $\overline{A}$ is the magnetic vector potential, $\bar{J}$ is the applied excitation current density, ω is the excitation angular frequency and σ is the material conductivity. For an axisymmetric geometry equation 2.1 reduces to

$$\frac{1}{\mu}\left(\frac{\partial^2\overline{A}}{\partial r^2} + \frac{1}{r}\frac{\overline{A}}{r} + \frac{\partial^2\overline{A}}{\partial z^2} - \frac{\overline{A}}{r^2}\right) = -\bar{J} + j\omega\sigma\overline{A} \tag{2.2}$$

where r is associated with the cylindrical coordinate axis system of Figure 2.2.

3. Energy Functional

Mathematically, finite element analysis can be understood as the minimization of an energy functional associated with a particular governing equation. The

energy functional associated with the Poisson's governing equation is

$$F = \int \int_R \left[\frac{1}{2\mu} \left\{ \left| \frac{\partial \overline{A}}{\partial z} \right|^2 + \left| \frac{\partial \overline{A}}{\partial r} + \frac{\overline{A}}{r} \right|^2 \right\} + \frac{j\omega\sigma}{2} |\overline{A}|^2 - \overline{J} \cdot \overline{A} \right] r \, dr \, dz \qquad (2.3)$$

where the first term corresponds to the energy of the magnetic field, the second term corresponds to the eddy currents, and the third term corresponds to the source [43].

C. Finite Element Procedure

Although there are different approaches to finite element modeling the Ritz method which is a derivative of variational calculus is used in this finite element formulation. The steps followed in a finite element formulation are from [34]

1. Discretization
2. Interpolation
3. Elemental formulation
4. Assembly
5. Constraints
6. Solution
7. Computation of derived or secondary variables.

1. Discretization

The first step in developing a finite element model involves discretizing the region to be modeled. A typical two-dimensional discretization scheme using triangular elements is shown in Figure 2.1. In creating a mesh it is desirable to take advantage of any symmetry which can be incorporated into the problem. For the case of a tubular geometry it is possible to reduce the number of dimensions from three to two if complete axisymmetry is assumed as shown in Figure 2.2. The resulting two-dimensional axisymmetric mesh is shown in Figure 2.3. When modeling very fine fatigue cracks, discretization becomes more difficult because of the need for a fine mesh in the crack region. The mesh generation is discussed in greater detail later in this chapter.

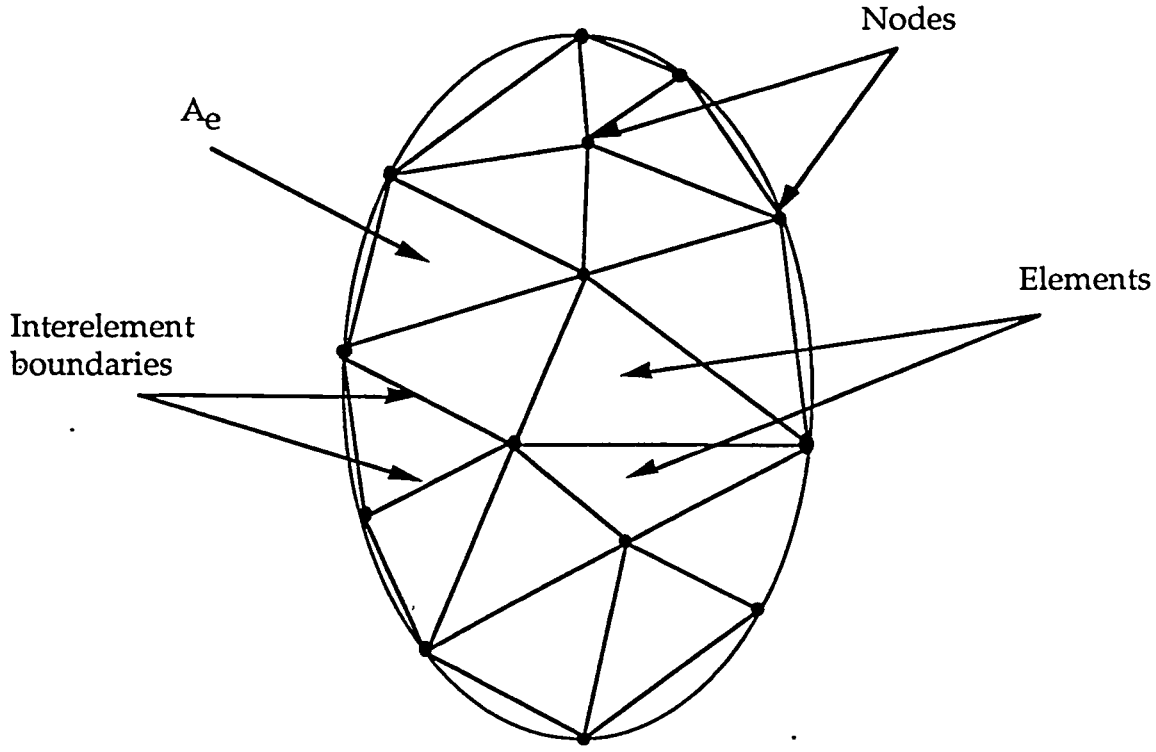

Figure 2.1. Typical two-dimensional finite element mesh.

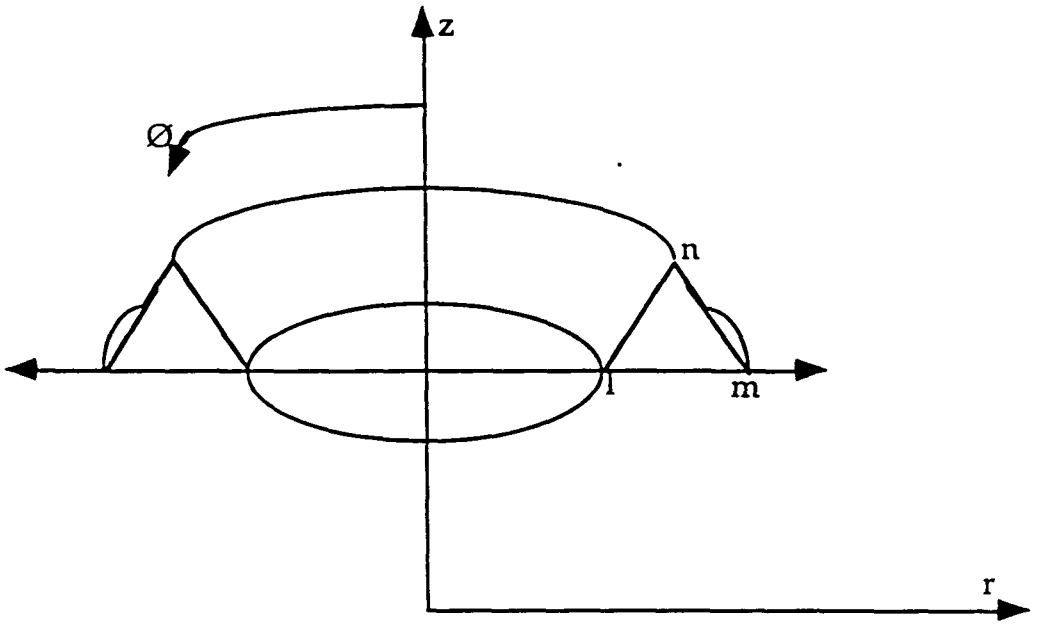

Figure 2.2. Axisymmetric region with element lmn.

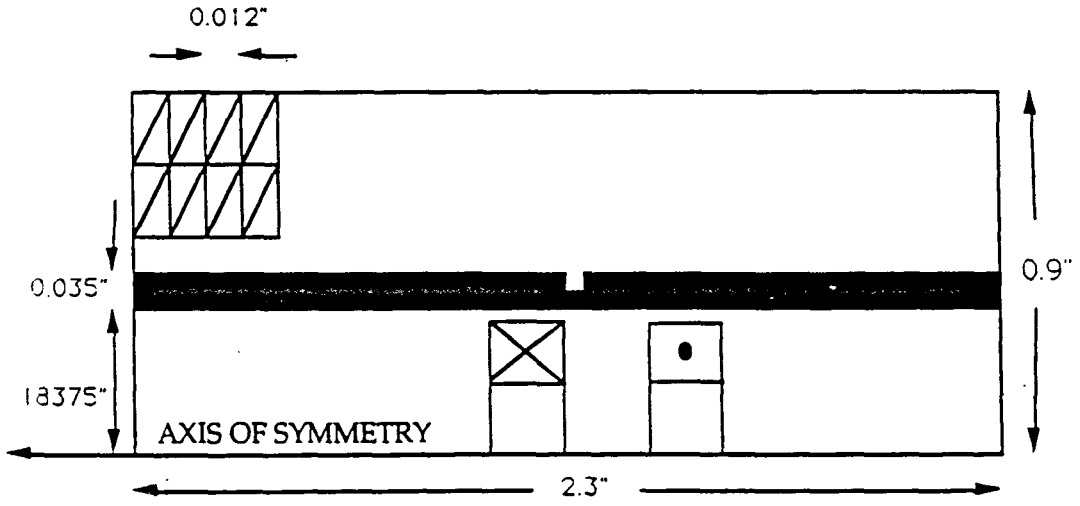

Figure 2.3 Axisymmetric Mesh.

2. Interpolation

The process of interpolation involves obtaining solution surfaces which represent the element. The most elementary type of interpolation is that for the straight sided, three-node triangular element which was used in this study. The value $\overline{A}(r,z)$ at any point within the triangle can be written as

$$\overline{A}_p(r,z) = \overline{\beta}_1 + \overline{\beta}_2 r + \overline{\beta}_3 z \tag{2.4}$$

Following the method of [34] the triangular shape functions N_1, N_2, and N_3 shown in Figure 2.4 are given by

$$N_i = \frac{a_i + b_i r + c_i z}{2\Delta_e} \tag{2.5}$$

where

$$a_i = r_j z_k = r_k z_j$$

$$b_i = z_j - z_k$$

$$c_i = r_k = r_j$$

$$2\Delta_e = \begin{vmatrix} 1 & r_i & z_i \\ 1 & r_j & z_j \\ 1 & r_k & z_k \end{vmatrix}$$

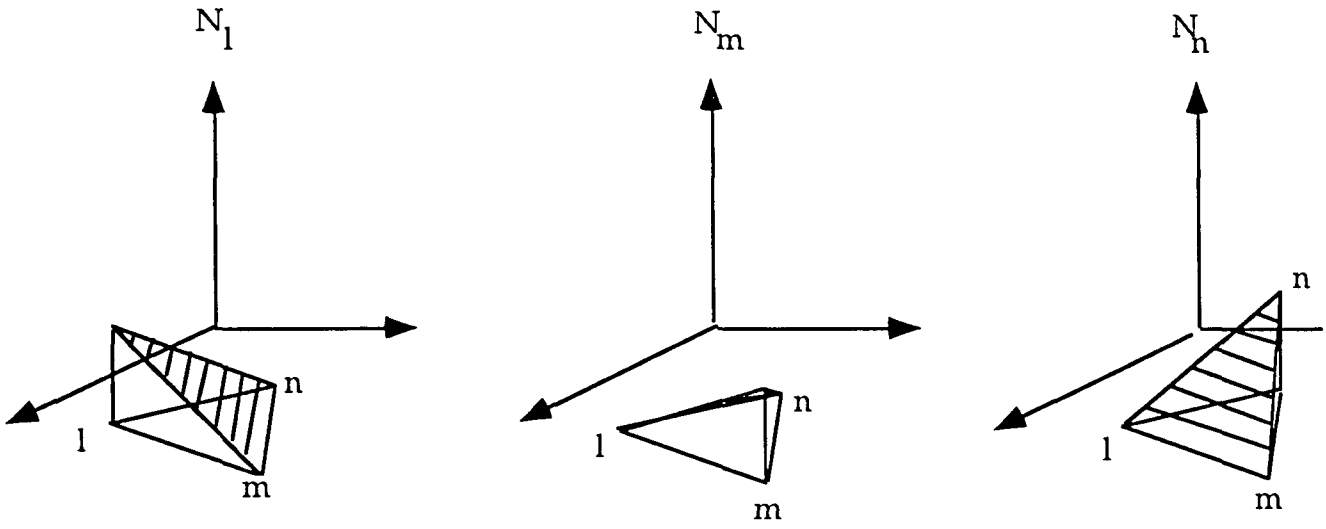

Figure 2.4. Shape functions for the three node triangular element.

3. Formulation

The finite element formulation is achieved by minimizing the energy functional of equation 2.3 as shown in references [42-43]. This is done by taking the first variation of the functional with respect to $\overline{A}$ as

$$\frac{\partial F}{\partial \overline{A}} = \int\int \left[\frac{1}{\mu}\left(\frac{\partial \overline{A}}{\partial r} + \frac{\overline{A}}{r}\right)\left(\frac{\partial}{\partial \overline{A}_i}\frac{\partial \overline{A}}{\partial r} + \frac{\partial \overline{A}}{\partial r}\right)\right.$$

$$\left. + \left(\frac{\partial \overline{A}}{\partial z}\frac{\partial}{\partial \overline{A}_i}\frac{\partial \overline{A}}{\partial z}\right) + j\omega\sigma\overline{A}\frac{\partial}{\partial \overline{A}_i}\overline{A} - \frac{\partial}{\partial \overline{A}_i}\overline{A}\,\overline{J}\right] r\,dr\,dz \qquad (2.6)$$

and setting it equal to zero. By incorporating the following equations

$$[N] = [\, N_1 \quad N_2 \quad N_3 \,],\ [\overline{A}] = \begin{bmatrix} \overline{A}_1 \\ \overline{A}_2 \\ \overline{A}_3 \end{bmatrix},\ [P] = \begin{bmatrix} \frac{1}{\mu} & 0 \\ 0 & \frac{1}{\mu} \end{bmatrix} \tag{2.7}$$

$$\Delta N = \begin{bmatrix} \frac{\partial N}{\partial r} + \frac{N}{r} \\ \frac{\partial N}{\partial z} \end{bmatrix} = \begin{bmatrix} \frac{\partial N_1}{\partial r} + \frac{N_1}{r} & \frac{\partial N_2}{\partial r} + \frac{N_2}{r} & \frac{\partial N_3}{\partial r} + \frac{N_3}{r} \\ \frac{\partial N_1}{\partial z} & \frac{\partial N_2}{\partial z} & \frac{\partial N_3}{\partial z} \end{bmatrix} \tag{2.8}$$

the variation becomes, in matrix form:

$$\frac{\partial F_e}{\partial A} = \int\int \frac{\partial}{\partial \overline{A}_e}[\overline{A}]_e^T[\Delta N]^T[P][\Delta N][\overline{A}]_e + j\omega\sigma\frac{\partial}{\partial \overline{A}_e}[\overline{A}]_e^T[N]^T[N]\,[\overline{A}]_e$$

$$- \overline{J}_s \frac{\partial}{\partial \overline{A}_e}[\overline{A}]_e^T[N]^T ds = 0 \tag{2.9}$$

From this formulation a final matrix equation is formed as

$$[\,[S]_e + j\,[R]_e]\,\{\overline{A}\}_e = \{\overline{Q}\}_e \tag{2.10}$$

where $[S]_e$ is a 3 x 3 'element matrix' formed from the r and z values of the three vertices l,m and n in element lmn and the element's area Δ.

$$[S]_e = \frac{r_c}{4\Delta\mu}\begin{bmatrix} (b_l' b_l' + c_l c_l) & (b_l' b_m' + c_l c_m) & (b_l' b_n' + c_l c_n) \\ (b_m' b_l' + c_m c_l) & (b_m' b_m' + c_m c_m) & (b_m' b_n' + c_m c_n) \\ (b_n' b_l' + c_n c_l) & (b_n' b_m' + c_n c_m) & (b_n' b_n' + c_n c_n) \end{bmatrix} \qquad (2.11)$$

where $b'_k = \left[b_k + \frac{\Delta}{3r_c} \right]$, k=l,m,n, r_c is the centroid of the element, and Δ is the area of the element. $[R]_e$ is a 3x3 'element matrix' formed from the angular frequency ω, electrical conductivity σ, associated with the element lmn and the area Δ, of the element lmn given by

$$[R]_e = \frac{\omega\sigma\Delta r_c}{12}\begin{bmatrix} 2 & 1 & 1 \\ 1 & 2 & 1 \\ 1 & 1 & 2 \end{bmatrix}. \qquad (2.12)$$

$\{\overline{Q}\}_e$ is a 3x1 'element matrix' formed from the complex source current density, within an element lmn given by

$$\{\overline{Q}\}_e = \frac{\bar{J}_s \Delta r_c}{3}\begin{Bmatrix} 1 \\ 1 \\ 1 \end{Bmatrix} \qquad (2.13)$$

$\{\overline{A}\}_e$ is a 3x1 'element matrix' formed from the unknown complex vector potentials $\overline{A}_l$, $\overline{A}_m$ and $\overline{A}_n$ at the apices of an element lmn.

$$\{\overline{A}\}_e = \begin{Bmatrix} \overline{A}_l \\ \overline{A}_m \\ \overline{A}_n \end{Bmatrix} \tag{2.14}$$

4. Assembly

These element matrices are all local matrices and are used in assembling the global matrix. Following the method of assembly described in [31-33] the final global matrix is formed.

$$[\overline{G}]\{\overline{A}\} = \{\overline{Q}\} \tag{2.15}$$

5. Constraints

Next boundary conditions are incorporated. For this geometry the Dirichlet boundary conditions are used forcing the magnetic vector potential to be zero at the boundaries as shown in Figure 2.5. The assumption is that the vector potential is zero at infinity and zero on the axis of symmetry.

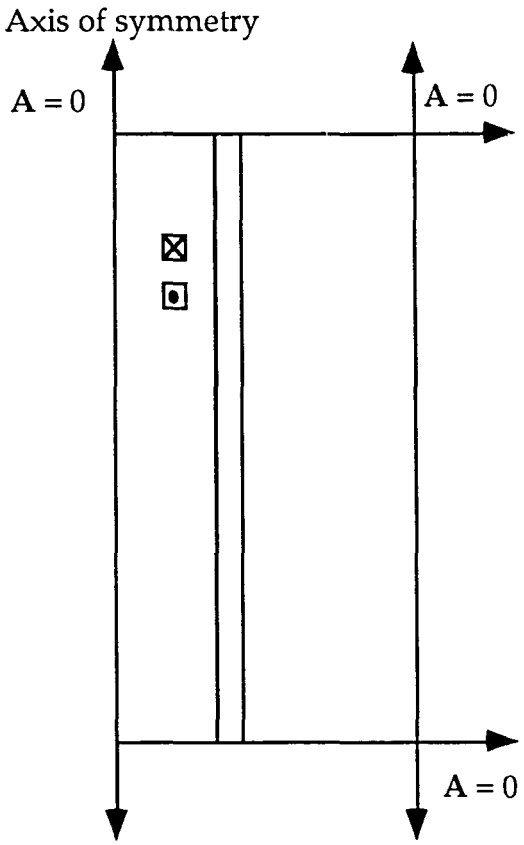

Figure 2.5. Boundary Conditions on vector potential.

6. Solution

The global matrix is solved using guassian elimination.

D. Mesh Refinement

As mentioned earlier a critical aspect of the finite element method is the mesh discretization of the region. The mesh must be adapted so a finer discretization is given to regions in which abrupt field changes are expected.

The mesh used in this research consisted of triangular elements which varied uniformly where necessary as shown in Figure 2.6. In Figure 2.6 the most discrete portion of the mesh in the z direction is 0.012". Although this is sufficient discretization for many defects of interest, to model fatigue cracks the mesh must have a finer discretization. There are a number of methods which can be used to increase discretization. A viable method would be to increase the discretization in the crack region only. The advantage to this is that the mesh need only be heavily discretized in the crack region. The disadvantage is that the finite element program must be adapted to accommodate this new mesh. This method was not used in this research but could be an aspect to investigate further.

In this research, a technique of decreasing the z distance of each element by one half in the region of probe travel was used. Thus, the number of elements roughly doubled with each mesh renovation. There are two main disadvantages to this method. The first is that the number of elements in the mesh is drastically increased because the entire region that the probe traverses must be heavily discretized, not just the crack region. For example, the original mesh with element width of 12 mils consisted of 8400 elements while the finest mesh had an element width of 1.5 mils, an element height of 12 mils, and consisted of 132,000 elements. This increase in elements increases CPU time drastically. This increase in CPU time is not a huge concern for a two-dimensional code, however, it would be a great concern in three-dimensional modeling. The second disadvantage to this method is that a large aspect ratio is produced from this method. The finest mesh in this study had an aspect ratio of

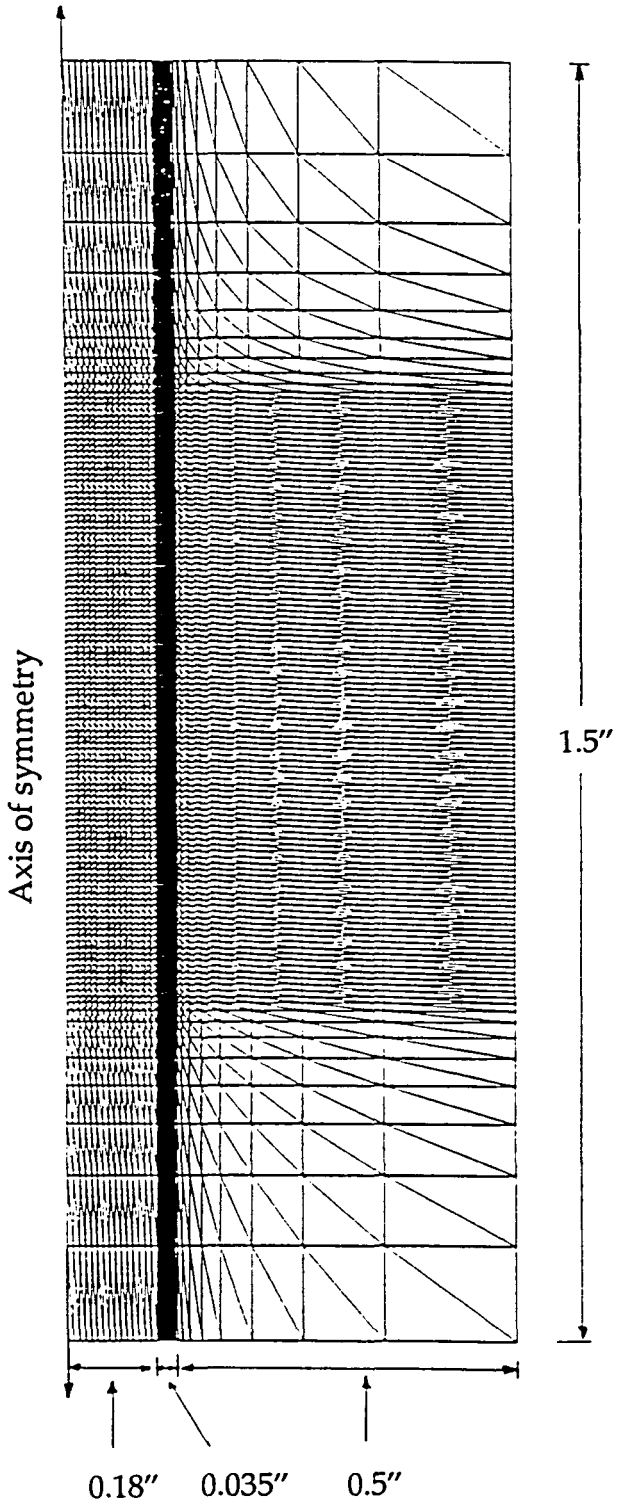

Figure 2.6 Finite element mesh.

8:1. This problem can only be avoided if the mesh is also discretized more in the radial direction. This would obviously cause a drastic increase in the number of elements.

Although this method has obvious disadvantages it was used for a number of reasons. First, since the mesh is uniform throughout, the original finite element code was easily adapted to accompany the modified mesh. Second, although the number of elements made the CPU time much greater, the run time never exceeded three hours on a Stellar workstation. Finally, although an aspect ratio of 8:1 seems large, a brief study included in this research shows that for normalized impedance values with aspect ratios as much as 8:1 the difference is less than 2% from the normalized impedance values of aspect ratio 1:1.

E. Modeling an Infinitesimally Narrow Crack

1. Introduction

The purpose of this thesis is to compare models of tight fatigue cracks in thin walled tubing. The mesh refinement discussed earlier was used to model decreasingly narrower fatigue cracks. Two questions then arise. First, is it possible to model an infinitesimally narrow crack? Second, if this is possible, how does the EC response from a crack in the finest mesh compare to the EC response from an infinitesimally narrow crack?

There are different methods of incorporating infinitesimally narrow cracks into a mesh. One method is to add two node elements to the mesh in the

crack region [44]. The method used in this research consisted of incorporating weighting functions into the element conductivity where necessary.

2. Formulation

Earlier in this chapter the finite element formulation for three node linear triangular elements was shown to involve an integration of the shape functions N_1, N_2 and N_3. From Figure 2.4 it can be seen that the three node triangular shape functions have a unity value at one node and a zero value at the other nodes with linear variance between the nodes. Thus, if these shape functions can be incorporated into the $[R_e]$ integral the desired value at a specified node can be forced to zero.

In the stiffness matrix calculations it was assumed that the conductivity was constant over each element in the $[R]_e$ matrix calculations of equation 2.10. Now, for elements in the crack region this assumption is no longer valid. That is, the conductivity value of nodes along the crack element are forced to a zero value. However, it is important to note that the conductivity of the element is not zero, only the conductivity at the specified crack node. This can be done by incorporating the proper shape function into the $[R]_e$ matrix formulation integral shown below and taken from the energy functional as

$$[R_e] = \int_A \sigma\omega [N]^T [N] \, dA \tag{2.16}$$

Equation 2.16 is modified by treating the value for conductivity not as a constant over the element as was done previously, but rather as a function dependant on the value of a particular shape function at the node as

$$\sigma = \overline{N}\,\overline{\sigma} = \left[\overline{N_l}\,\overline{N_m}\,\overline{N_n}\right]\begin{pmatrix}\sigma_l\\ \sigma_m\\ \sigma_n\end{pmatrix} \tag{2.17}$$

The shape function N used in equation 2.17 depends on which node is to be forced to zero. Next, the above shape functions from equation 2.5 are incorporated into equation 2.16 as

$$[R_e] = \omega \int_A \overline{N}^T(\overline{N}\,\sigma)\overline{N}\ dA \tag{2.18}$$

From Figure 2.7 it can be seen that different crack elements have different nodes which must have conductivity equal to zero. For an element for which nodes one and two have zero conductivity as shown in Figure 2.8, N_3 would be used as the weighting function in the $[R_e]$ integral as

$$\left[R_e\right] = \omega\,\sigma \int_A \begin{pmatrix}N_1\\ N_2\\ N_3\end{pmatrix}\left[N_1 N_2 N_3\right]\left[N_3\right]\ dA \tag{2.19}$$

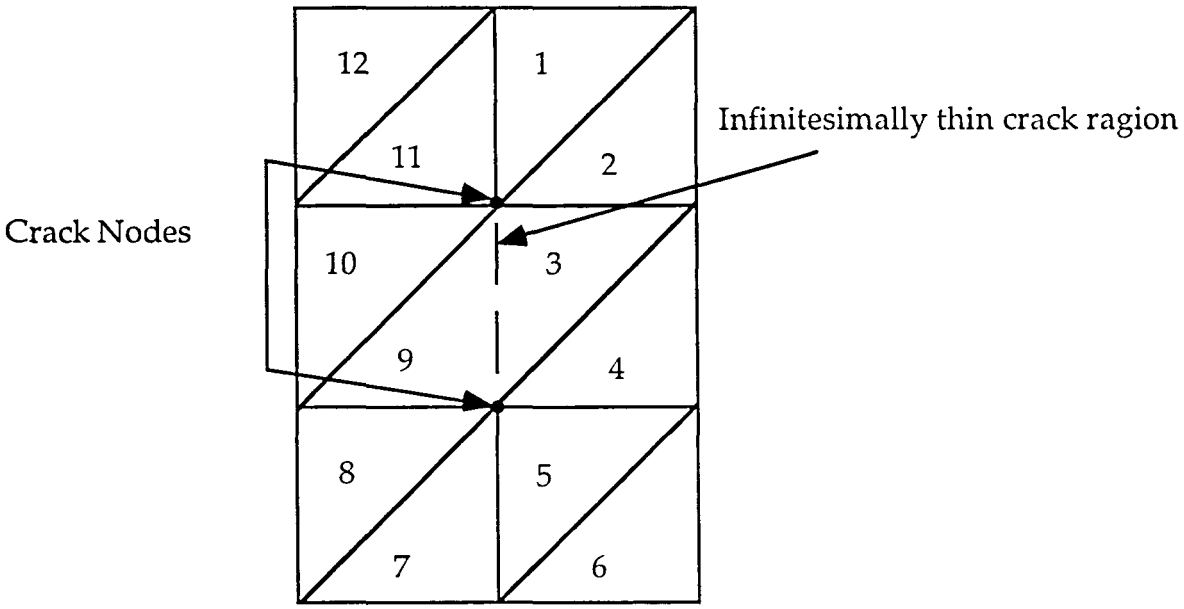

Figure 2.7. Elements adjacent to infinitesimally thin crack region.

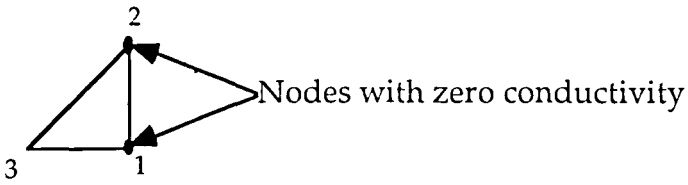

Figure 2.8. Element with nodes 1 and 2 having zero conductivity.

The resulting integral is given by

$$[R_e] = \omega \sigma \int_A \begin{bmatrix} (N_1N_1N_3)\,(N_1N_2N_3)\,(N_1N_3N_3) \\ (N_1N_2N_3)\,(N_2N_2N_3)\,(N_2N_3N_3) \\ (N_1N_3N_3)\,(N_2N_3N_3)\,(N_3N_3N_3) \end{bmatrix} dA \qquad (2.20)$$

The following equation can be used to integrate equation 2.20

$$\int_A N_1^{\alpha} N_2^{\beta} N_3^{\gamma} \, dA = \frac{\alpha!\ \beta!\ \gamma!}{(\alpha + \beta + \gamma + 2)!} 2A \qquad (2.21)$$

Evaluation of the integral results in the $[R]_e$ matrix given by

$$[R_e] = \frac{\omega \sigma \Delta r_c}{60} \begin{bmatrix} 2\,1\,2 \\ 1\,2\,2 \\ 2\,2\,6 \end{bmatrix} \qquad (2.22)$$

Thus equation 2.22 differs from the previous $[R_e]$ matrix in equation 2.12. The $[R_e]$ matrix varies depending on the weighting function chosen. For the element with conductivity equal to zero only at node one as in Figure 2.9 both N_2 and N_3 would be used in the integral as shown below

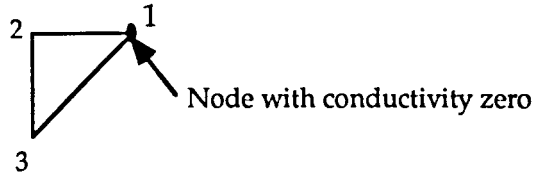

Figure 2.9. Element with zero conductivity at node one.

$$[R_e] = \omega\sigma\int_A \begin{bmatrix} N_1 \\ N_2 \\ N_3 \end{bmatrix} [\, N_1 \quad N_2 \quad N_3 \,] [N_2 + N_3]\, dA \tag{2.23}$$

Expanding the integral results in

$$[R_e] = \omega\sigma\int_A \begin{bmatrix} N_1^2N_2 & N_1N_2^2 & N_1N_2N_3 \\ N_1N_2^2 & N_2^3 & N_2^2N_3 \\ N_1N_2N_3 & N_2^2N_3 & N_2N_3^2 \end{bmatrix}$$

$$+ \begin{bmatrix} N_1^2N_3 & N_1N_2N_3 & N_1N_3^2 \\ N_1N_2N_3 & N_2^2N_3 & N_2N_3^2 \\ N_1N_3^2 & N_2N_3^2 & N_3^3 \end{bmatrix} dA \tag{2.24}$$

Evaluation of equation 2.24 using the above procedure results in the $[R]_e$ matrix given by

$$[R_e] = \frac{\omega\sigma\Delta r_c}{60}\begin{bmatrix} 433 \\ 384 \\ 348 \end{bmatrix} \tag{2.25}$$

Thus the local $[R]_e$ matrix has different values for elements along the cracks. Following the numbering scheme of Figure 2.7 the $[R]_e$ matrix of each element is as shown below.

ELEMENTS		$[R]_e$ MATRIX
1	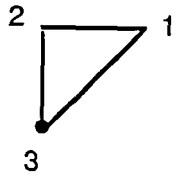	$\frac{\omega\sigma\Delta}{60}\begin{bmatrix} 8 & 4 & 3 \\ 4 & 8 & 3 \\ 3 & 3 & 4 \end{bmatrix}$
2	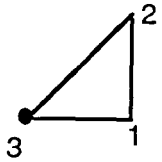	$\frac{\omega\sigma\Delta}{60}\begin{bmatrix} 8 & 4 & 3 \\ 4 & 8 & 3 \\ 3 & 3 & 4 \end{bmatrix}$
3	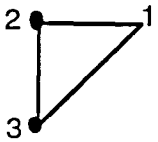	$\frac{\omega\sigma\Delta}{60}\begin{bmatrix} 6 & 2 & 2 \\ 2 & 2 & 1 \\ 2 & 1 & 2 \end{bmatrix}$
4	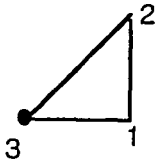	$\frac{\omega\sigma\Delta}{60}\begin{bmatrix} 8 & 4 & 3 \\ 4 & 8 & 3 \\ 3 & 3 & 4 \end{bmatrix}$
5	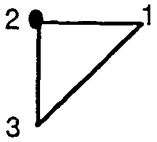	$\frac{\omega\sigma\Delta}{60}\begin{bmatrix} 8 & 3 & 4 \\ 3 & 4 & 3 \\ 4 & 3 & 8 \end{bmatrix}$

7 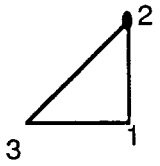

$$\frac{\omega\sigma\Delta}{60}\begin{bmatrix} 8 & 3 & 4 \\ 3 & 4 & 3 \\ 4 & 3 & 8 \end{bmatrix}$$

8 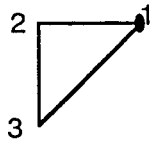

$$\frac{\omega\sigma\Delta}{60}\begin{bmatrix} 4 & 3 & 3 \\ 3 & 8 & 4 \\ 3 & 4 & 8 \end{bmatrix}$$

9 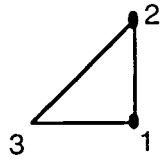

$$\frac{\omega\sigma\Delta}{60}\begin{bmatrix} 2 & 1 & 2 \\ 1 & 2 & 2 \\ 2 & 2 & 6 \end{bmatrix}$$

10 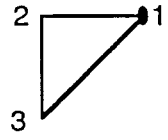

$$\frac{\omega\sigma\Delta}{60}\begin{bmatrix} 4 & 3 & 3 \\ 3 & 8 & 4 \\ 3 & 4 & 8 \end{bmatrix}$$

11 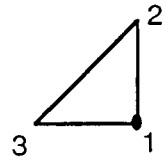

$$\frac{\omega\sigma\Delta}{60}\begin{bmatrix} 4 & 3 & 3 \\ 3 & 8 & 4 \\ 3 & 4 & 8 \end{bmatrix}$$

These local $[R]_e$ matrices are then substituted into equation 2.10 and assembled into the global matrix in the usual manner. The results of this method are discussed in Chapter 5.

F. Impedance Calculations

Once the magnetic vector potential values $\overline{A}$ are obtained the impedance of the coil can also be obtained. This can then be used to plot the IPTs which can be compared to experimental IPTs. Following [42], we start with the equation

$$Z = V/I \tag{2.26}$$

where Z is coil impedance, V is the phasor voltage across the coil, and I is the phasor current through the coil. Then using

$$V = \int_c \overline{E} \cdot d\bar{l} \tag{2.27}$$

and the relation

$$\overline{E} = j\omega\overline{A} \tag{2.28}$$

Equation 2.27 becomes

$$V = j\omega \int_c \overline{A} \cdot d\bar{l} \tag{2.29}$$

for a single loop coil of radius r the voltage becomes

$$V = j\omega 2\Pi r A \tag{2.30}$$

Thus, for a coil with N turns, equation 2.30 becomes

$$V = j\omega 2\Pi \sum_{i=1}^{N} r_i A_i \qquad (2.31)$$

To normalize the voltage to the number of elements in the coil cross section equation 2.31 becomes

$$V = j\omega 2\Pi \frac{N}{N_e} \sum_{i=1}^{N_e} r_{ci} A_{ci} \Delta_i \qquad (2.32)$$

where N_e is the number of elements in the coil cross section, A_{ci} is the centroidal vector potential value in the ith triangular element of the coil, r_{ci} is the centroidal radius and Δ_{ci} is the area of the ith element. By substituting equation 2.32 into equation 2.26 the impedance of the coil is given by

$$Z = j\omega \frac{2\,\Pi\, N\Delta}{I\, N_e} \sum_{i=1}^{N_e} r_d A_c \qquad (2.33)$$

CHAPTER 3. FATIGUE CRACK INITIATION AND GROWTH

A. Introduction

The purpose of this chapter is to give the reader a brief overview of the process of fatigue. This is an extremely broad subject and since this thesis is focussed on the eddy current probe response to fatigue cracks rather than on fatigue itself the discussion here is brief and limited to an overview of fatigue crack initiation and fatigue crack growth in metal. The reader is referred to many excellent references for a broad and detailed discussion of fatigue in metals [45-47].

The procession of fatigue damage can be classified into the following stages [46]:

1. Substructural and microstructural changes which cause nucleation of permanent damage.

2. The creation of microscopic cracks.

3. The growth and combination of microscopic flaws to form a dominant crack which could lead to catastrophic failure.

4. Stable propagation of a dominant macrocrack.

5. Structural instability or complete fracture.

The purpose of NDE in fatigue crack detection is to be able to detect fatigue cracks while they are still in stages one through four above. As mentioned in Chapter 1 the presence of a fatigue crack does not necessarily mean the structure will fail. However, it is obviously imperative that the fatigue crack be detected and attended to before structural instability occurs. The next sections discuss stages one through four above.

B. Fatigue Crack Nucleation

1. Introduction

Before beginning it is helpful to mention two points about fatigue initiation [45].

1. Fatigue failure occurs due to the initiation of a crack and the subsequent growth of that crack.

2. In homogeneous metals, cracks initiate at a free surface and no damage is done to metal away from its surface by the cyclic stressing.

Thus, fatigue crack phenomena are localized phenomena in the area of fatigue initiation and propagation. In cyclic stressing of ductile metals it is not necessary for the bulk of the grains in a piece of metal to fail by fatigue. Continued cyclic

plastic deformation in one localized surface region is sufficient. This trait of localized surface occurrence distinguishes fatigue failure from other modes of mechanical failure. It has been shown that the general features of fatigue failure do not vary with stress level [40] and are the same in all homogeneous ductile metals. Fatigue cracks can initiate in different manners once a stress is applied on a material. The next subsections discuss three possible ways fatigue cracks can initiate.

2. Slip Band Cracking

Although in general, fatigue failure is the same for different metals and stress levels, it has been shown that the size and location of surface cracking depends on the metal, stress level, and temperature [45]. In most ductile metals at room temperature and relatively high stress levels microcracks generally originate from persistently active slip bands [45]. These slip bands are spaced irregularly over the surface grains as shown in Figure 3.1. Slip bands are generally formed from slip lines. These slip lines, when formed under static loading appear as straight lines which are evenly distributed over each grain in the metal. When the slip lines are produced under cyclic stressing they form in bands and do not necessarily extend right across a grain. These bands grow wider and more dense with fatigue cracks initially forming in the broadened bands where slip is particularly intense. These are generally termed persistent slip bands (PSBs).

Figure 3.1. Development of persistent slip bands in copper. (a) Polished after 7% of the life. (b) Polished after 42% of the life. (c) polished after 77% of the life [45].

3. Grain Boundary Cracking

Although slip band cracking occurs in many ductile pure metals, it has been shown that other metals may exhibit grain-boundary cracking rather than slip band cracking [45]. Grain boundary cracking generally occurs for different reasons. It can occur from higher stress levels, it can also occur when the grain boundaries are weakened from alloying or temperature differences, or when the grains are misaligned. During grain boundary cracking, the grain boundaries are unable to accommodate large cyclic deformation in neighboring grains. This creates severe strain gradients at the grain boundaries, providing an additional shearing mechanism which gives rise to surface crevices [45]. Because different grains have different elastic and plastic properties, the severity of strain incompatibility across a grain boundary depends on the number of slip bands that can be activated in neighboring grains, thus relieving the stress at a common grain boundary. Thus, if slip bands can form, the stresses at the grain boundaries are relieved. Thus, whether or not grain-boundary cracking occurs depends on whether the induced cyclic strains can be accommodated by repeated slip in the grains, thus relieving the incompatibility across a grain boundary, or whether the incompatibility sets up such severe strain gradients that cracking occurs here before the slip mechanisms can operate in the grains. It follows therefore, that grain-boundary cracking will occur whenever the boundaries are weakened relative to the grains. An example of grain-boundary cracking is shown in Figure 3.2.

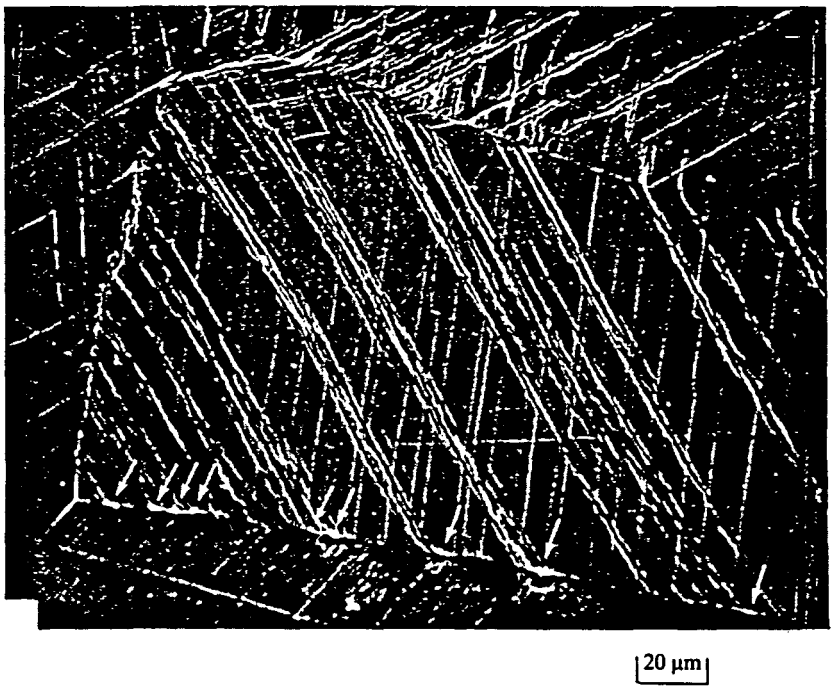

Figure 3.2. Nucleation of fatigue flaws (denoted by arrows) along a grain boundary [46].

4. Inclusion-Matrix Boundary Cracking

Stress and strain concentrations sometimes form around inclusions or intermetallics in highly alloyed metals. If the metal has a complex microstructure inhibiting slip, cracks can form at the inclusion-matrix boundary before the stress level necessary to cause cyclic slip in a surface grain is reached. This type of crack initiation is feasible at both near surface and interior locations in commercial alloys. An example of inclusion boundary cracking is shown in Figure 3.3.

Figure 3.3. Example of fatigue cracks associated with inclusions [50].

5. Summary

Surface cracking can occur in many different ways; as a continuation of surface roughening in broad slip bands, as a result of severe strain incompatibilities across grain boundaries, or because of the presence of inclusions or inhomogeneities in the surface. If the grain boundaries or inclusion interfaces can sustain the imposed strain incompatibilities across them without cracking, microcracks will develop from slip bands.

C Microscopic Crack Growth

On a microscopic scale, fatigue crack growth is often an irregular process. Examination of the fracture surface of 2024-T4 aluminum alloy [45] showed that the main fracture surface was irregular with numerous interconnected cracks

intersecting the main crack; some of these cracks were nearly perpendicular to the main fracture. In another study [45] it was shown that in the region of the crack front, numerous apparently independent cracks were found.

The initiation of surface microcracks in the metal followed by their subsequent extension across and penetration into the metal are the basic features of fatigue failure. Generally, the direction of surface microcracks is initially that of the slip bands. It remains in this direction until a microcrack is of sufficient size that the amount it opens and closes is sufficient to affect a large enough volume of material along its edge for it to grow in a continuum. This occurs under resolved cyclic stresses acting normal to the crack faces.

This phenomenon of early microcracking followed by later fatigue crack growth has been observed by Haworth, Sinh and Mueller [51]. Shown in Figure 3.4 is the extensive development of coarse slip bands over the specimen surface very early in the fatigue life of unnotched specimens. Prior to fatigue cycling there is no evidence of slip bands or microcracks. There are only constituent particles and voids in the surface where particles are lost by abrasion during grinding or polishing. During the first 25 fatigue cycles a substantial amount of deformation occurs, as shown in Figure 3.4(a). There is some evidence of microcracking and a severe local deformation due to the constituent particles. The microcracks are predominantly perpendicular to the tensile axis and do exceed about 10 microns in length. During the first 1 percent of fatigue life a rapid intensification of slip band density is observed and the number of microcracks increases rapidly. These changes are shown in Figure 3.4(b) after 500 fatigue cycles and in Figure 3.4(c) after 20,000 cycles. The overall surface roughness increases significantly between 25 and 500 cycles, but the changes

between 500 and 20,000 cycles are less pronounced. With the exception of a small increase in the number microcracks, no further surface changes are observed until fatigue crack propagation beyond approximately 20 microns occurs. Very few of the microcracks develop beyond about 20 microns in length at any stage of the fatigue life. In Figure 3.4(d) a macrocrack can be seen with length of 60 microns and direction normal to the stress.

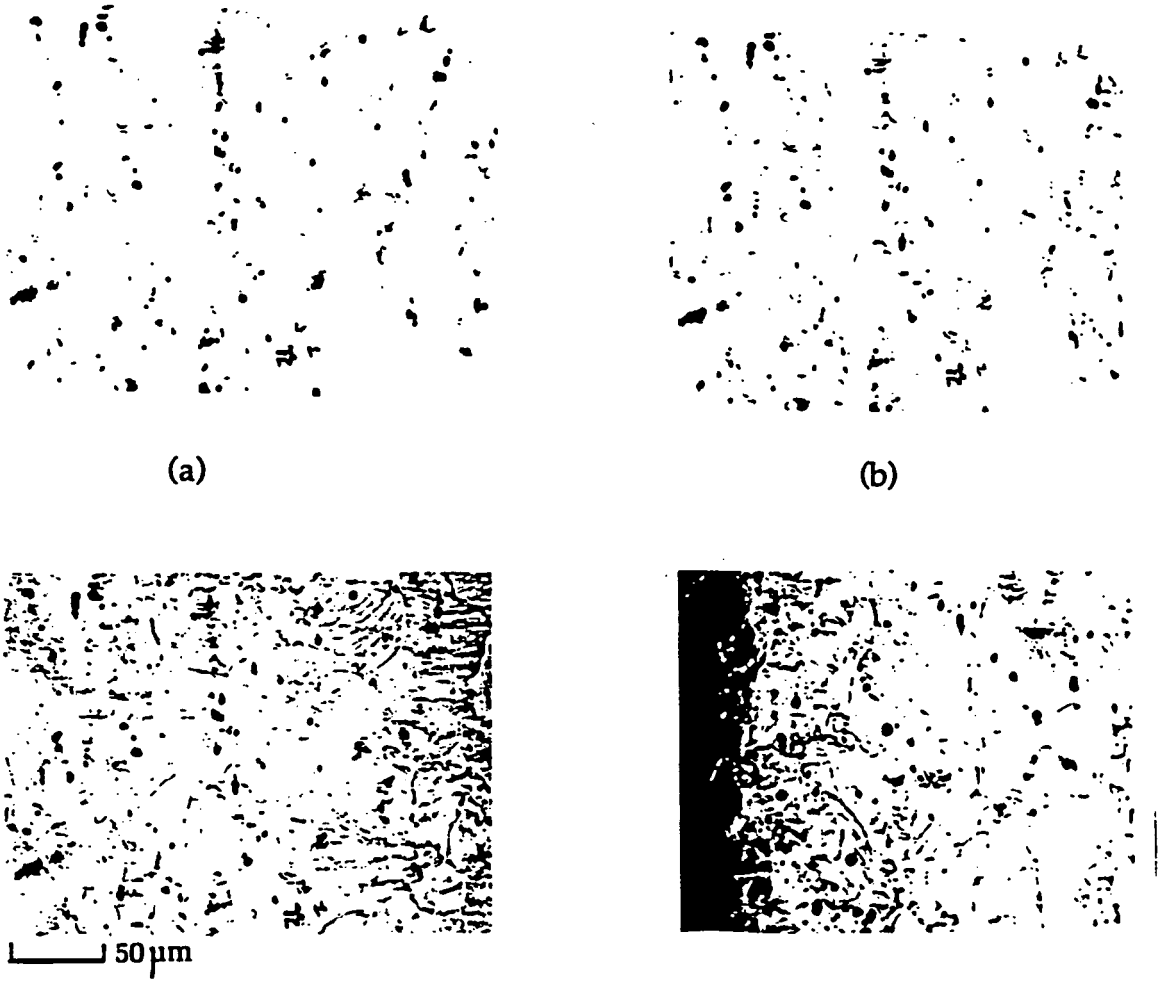

Figure 3.4. Progressive development of fatigue damage in unnotched 2024-T3 aluminum. Number of cycles elapsed: (a) 25, (b) 500, (c) 20,000, (d) 78,200 [51].

D. Fatigue Crack Growth

1. Introduction

There are three basic modes of crack surface displacement which can cause crack growth as shown in Figure 3.5.

I. The opening mode. The crack surfaces move directly apart.

II. The edge sliding mode. The crack surfaces move normal to the crack front and remain in the crack plane.

III. The shear mode. The crack surfaces move parallel to the crack front and remain in the crack plane.

For this discussion and most actual fatigue crack growth, mode I can generally be assumed to be the dominant mode of crack growth.

2. Stage I Crack Growth

The microscopic mode of fatigue crack growth is strongly affected by the slip band characteristics of the material, characteristic microstructural dimensions and applied stress level. In ductile solids, cyclic crack growth is a process of intense localized deformation in slip bands near the crack tip which

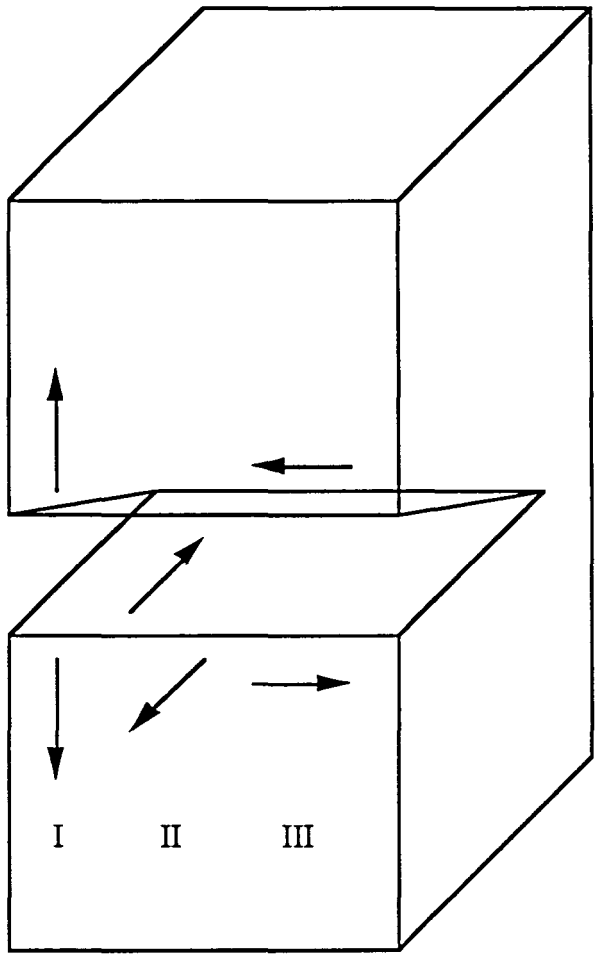

I Opening Mode
II Edge Sliding Mode
III Shear Mode

Figure 3.5. Modes of crack surface displacement.

leads to the creation of new crack surfaces. When the crack and the zone of plastic deformation surrounding the crack are confined to within a few grain diameters, crack growth occurs predominantly by single shear, in the direction of the primary slip system. This single slip mechanism leading to a zig-zag crack path has been termed stage I crack growth by Forsyth [46]. A schematic of this phenomenon is shown in Figure 3.6 with an example shown in Figure 3.7. Once a crack is nucleated along slip bands, the crack generally continues to develop

along an active slip plane, generally a PSB. The PSB's are formed on the most highly stressed slip plane, where the orientation of the crack is usually at 45 degrees to the stress axis [48]. In this configuration it is known as a stage I crack.

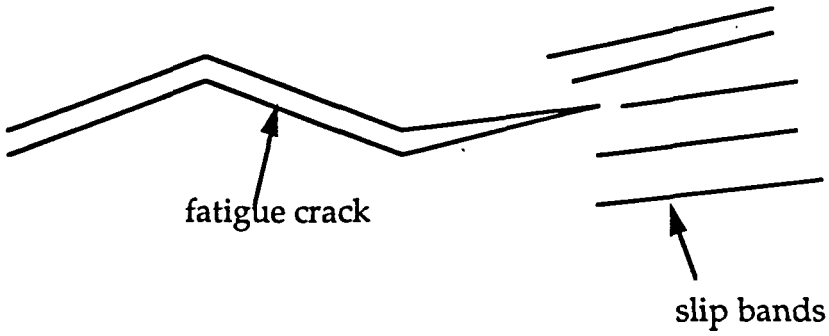

Figure 3.6. Schematic of stage I fatigue crack growth in slip bands.

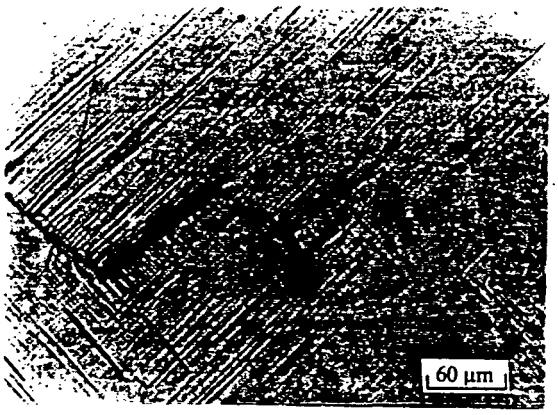

Figure 3.7. Example of stage I fatigue crack growth in slip bands [46].

3. Stage II Crack Growth

At higher stress intensity range values, the plastic zone at the crack tip encompasses many grains. The crack growth process involves simultaneous or alternating flow along two slip systems. This duplex slip mechanism, termed stage II by Forsyth [46], results in a mode I crack path normal to the far-field tensile axis. A schematic of stage II fatigue crack growth is shown in Figure 3.8 with an example shown in Figure 3.9. The growth process is now associated with the magnitude of the tensile strain range in the volume of material just ahead of the crack edge. The direction of crack growth is now that which allows the maximum crack opening and closing during the fatigue cycle. This is perpendicular to the cyclic tensile stress (rather than 45 degrees with the PSBs in stage I) and is independent of any crystalline slip plane, although in the early stages the crack may follow a crystallographic plane closely. The crack is now termed a macrocrack which spreads rapidly through the metal.

While the fracture surfaces created by stage I fatigue exhibit a tortuous profile, stage II crack growth generally leads to the formation of fatigue 'striation'. These striations are ripples on the fracture surface and an example is shown in Figure 3.10. Although striations are not found on all fatigue fracture surfaces, the presence of striations on a fracture surface is proof that failure was caused by fatigue [45].

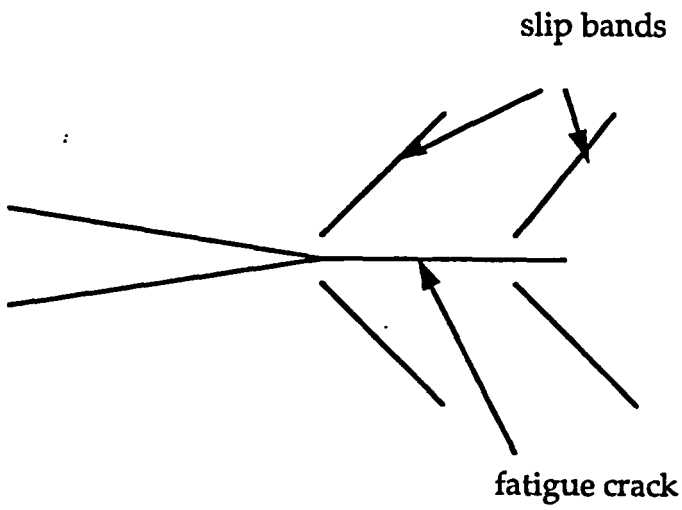

Figure 3.8. Schematic of stage II Fatigue Crack Growth.

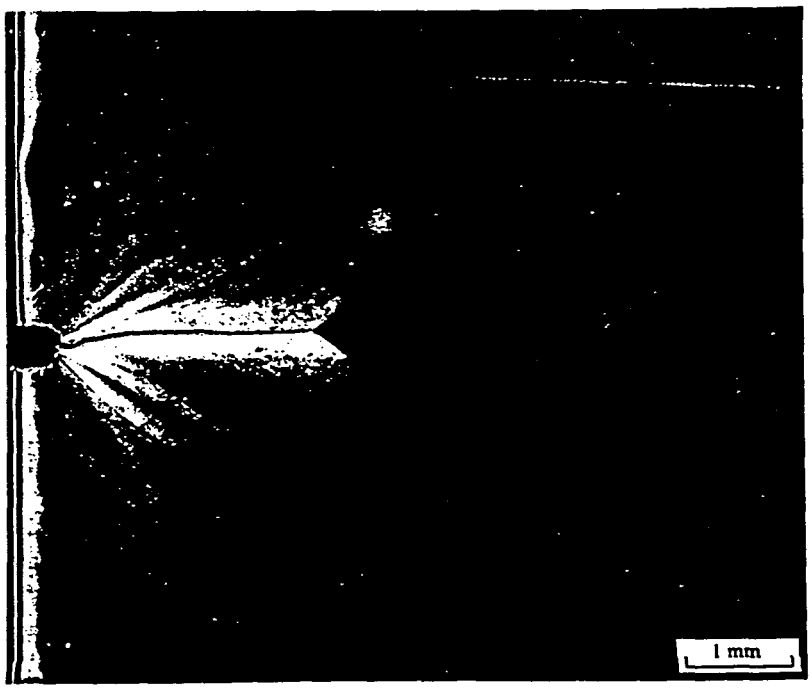

Figure 3.9. Example of stage II fatigue crack in metal [46].

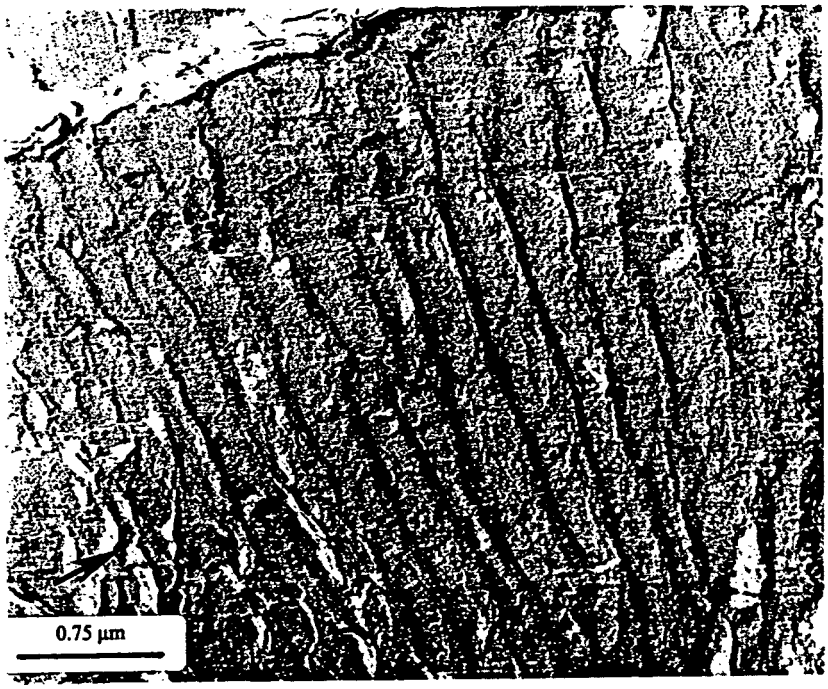

Figure 3.10. Example of striations in fatigued metal [46].

4. Grain Size In Crack Growth

As mentioned earlier in this chapter grain boundary cracking generally occurs when the stresses are high or when the grains are weakened. Generally grains are weaker when they are large or misaligned. For large-grained or weak-grained material, cracks are nucleated at grain boundaries parallel and perpendicular to the stress axis, however, for fine-grained material, cracks only occur perpendicular to the stress axis [50]. An example of this is shown in Figure 3.11. Consider the case of under-aged and over-aged microstructures of an aluminum alloy [46]. The over-aged condition leads to a reduction in stress intensity factor [46], while the under-aged condition leads to an increase in stress

intensity factor. This increase in stress intensity factor is also found with increase in grain size. In the under-aged condition, a tortuous crack path is observed as shown in Figure 3.12(a). In the over-aged condition the crack growth is perfectly straight as shown in Figure 3.12(b).

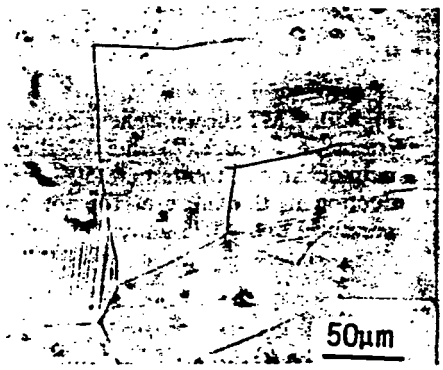

(a)

(b)

Figure 3.11. Effect of grain size on fatigue-crack formation. (a) Grain size 220 μm, (b) Grain size 30 μm [50].

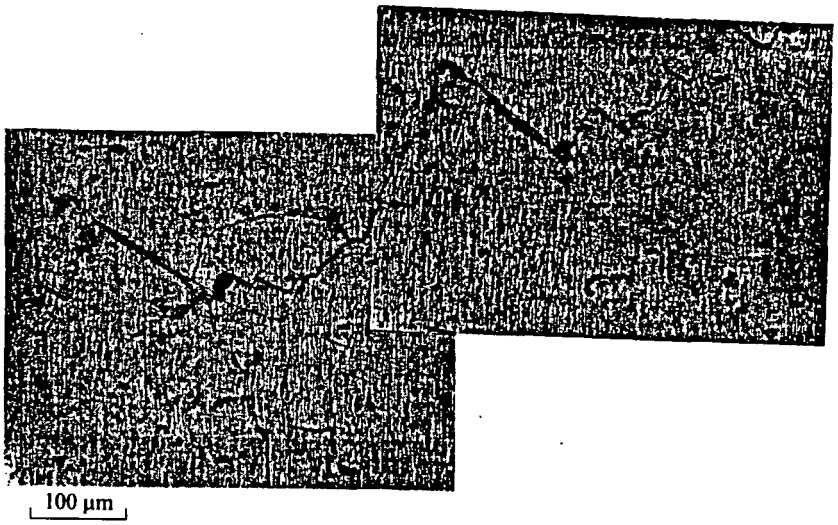

(a)

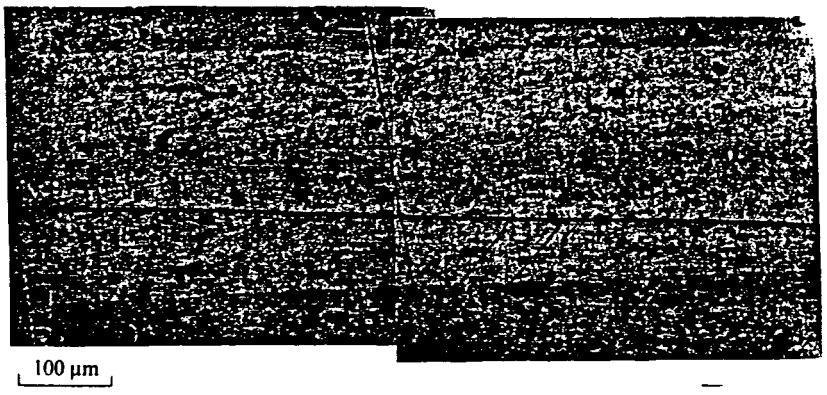

(b)

Figure 3.12. Example of fatigue crack in (a) under-aged metal, (b) over-aged metal [46].

It should be pointed out at this point that most tubing products are made by taking a metal cylinder, heating it, and pushing it over a point. This in turn stretches the metal and causes the grains in the tube to become elongated along the axis which in turn weakens the grains.

E. Summary

The above discussion clearly illustrates that fatigue crack growth does not involve only the growth of a single straight crack in a material. Rather, the type of crack path can be quite tortuous depending on factors such as strain level, grain size and age of the material. Also, the fatigue crack may have microcracking associated with it. These are both aspects which could have a significant effect on the eddy current response of the material. Thus, it is important that they be taken into account when determining reference standards.

Very few aspects of fatigue are mentioned here. The subject is much too broad to cover in detail here and hence for more information the reader is strongly encouraged to refer to the noted references. There are many fascinating aspects of fatigue and fatigue crack growth. The main purpose here is to show the reader that fatigue cracks can initiate and grow in different manners.

CHAPTER 4. EXPERIMENTAL PROCEDURE

A. Introduction

One purpose of this study was to investigate how well a two-dimensional numerical model can simulate actual EC fatigue crack responses. Thus, an essential portion of this study was the preparation of actual tubing samples with fatigue cracks. Also, tubing samples with EDM notches were prepared to compare EC EDM responses to EC fatigue crack responses. This chapter describes the preparation of fatigue cracks in stainless steel tubing, the generation of EDM notches in stainless steel tubing, and the subsequent collection of EC data from these samples.

B. Fatigue Crack Preparation

When developing a process to create fatigue cracks in the stainless steel tubing a major concern was preparing the fatigue cracks without completely damaging the tubing. To create the fatigue cracks a Krause fatigue machine shown in Figure 4.1 was used. A diagram of the fatigue machine is shown in Figure 4.2. The machine operates by rotating the specimen while both ends are held in collets. On one end of the specimen constant weight is applied from 0 to 200 lbs. The specimen is rotated with a variable speed motor. As the fatigue machine rotates the specimen, the sample is placed in continually alternating tension and compression, which produces stress and heat in the specimen.

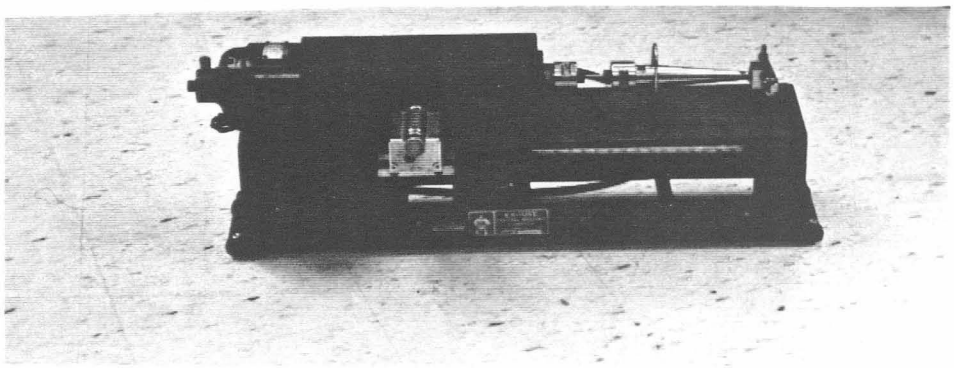

Figure 4.1. Krause fatigue machine.

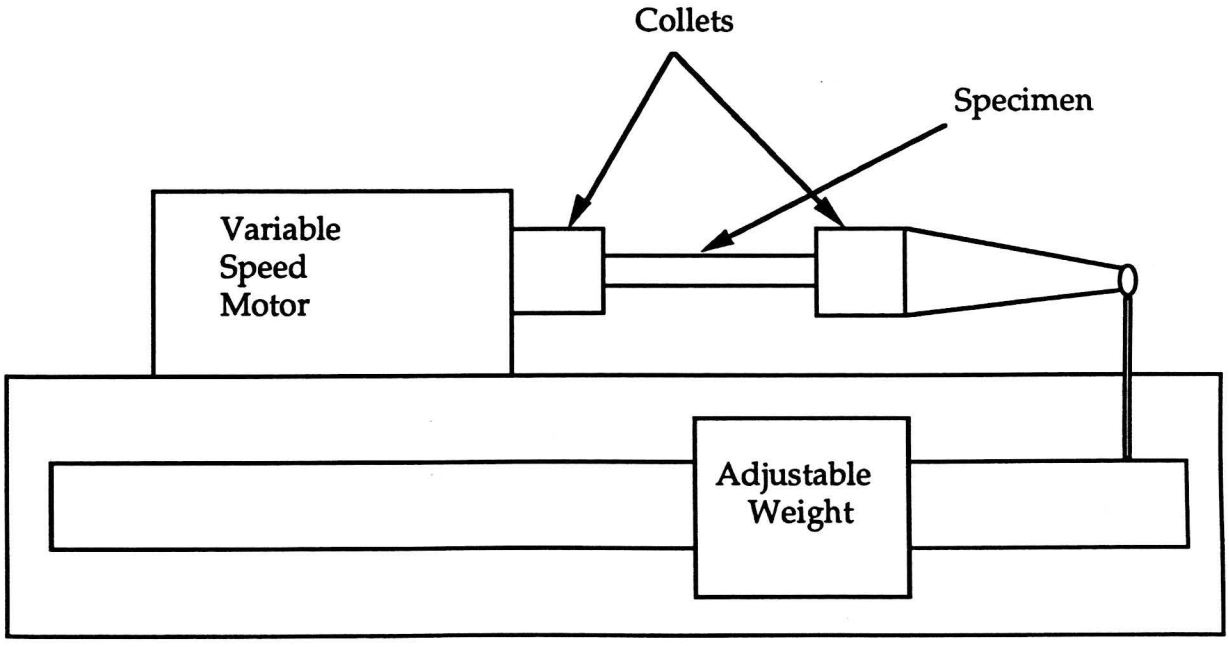

Figure 4.2. Schematic of fatigue machine.

This continual process then weakens the sample and usually causes a fatigue crack to form in the tube.

When the fatigue machine was actually put into use, it was difficult to determine how best to create the defects. Since the machine produced stresses perpendicular to the axis, it was assumed that the fatigue machine would create circumferential fatigue cracks, ideal for simulation by the axisymmetric finite element code. A problem was predicting where the tube would crack. The maximum stresses are produced farthest from the load, however, since the tube contains elongated grains and inclusions there are areas more likely to strain. Also, when the tube is heated and cooled the tube expands and contracts and this further weakens these areas.

To produce the fatigue cracks in the tubing the machine was initially run at very high rpm (3000 rpm) with relatively low weight (30 lbs) on the end of the tube. The machine would be run constantly until a fatigue crack was produced. The problem with this method was not in actually producing the fatigue cracks, but rather in stopping the fatigue crack before complete failure of the sample. With the high rpm, the fatigue fracture would occur much too rapidly to constrain it. Thus, a different approach had to be taken. This new approach involved using a much lower rpm (200 rpm) and a much higher weight (160-200 lbs) to compensate for the low rpm. The best results for fatigue crack production seemed to come from running the tube at approximately 200 rpm with 180 lbs on the end until the tube began producing a significant amount of heat. Then the tube would be allowed to cool and the process would be repeated. This combined process of rotation, loading, heating and cooling would produce a circumferential fatigue crack. The main disadvantage to this procedure was that

This continual process then weakens the sample and usually causes a fatigue crack to form in the tube.

When the fatigue machine was actually put into use, it was difficult to determine how best to create the defects. Since the machine produced stresses perpendicular to the axis, it was assumed that the fatigue machine would create circumferential fatigue cracks, ideal for simulation by the axisymmetric finite element code. A problem was predicting where the tube would crack. The maximum stresses are produced farthest from the load, however, since the tube contains elongated grains and inclusions there are areas more likely to strain. Also, when the tube is heated and cooled the tube expands and contracts and this further weakens these areas.

To produce the fatigue cracks in the tubing the machine was initially run at very high rpm (3000 rpm) with relatively low weight (30 lbs) on the end of the tube. The machine would be run constantly until a fatigue crack was produced. The problem with this method was not in actually producing the fatigue cracks, but rather in stopping the fatigue crack before complete failure of the sample. With the high rpm, the fatigue fracture would occur much too rapidly to constrain it. Thus, a different approach had to be taken. This new approach involved using a much lower rpm (200 rpm) and a much higher weight (160-200 lbs) to compensate for the low rpm. The best results for fatigue crack production seemed to come from running the tube at approximately 200 rpm with 180 lbs on the end until the tube began producing a significant amount of heat. Then the tube would be allowed to cool and the process would be repeated. This combined process of rotation, loading, heating and cooling would produce a circumferential fatigue crack. The main disadvantage to this procedure was that

it took approximately 4-5 hours to produce a fatigue crack. If more than a couple of fatigue cracks were to be made it would be a matter of days before they could be produced. Also, the fatigue procedure often resulted in deformation in the portion of the tube held by the collets. This deformation produce a strong eddy current response which often interfered with the eddy current response from the fatigue crack itself. The main advantage, of course, was that the tubes had cracks that were produced from actual fatigue.

C. Fatigue Crack Analysis

A scanning electron microscope (SEM) was used to investigate the size, shape, and structure of the fatigue cracks. The resulting photographs are shown in Figure 4.3 (a-f). The photographs are for two different fatigue cracks with views of fatigue crack top, bottom and fracture surfaces.

Figure 4.3 (a) shows the top view of a fatigue crack which is growing circumferentially around the tube. From the photograph it can be seen that there is extensive microcracking on the surface perpendicular to the fatigue crack. This was also observed in Chapter 3 of this thesis. It can also be seen that instead of having a straight growth path, the fatigue path is very tortuous, zig-zagging back and forth. The width of the fatigue crack can be seen to be about 10 microns (0.4 mils). Figure 4.3 (b) shows a photograph of the same crack from the inner diameter of the tube. From this photograph it can be seen that this is a through-wall crack. Also, there is no visible microcracking on the inner surface. These fatigue cracks are assumed to start from the outer diameter and, as mentioned in Chapter 3, microcracking usually occurs only on the surface where the fatigue

crack initiates. This statement is supported by these photographs. Figure 4.3 (c) shows the fracture surface of this fatigue crack. From the photographs it can be seen that the leading edge of the crack is nearly perpendicular to the surface. However, the outer diameter does lead the inner diameter slightly. This indicates that the fatigue crack reached through-wall depth early and then grew around the circumference as illustrated in Figure 4.4. This phenomenon could be expected in thin-walled tubing. Figure 4.3(d) shows the fracture surface of microcracking on the outer diameter. It can be seen that the microcracking does not extend deep into the surface of the tube. Figure 4.3(e) clearly shows striations on the fracture surface. The striations verify that these cracks are actually formed from fatigue. Another interesting observation is that the striations are not so much downward, but rather are outward around the circumference of the tube. This is further support for the fatigue crack growth pattern of Figure 4.4. Figures 4.3 (f-j) show photographs of another fatigue crack with similar implications.

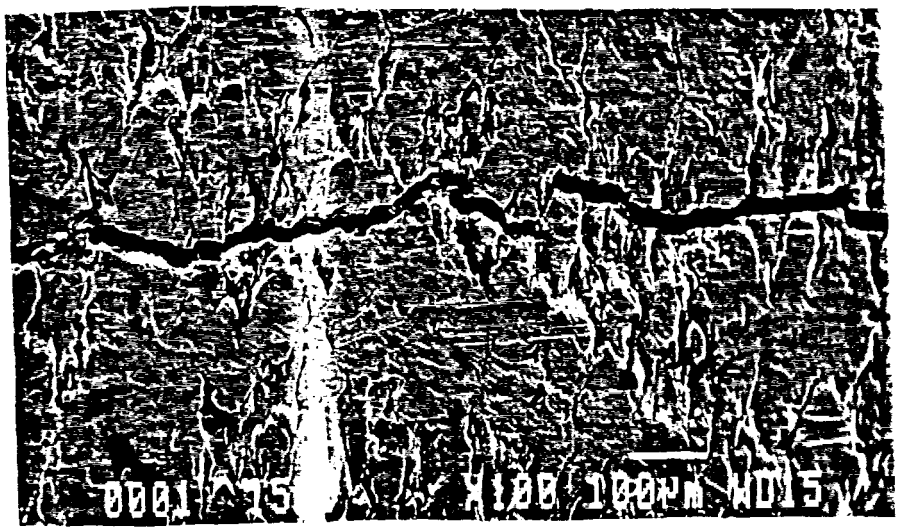

(a)

Figure 4.3 Scanning electron micrograph of fatigue crack; (a) Top view (100X).

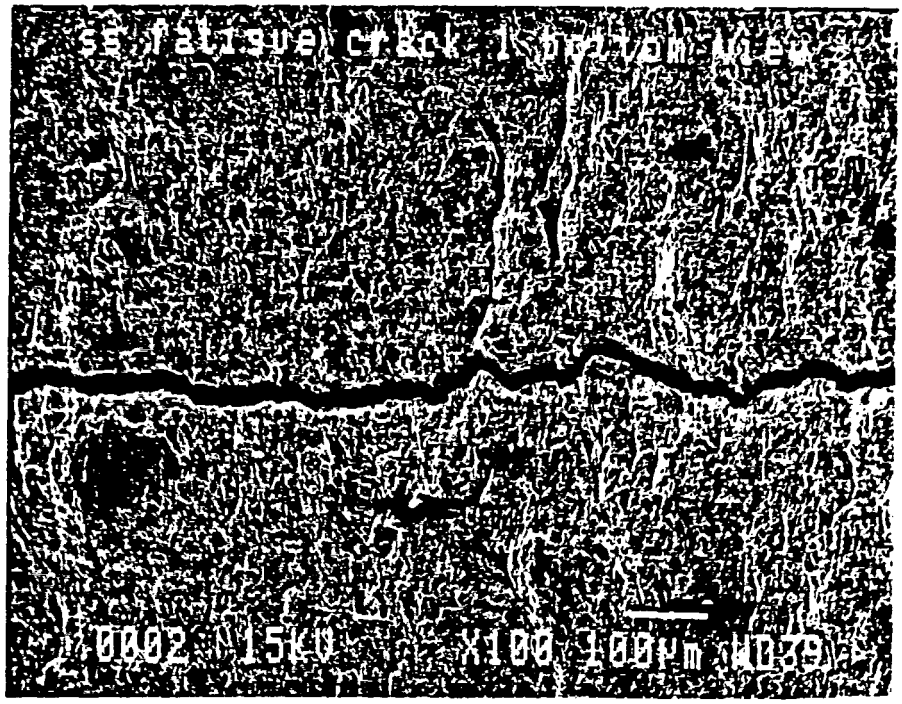

(b)

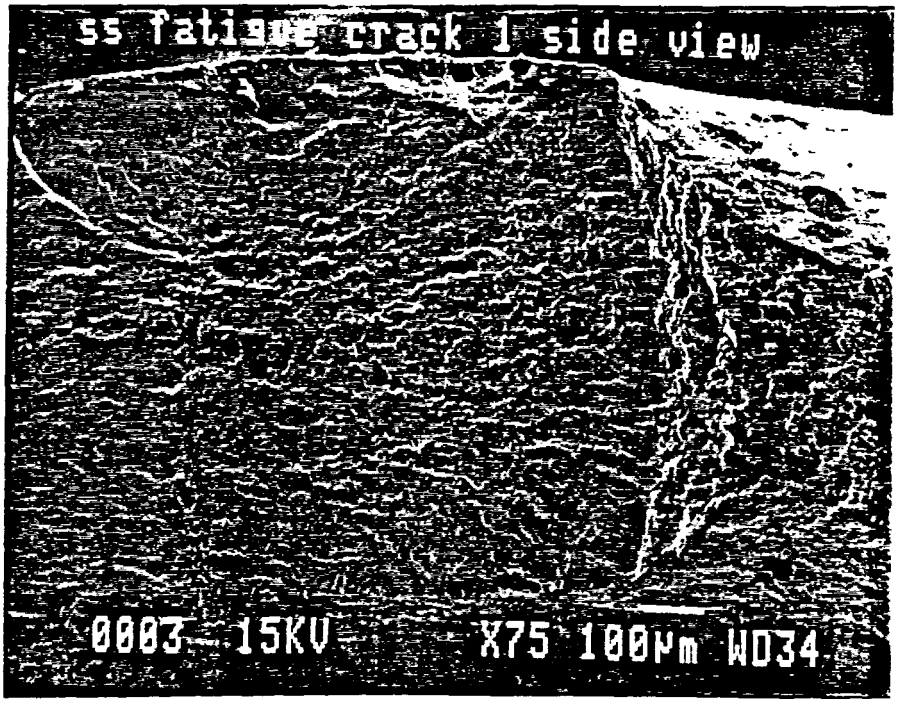

(c)

Figure 4.3. continued; (b) Bottom view (100X). (c) Side view of fracture surface (75X).

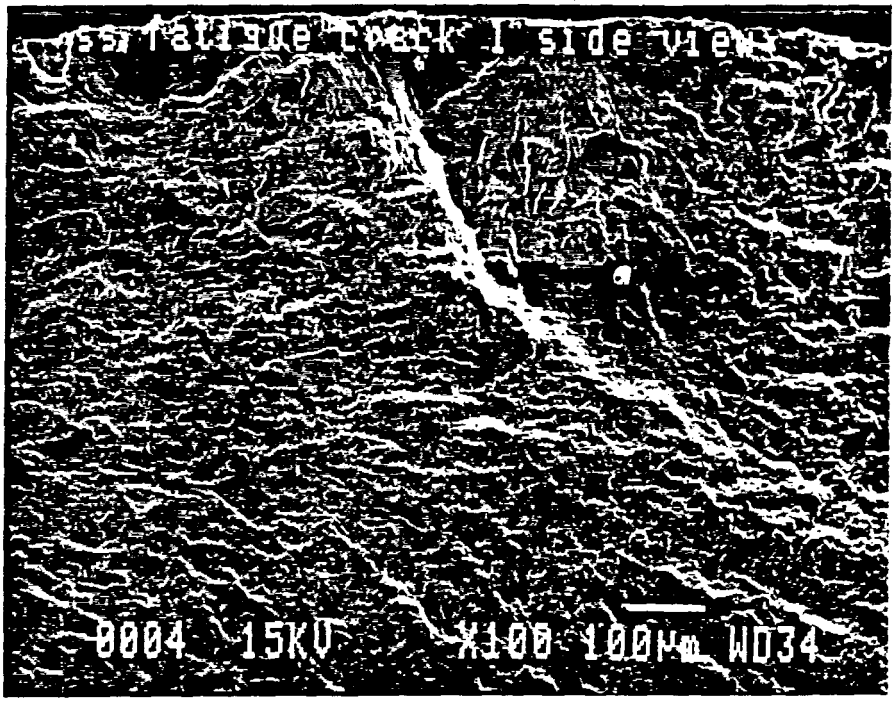

(d)

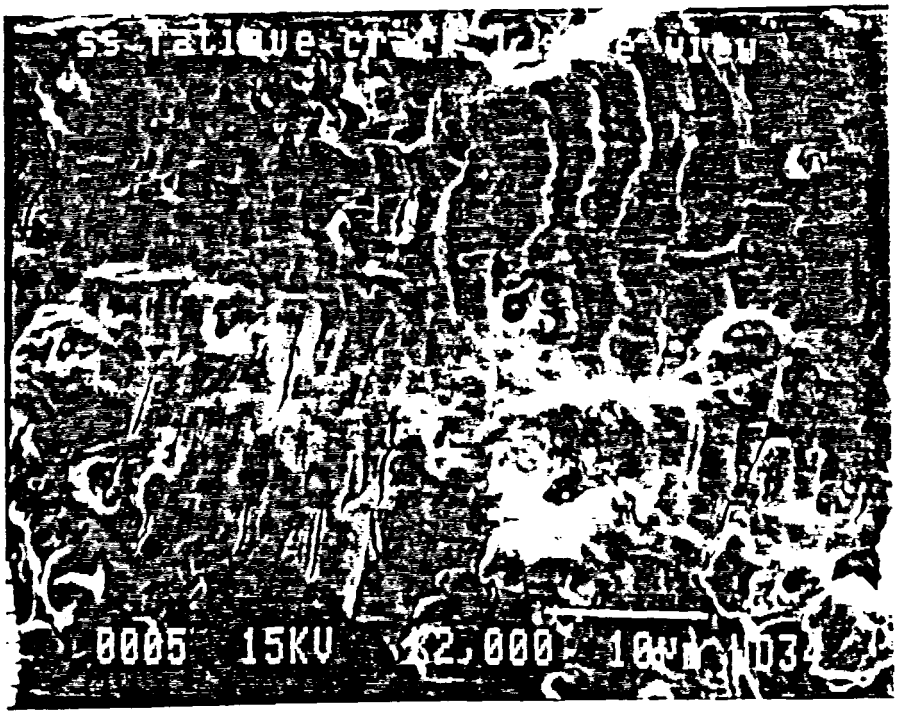

(e)

Figure 4.3. continued; (d) Side view of microcracking in fracture surface (100X). (e) Fatigue striations from fracture surface (2000X).

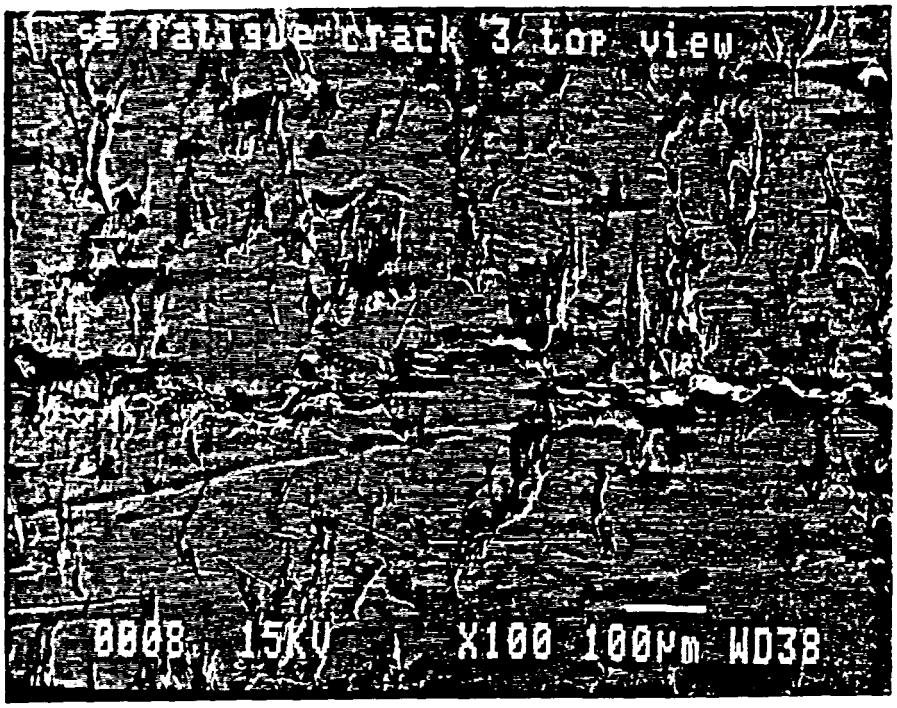

(f)

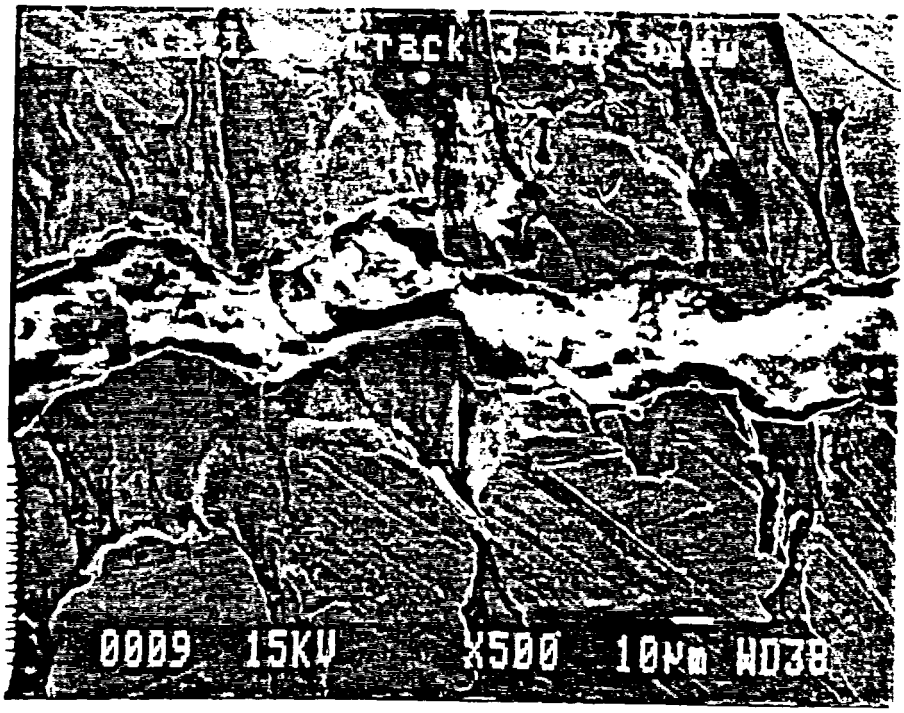

(g)

Figure 4.3. continued; (f) Top view (100X). (g) Top view (500X).

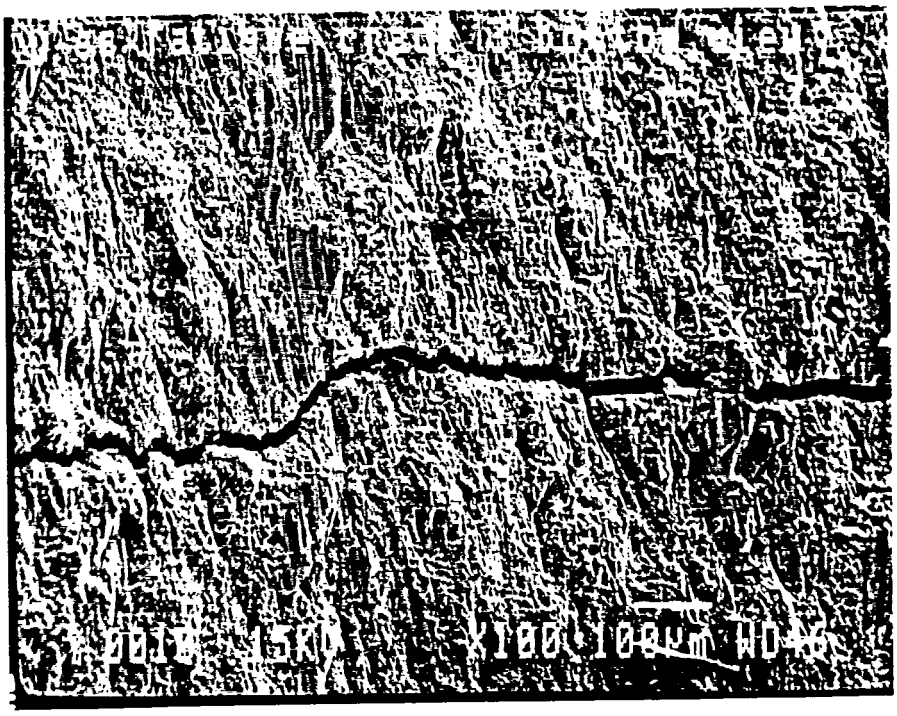

(h)

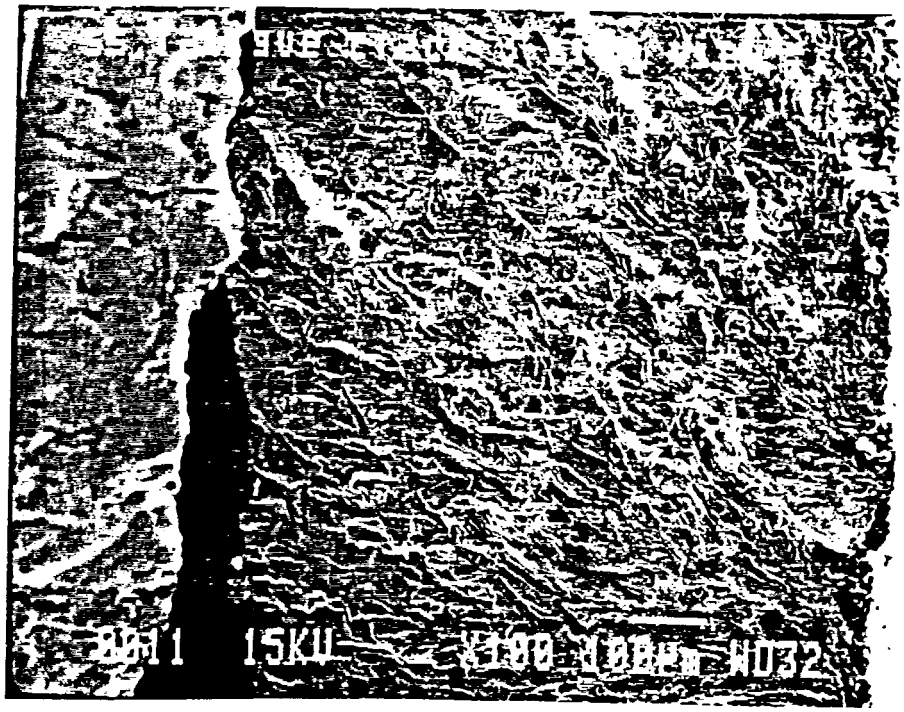

(i)

Figure 4.3. continued; (h) Bottom view (100X). (i) Fracture surface (100X).

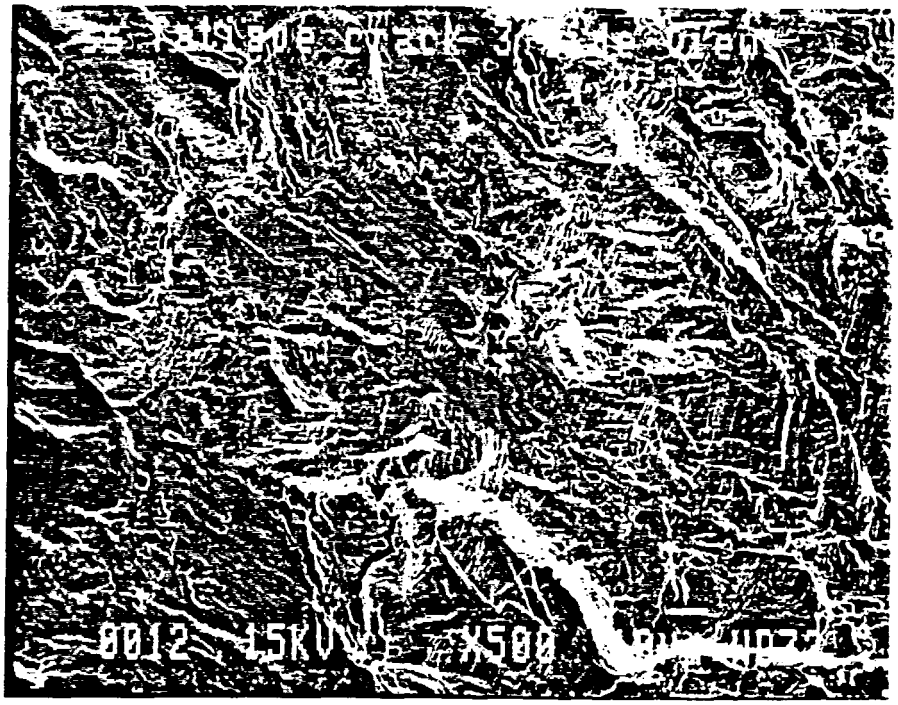

(j)

Figure 4.3 continued; (j) Fracture surface (500X).

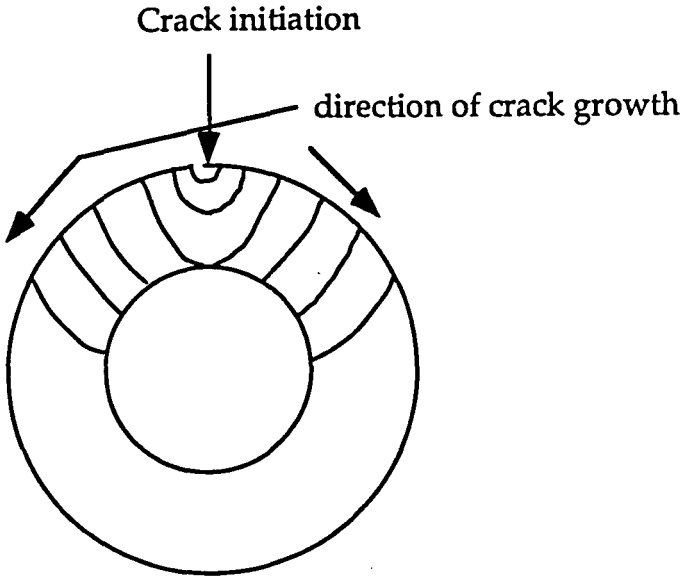

Figure 4.4. Fatigue crack growth in tubing.

Thus, from the SEM photographs certain conclusions can be made about the fatigue cracks grown in this experiment.

1. The cracks can be assumed to have formed from fatigue because they contain striations.

2. The fatigue cracks started from the outside of the tube and grew quickly to the inner diameter.

3. Once the fatigue crack reached the inner diameter, the crack grew around the circumference of the tube.

4. The leading edge of the circumferential growth is nearly vertical, although the outer surface slightly leads the inner surface.

5. Microcracking is evident on the outer diameter with length less than 40 microns. The microcracking is perpendicular to the main fatigue crack and does not extend to the inner diameter. The inner diameter is free from microcracking.

6. The path of the fatigue crack can be seen to be tortuous. Although the crack itself is less than one mil in width, the entire crack varies from true perpendicular by approximately 6 to 8 mils.

D. Electrical-Discharge Machining

1. Introduction

As mentioned in Chapter one, electrical-discharge-machining (EDM) is a common method of obtaining defects similar to cracks for reference standards in nondestructive testing. H. J. Bowman [52] found that it was necessary to have a precise artificial notch as a standard for calibrating eddy current inspection equipment. EDM notches are generally used because they are relatively quick and easy to produce and can make small notches with widths generally around five mils, although some companies today have the ability to produce EDM notches as small 1.5 mils.

2. Principles of EDM

EDM is a metal removal process also known as spark erosion, spark machining or capacitor-discharge-machining. The process has been used in metal removal since 1906. EDM machines remove metal by discharging a series of short bursts of electrical energy into the workpiece in the presence of a dielectric oil in which the workpiece is immersed as shown in Figure 4.5.

There are a variety of factors which affect the type of EDM notch produced. Two of these factors are discussed by Zemberry [17].

i) Effect of Voltage Potential Between Workpiece and Electrode

The rate at which the electrode can be fed into the workpiece depends on the voltage between the workpiece and the electrode. Zembery showed that increasing the voltage produces a wider notch because a higher voltage will produce a larger overcut. This overcut is the space near the cutter filled with dielectric oil and eroded particles as shown in Figure 4.6.

ii) Effect of the EDM Process On Grain Structure

Zemberry also found that the heat generated during the EDM process does not significantly change or mechanically distort the grain structure of the workpiece. However, the EDM process does produce a thin recast surface. This recast surface is produced by the melting of the metal at the arc discharge points and the immediate resolidification of this mass by conduction of the heat away from the area by both the parent metal and the dielectric coolant. It is generally accepted that metal solidification leads to a lower conducting material [53]. The effect of this phenomenon on eddy current response is discussed in the next chapter.

E. EDM Experimental Preparation

A tanalum cutter of width 5 mils was used to produce the EDM notches in the stainless steel tubing. Although narrower cutters could have been used, generally they would tend to bend and produce unacceptable notches. The EDM notches were made transverse to the axis of the tube as shown in Figure 4.7. This

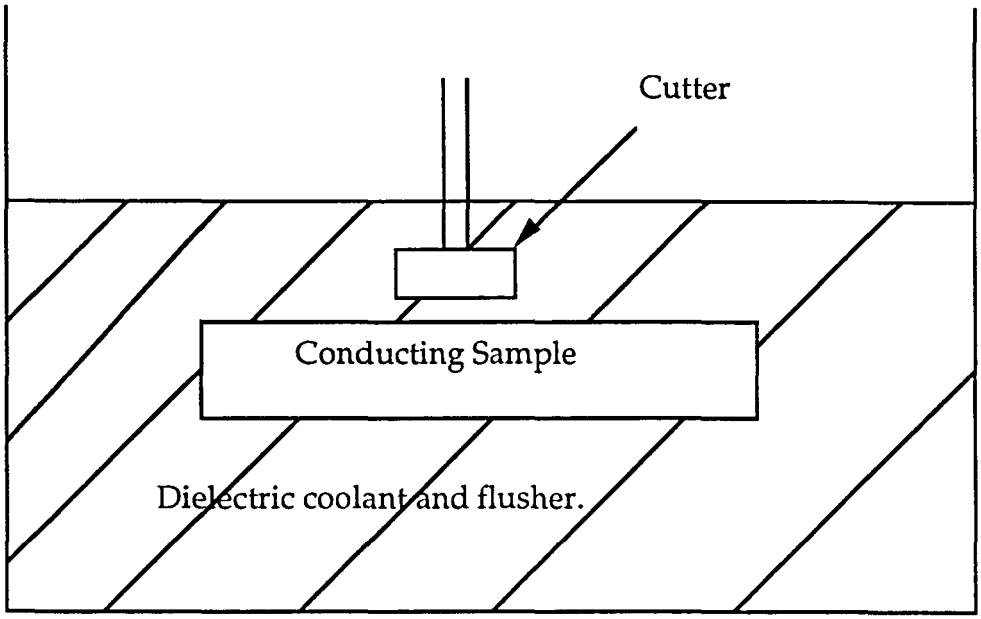

Figure 4.5. Diagram of EDM system.

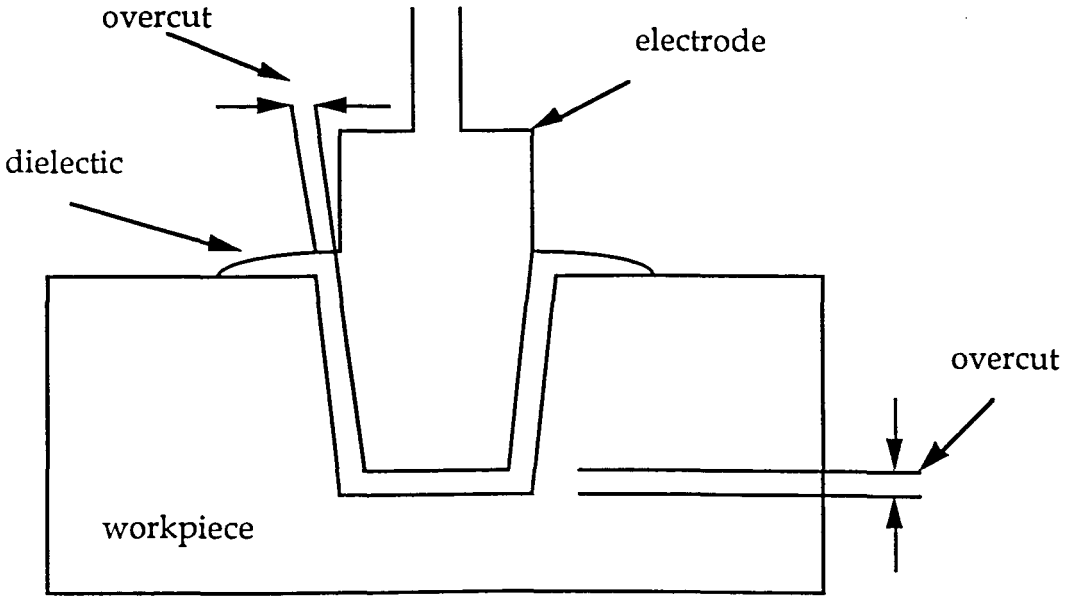

Figure 4.6. Workpiece overcut.

was done so that the EDM notches could be modeled with the finite element code and so that they would be as close as possible to the shape of the actual fatigue cracks.

A photograph of an EDM notch is shown in Figure 4.8 (a) from which a few points can be noted. First, the width of the notch is approximately 8 mils, although it should be noted that by increasing the speed of the cut, later EDM notches were produced with widths as small as 6.5 mils. Second, the notch is straight while the fatigue crack had a tortuous path. Third, a noticeable region of solidified material is evident on either side of the notch. The width of this region is approximately one or two mils. Fourth, there is no microcracking around the EDM notch region. In the fatigue cracks shown in Figure 4.3 there were large amounts of microcracking on the outer diameter of the tube. Figure 4.8 (b) shows a side view of the EDM notches which brings out the features caused by the spark-erosion, melting and resolidification of the metal.

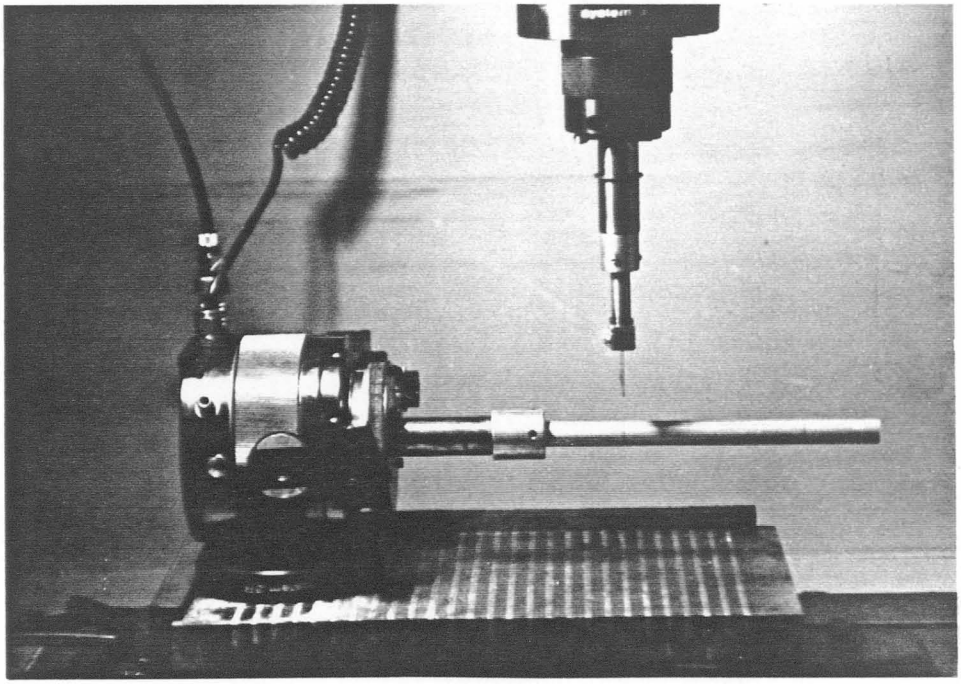

Figure 4.7. Orientation of EDM cutter with tube.

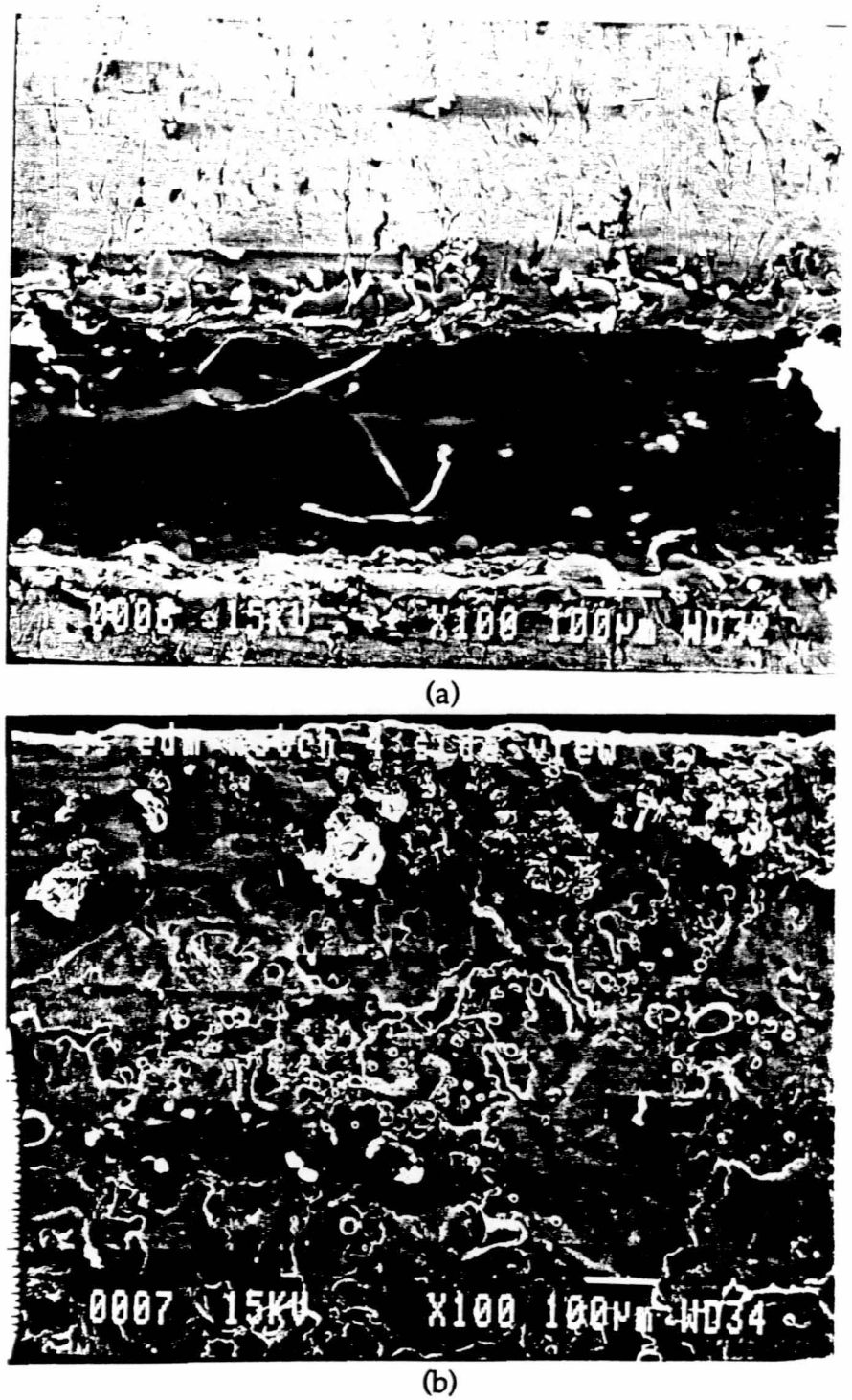

(a)

(b)

Figure 4.8. (a) Top view of EDM notch (100X). (b) Side view of EDM notch (100X).

F. Experimental Setup

A photograph of the experimental setup used in this research is shown in Figure 4.9 with a diagram shown in Figure 4.10. A Zetec MIZ-17 impedance analyzer was used to view eddy current responses in the form of impedance plane trajectories (IPTs). A 600 KHz Zetec differential probe with outer diameter 0.33" and coil radius 0.0625" was used for the 7/16" outer diameter stainless steel tubing. A diagram of the probe and tubing dimensions is shown in Figure 4.11. The motion of the probe was controlled by a PC21 motion control unit and an Electocraft DC motor. A Hewlett Packard 380 PC was used with an A/D converter for data collection. The collected data could then be sent to a laser printer for a hard copy.

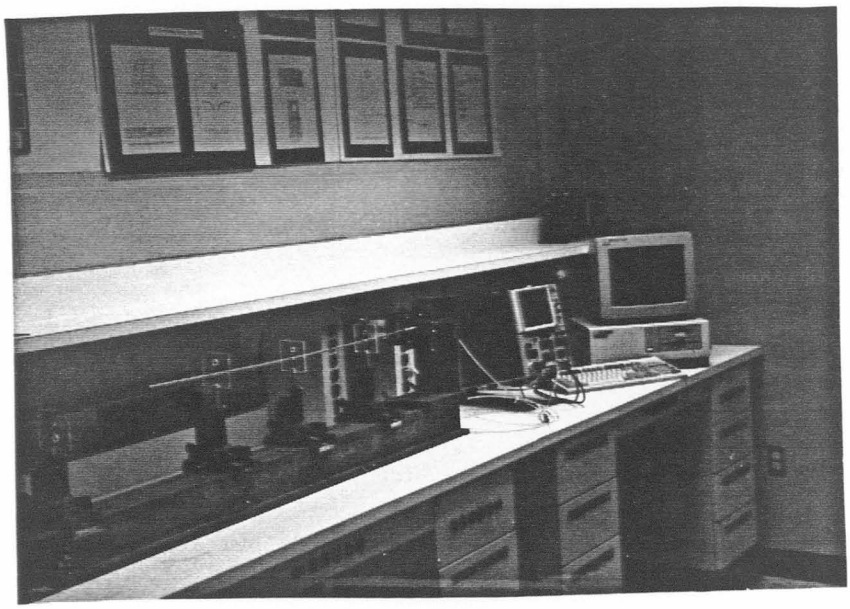

Figure 4.9. Photograph of experimental setup.

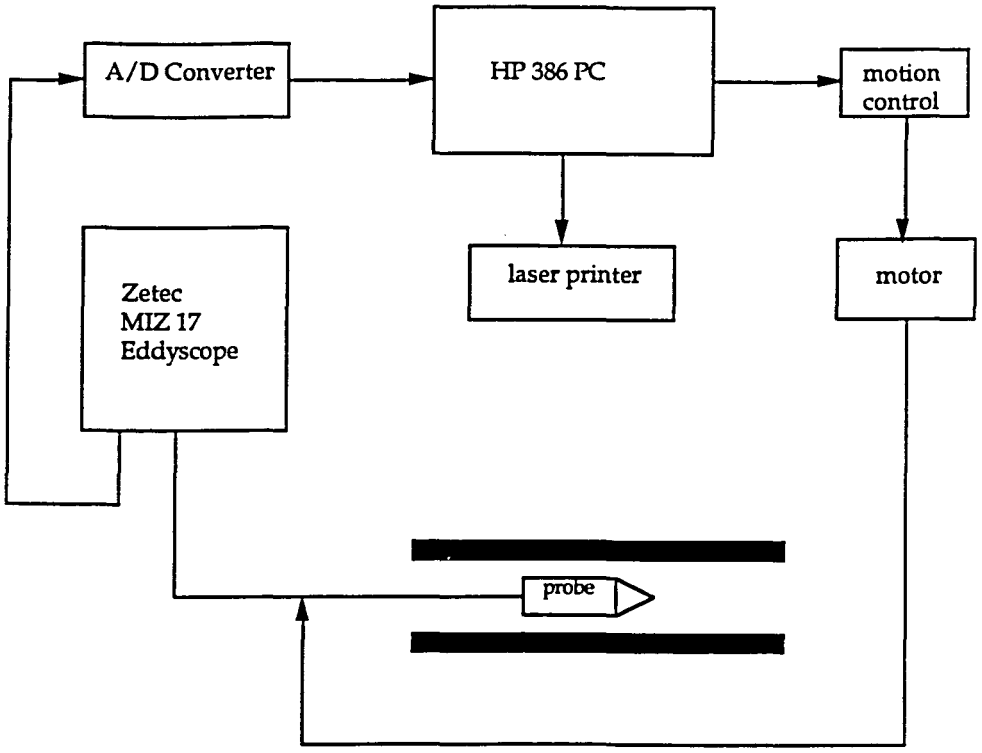

Figure 4.10. Block diagram of experimental setup.

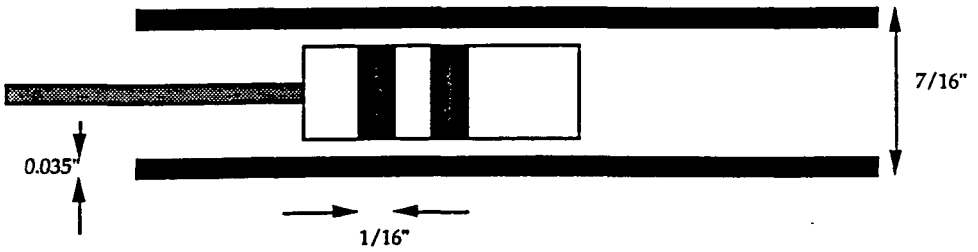

Figure 4.11. Dimensions of differential probe and stainless steel tubing.

CHAPTER 5. RESULTS

A. Introduction

This chapter presents results from the experimental and numerical procedures described in earlier chapters. The results from the eddy current responses are presented as impedance plane trajectories (IPTs). All experimental results were taken from the Zetec MIZ-17 eddyscope. The finite element results were all normalized with a uniform multiplication constant.

B. Experimental Results

1. Fatigue Crack Growth

Figure 5.1 shows the IPTs of a fatigue crack that is growing around the circumference of a stainless steel tube. The first measurement was taken with the length of the fatigue crack as 1/8" and the last was taken with the fatigue crack at 9/16". The width of the fatigue crack is approximately 0.0005" (12.5 microns). The growth of the crack was around the circumference of the tube as described in chapter four. The distortion in the IPTs is due to the deformation of the tube from the collet, which interfered with the actual fatigue crack signal. Figure 5.2 shows the IPTs of another fatigue crack growing around the circumference of the tube. The IPTs are again somewhat distorted from the collet deformation. The IPTs can be seen to grow in constant phase with both fatigue cracks. This phenomenon was observed for many other fatigue cracks, although

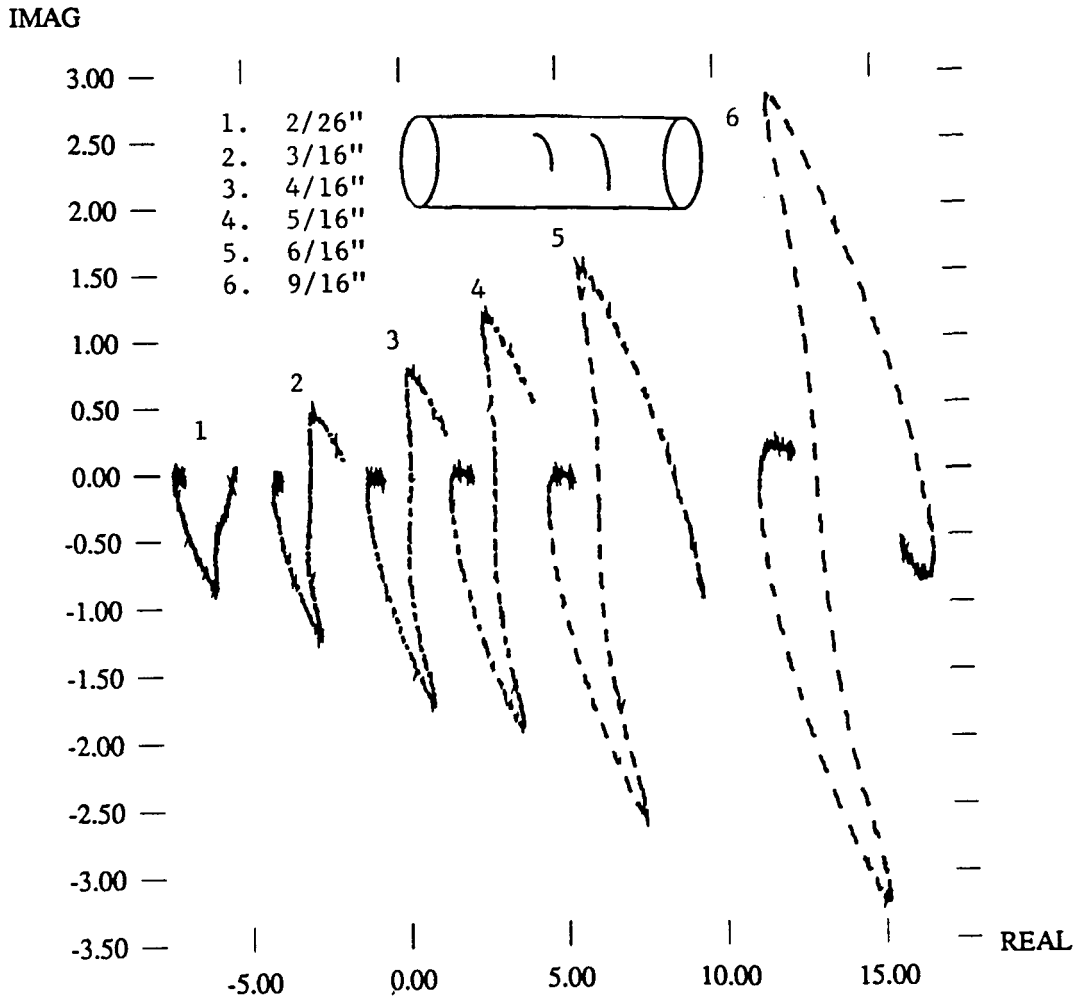

Figure 5.1. IPTs of fatigue crack growing around the circumference of the stainless steel tube.

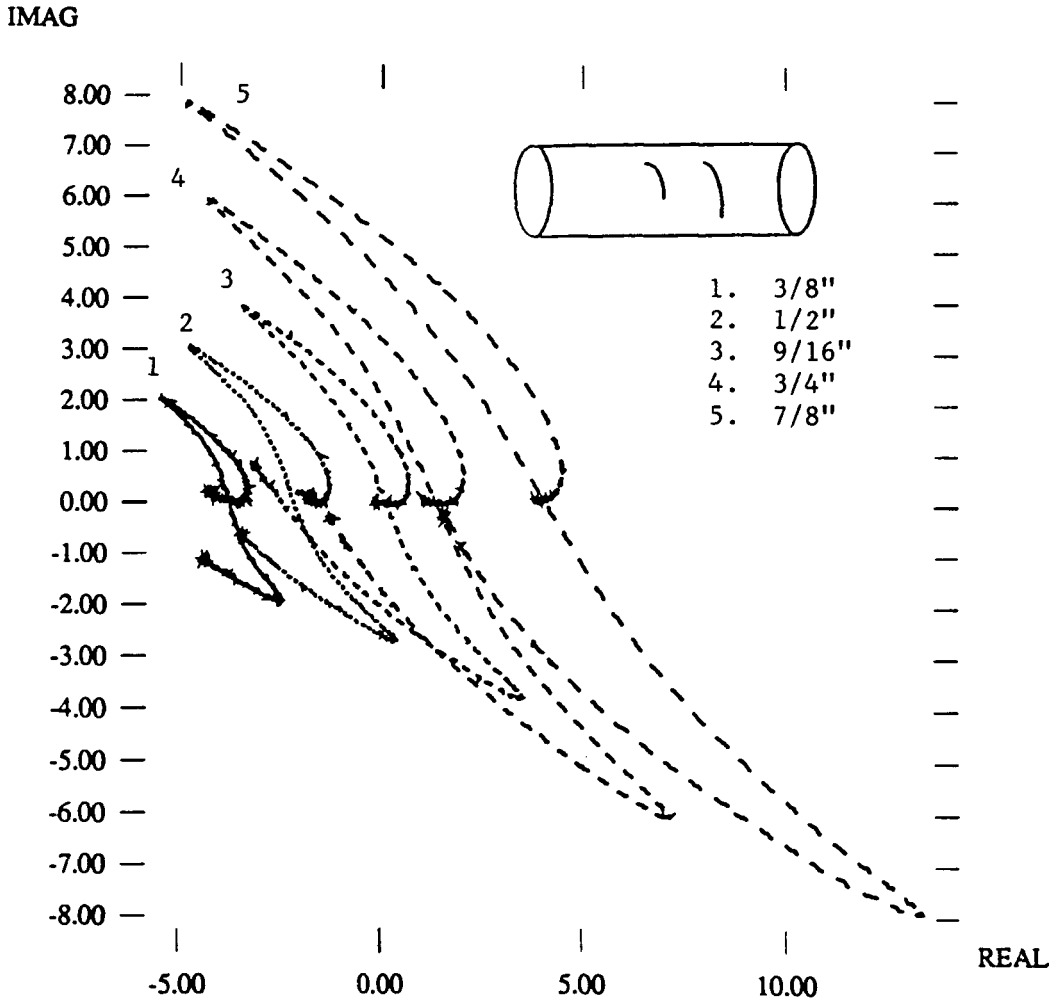

Figure 5.2 IPTs of fatigue cracks growing around circumference of tube.

the results are not presented here. Since it is generally accepted that the phase of an IPT changes with depth, it can be assumed the the fatigue crack was through the wall of the tube when the first measurement was taken.

2. EDM Notch Growth

Figure 5.3 shows the IPTs of EDM notches cut transverse to the axis of the stainless steel tube. Once again the measurement shown is the length around the circumference of the tube. The EDM notches are 0.008" wide and range in length from 9/32" to 7/8" around the circumference. The IPTs grow in constant phase except for the smallest IPT which is shifted slightly to the right. This implies that the EDM notches were completely through the wall of the tube as early as the second cut. Note that the signals are symmetric in this case because of the absence of collet damage.

3. Comparison of EDM Notches to Fatigue Cracks

Figure 5.4 shows a comparison between an EDM notch and a fatigue crack each with a length of 7/8" around the circumference of the tube. The IPTs compare very well, which is a somewhat surprising result, primarily because the EDM notches are much wider than the fatigue cracks. Also, according to Buck [53], the resolidifcation around the EDM notch can be considered to have a lower conductivity. To investigate this phenomenon, a thru-wall axisymmetric notch with width 0.006" was modeled with the two-dimensional finite element code. Another identical notch was modeled with a layer of resolidification material

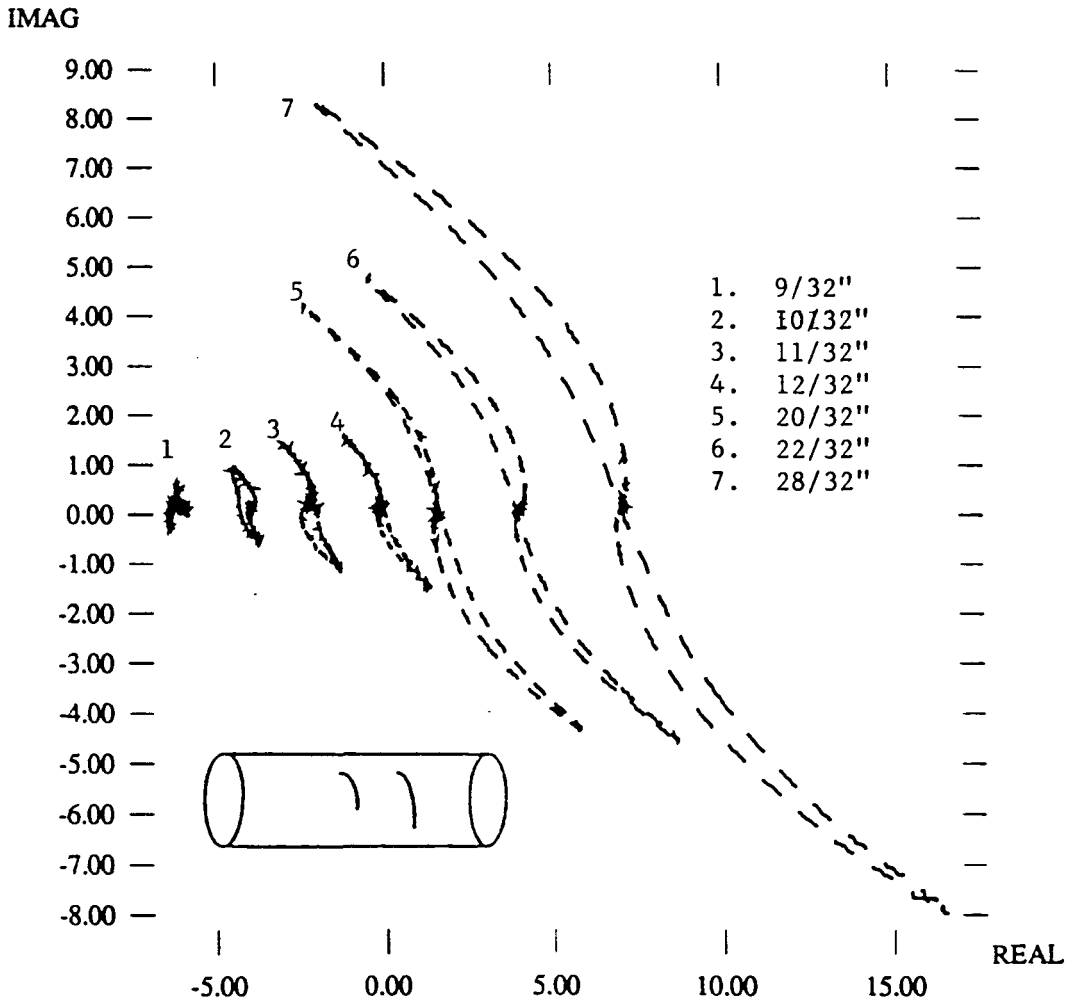

Figure 5.3. IPTs of EDM notch growth around the circumference of tube.

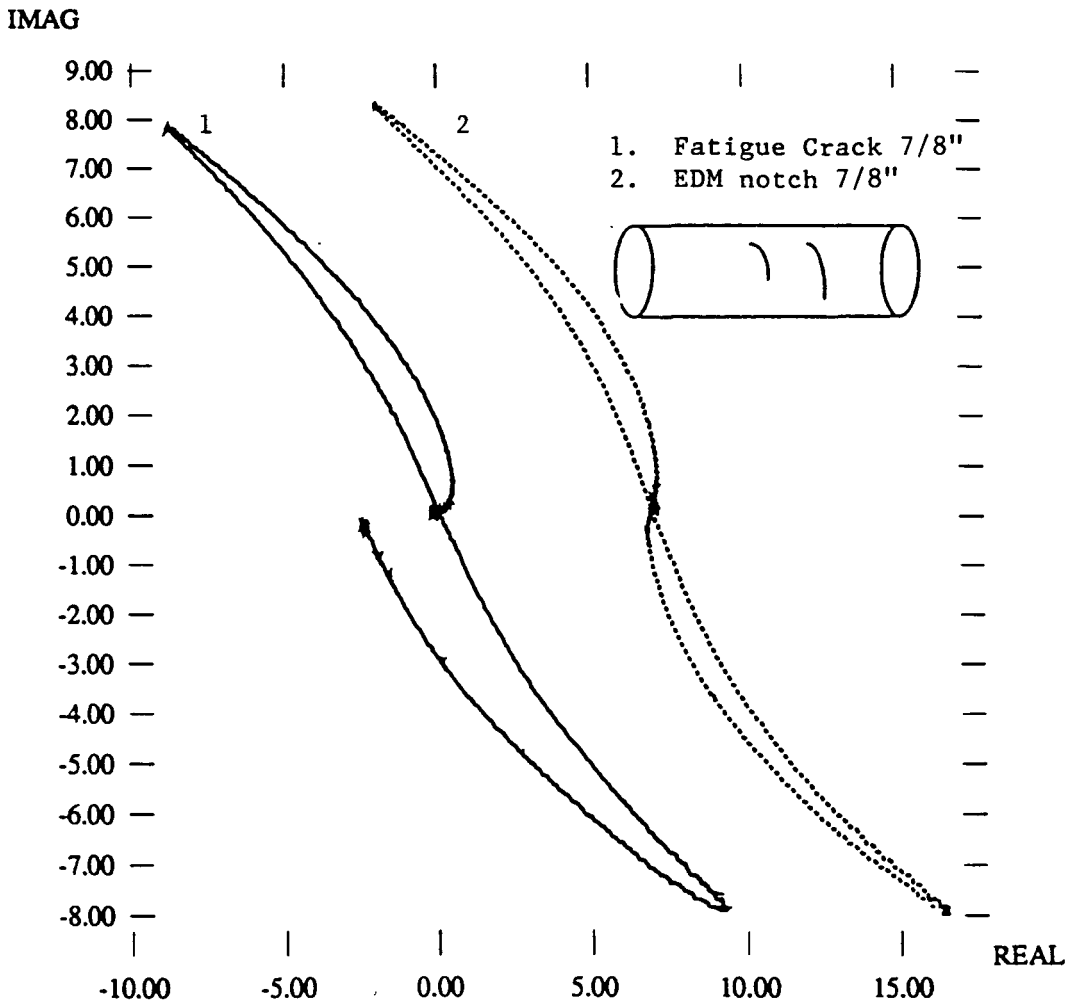

Figure 5.4. Comparison of EDM notch IPT and fatigue crack IPT.

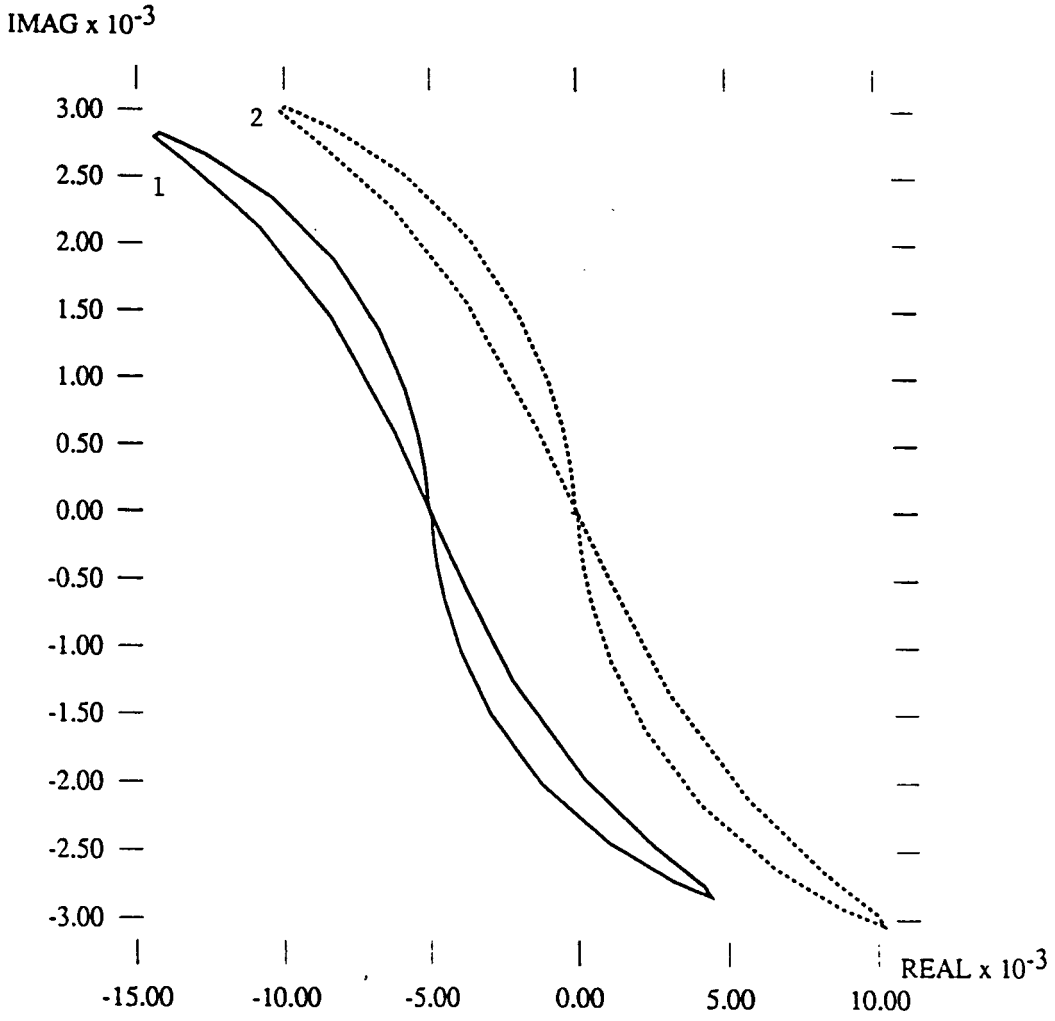

Figure 5.5. IPTs from (1) notch with width 0.0065" (2) notch with width 0.0065" and resolidification region with width 0.0015" on both sides of notch.

0.0015" wide on each side of the notch. The conductivity of the resolidification region was 10% lower than the rest of the tube. Figure 5.5 shows the results of the study. We can see that the resolidification causes an increase an IPT magnitude. Thus, an EDM notch can be expected to give a larger response than a crack of equal width. The effect of fatigue on conductivity has not been studied extensively to the author's knowledge, although, Buck [54] suggests that fatigue might cause a slight decrease in conductivity of the material.

C. Finite Element Results

Next, some results from the finite element model are presented. First, since the mesh used for the smallest defect has an aspect ratio of 8:1, a study of the effects of aspect ratio on IPT is presented. Figure 5.6 shows the IPTs from axisymmetric notches with width of 0.024". The IPTs have aspect ratio of 1:1, 4:1 and 8:1. From the figure one can see that the aspect ratio does not have a significant effect on the modeled response up to 8:1. The study did show, however, that making the aspect ratio larger than 8:1 causes the IPT to become quite distorted.

Figure 5.7 shows the IPTs from axisymmetric notches with width of 0.004". The depth of each notch is carried from 60% thru-wall to 100% thru-wall. It can be seen that there is a large variance in phase with change in depth as would be expected. Figure 5.8 shows IPTs of constant 80% thru-wall depth and varying width. The width of the axisymmetric notch varies from 0.002" to 0.014". The IPTs can be seen to grow in constant phase, just as was seen with the

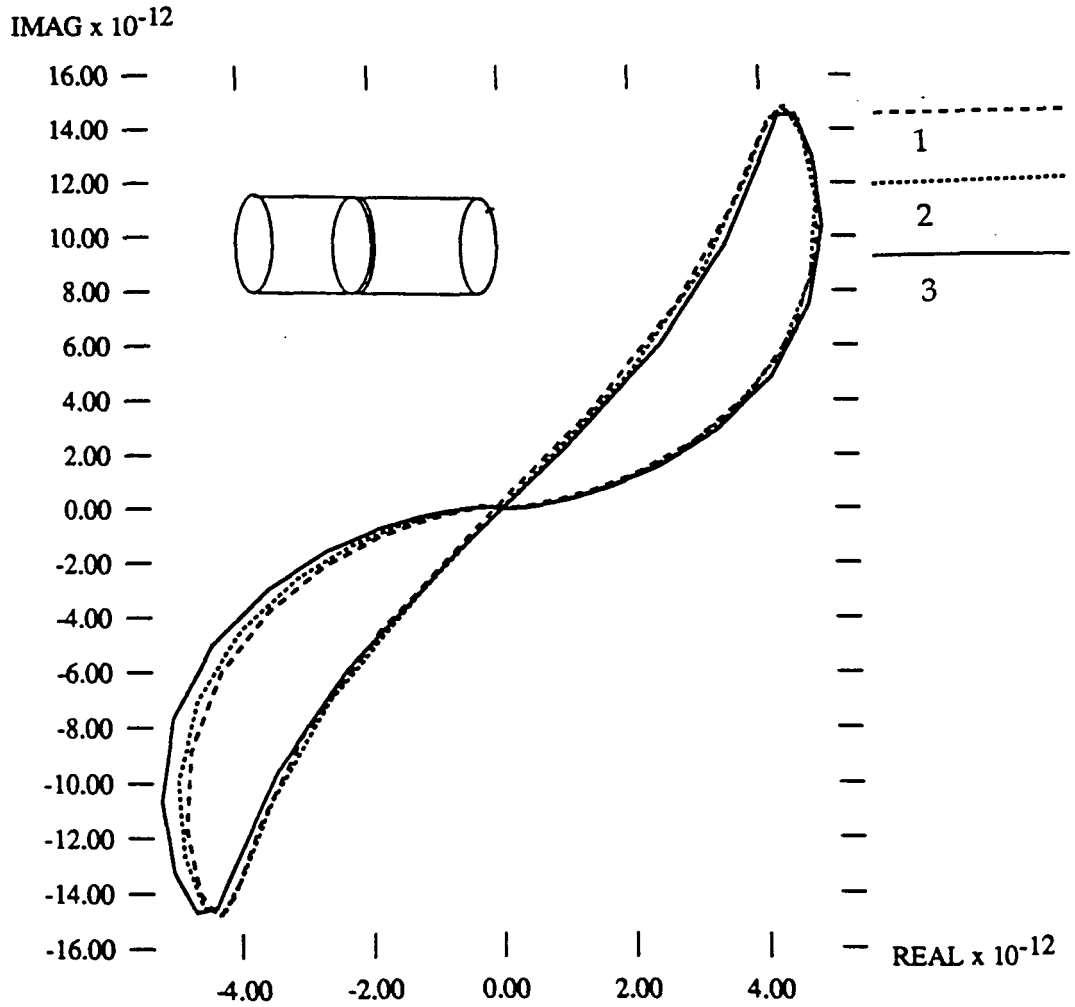

Figure 5.6. IPTs of axisymmetric notch with mesh aspect ratio (1) 1:1, (2) 4:1, and (3) 8:1.

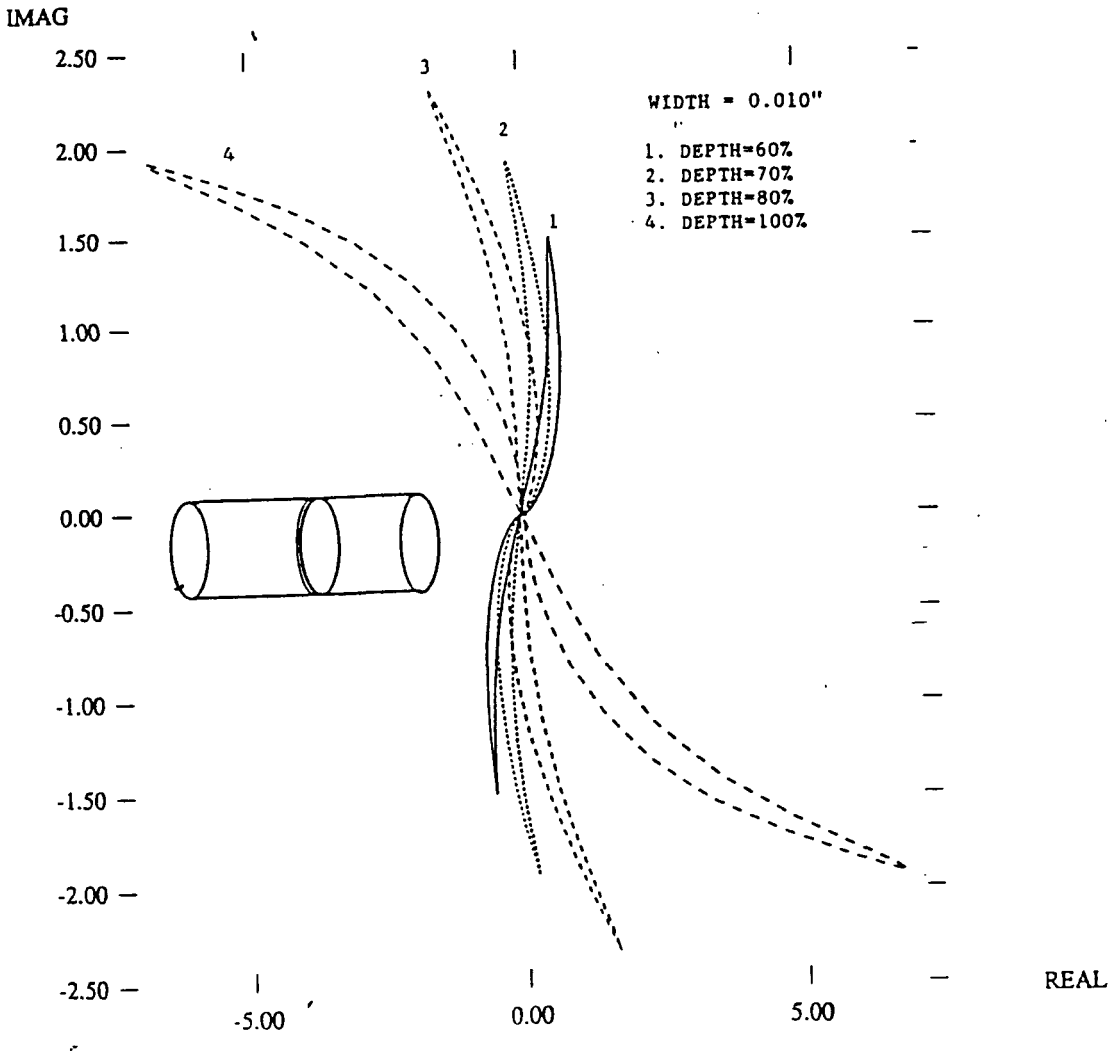

Figure 5.7. IPTs of axisymmetric notches with constant width and varying depth.

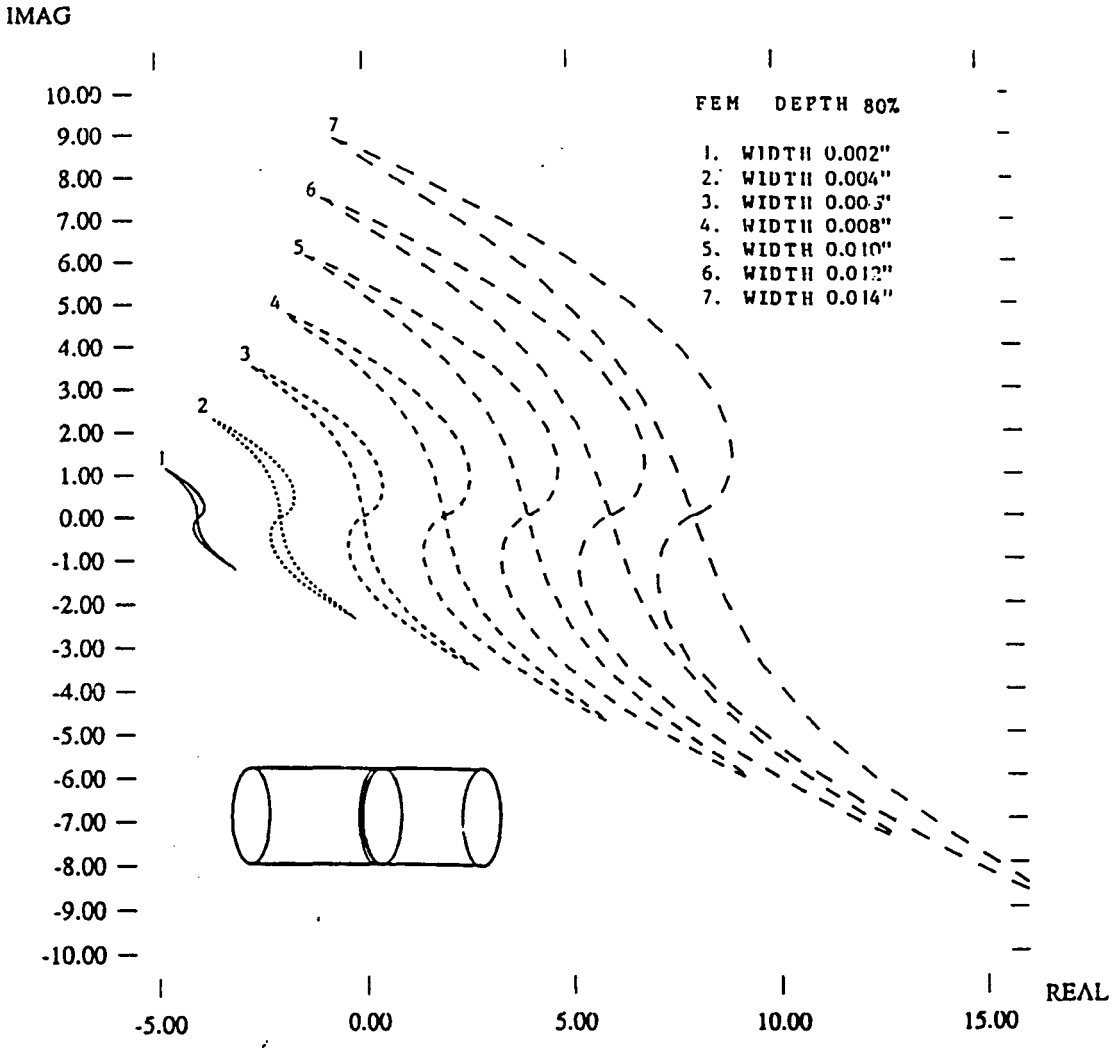

Figure 5.8. IPTs of axisymmetric notches with constant depth and varying width.

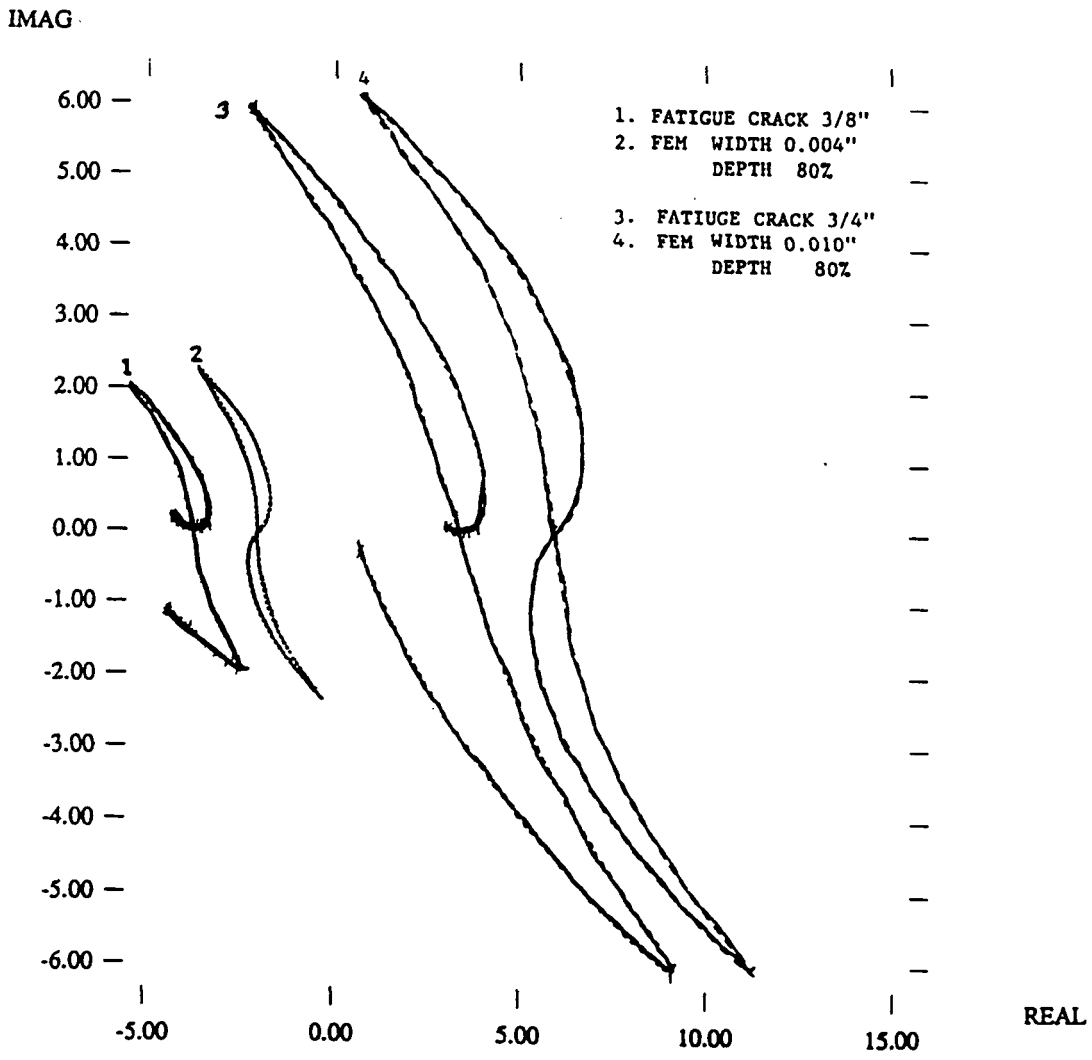

Figure 5.9. A comparison of axisymmetric FEM notch and fatigue crack.

experimental results from the growing fatigue cracks and EDM notches. Figure 5.9 shows a comparison of IPTs from fatigue cracks and the finite element model. It can be seen that by keeping the depth constant at 80% thru-wall and varying the width of the notch, the finite element model simulates the fatigue cracks very closely.

D. Further Results

After these results were completed, it was learned that the EDM notches could be made narrower by making the cut at a faster speed. The cut width could be reduced from 0.008" to approximately 0.0065" which would be significant in simulating the response from the fatigue cracks. Figure 5.10 shows the response from two EDM notches, each with length of 5/8" around the circumference of the tube. The larger IPT is from the wider notch. A good comparison can be seen between the decrease in width shown in the finite element model and the decrease in width of the EDM notches.

Next, these narrower EDM notches are compared to fatigue crack responses. Figure 5.11 shows IPTs from a fatigue crack and an EDM notch of length 5/8" inch. The fatigue cracks are again about 0.0001" wide and the EDM notches are 0.0065" wide. Figure 5.12 shows IPTs from a fatigue crack of length 9/16" and an EDM notch of length 10/16" with width the same as the previous figure. From the figures it can be seen that the EDM notches consistently give smaller IPTs than the fatigue cracks even though the fatigue cracks are much narrower than the EDM notches.

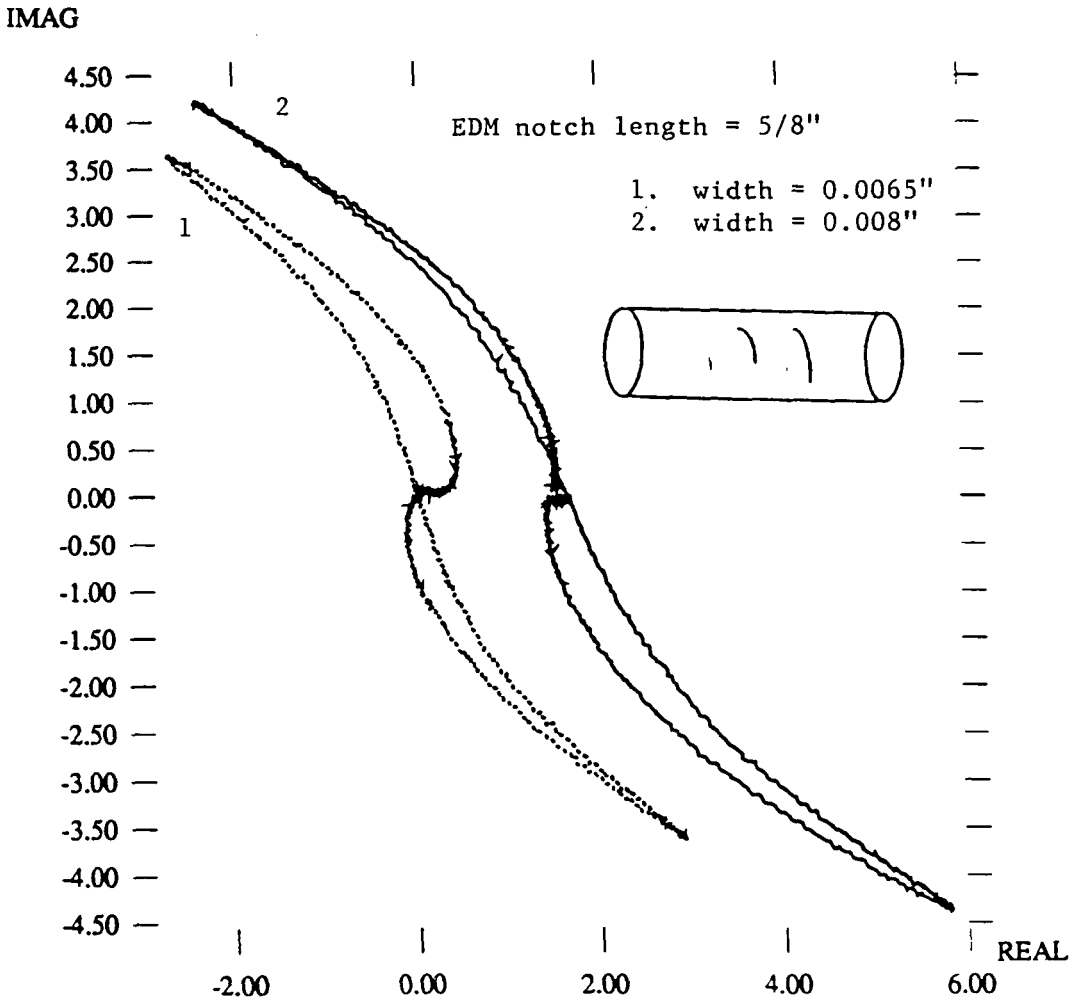

Figure 5.10. IPTs of EDM notches with varying width.

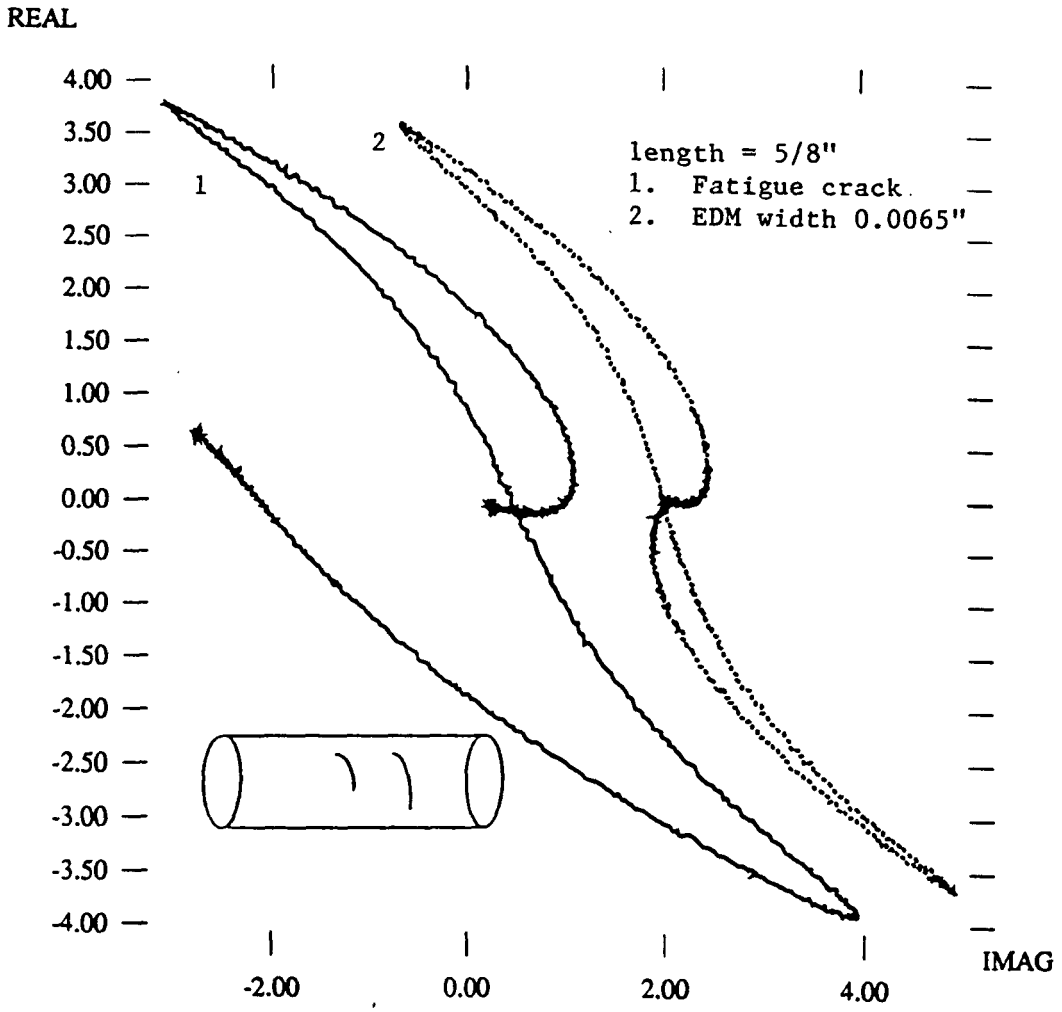

Figure 5.11. IPTs of fatigue crack and EDM notch with width of 0.0065".

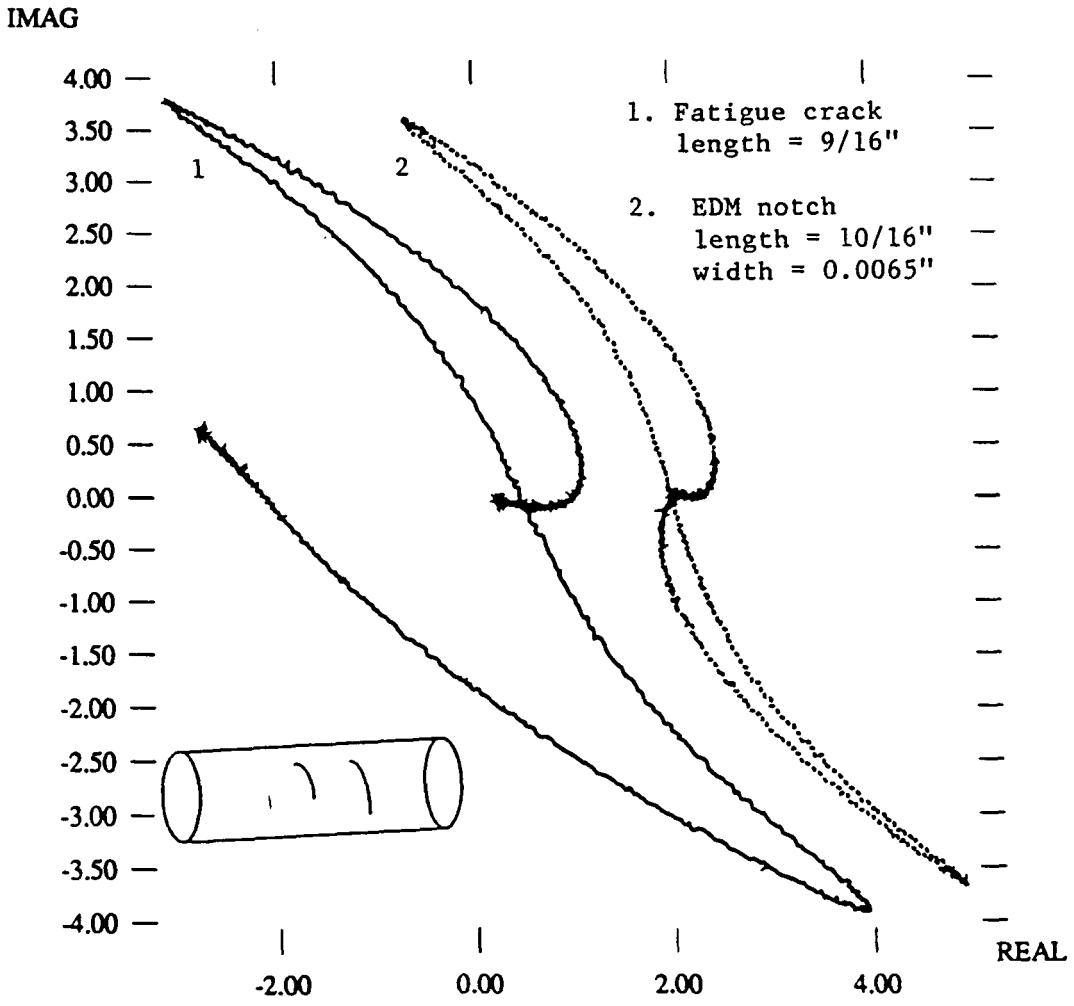

Figure 5.12. IPTs of fatigue crack and EDM notch with width 0.0065".

E. Results From Weighted Conductivity FEM

As described in Chapter 2, the weighted conductivity approach of modeling an infinitesimally narrow crack involves treating the conductivity over an element as a function of a triangular shape function. To first test this method, the original 36x121 mesh with element width 0.012" was used. All elements along the crack region shown in Figure 5.13 were given weighted conductivity. The value of conductivity for each shaded element is zero on the crack node, one at all other nodes, with linear variance between nodes. By using linear conductivity weighting functions over two element columns, we would expect to get a response similar to that from a thru-wall notch with zero conductivity over one column. This is because the total area of conductivity from both regions would be equal. Figure 5.14 shows the IPTs from a notch modeled with zero conductivity one element wide compared to the IPT from a crack modeled with the weighted conductivity model using the shaded elements of Figure 5.13. From Figure 5.14 it can be seen that the two IPTs compare very closely. Figure 5.15 is identical to Figure 5.14 except the IPTs are from a crack with depth 50% of the wall thickness.

Next, the minimum amount of element nodes along the crack element are used as shown in Figure 5.16. Figure 5.17 shows a comparison of IPTs from the smallest thru-wall notch in the original 36x121 mesh with element width of 0.012", a thru-wall notch using the weighted conductivity approach and the elements of Figure 5.16, and a thru-wall notch of width 0.0015" from the 36x968 mesh with aspect ratio 8:1. It can be seen that the IPT of a crack from the

weighted conductivity approach compares very well to an IPT of a crack from a much finer mesh. Figure 5.18 shows the magnetic vector potential $\overline{A}$ plot from a notch one 0.012" element wide with thru-wall depth. This plot shows that the magnetic vector potential is continuous as should be expected. Also, it can be seen that there is a slight different between the fields of the coil under the crack and the coil in the defect free region. Figure 5.19 shows the magnetic vector potential $\overline{A}$ plot from the weighted conductivity approach using the elements of Figure 5.16. Once again the potential contours are continous, however, the difference in fields from the coils is too small to be noticed here. This is because the simulated defected is very small and does not cause much field disruption. These field plots help to verify the validity of the weigted conductivity approach. Thus, it is possible to simulate a much finer mesh using this approach.

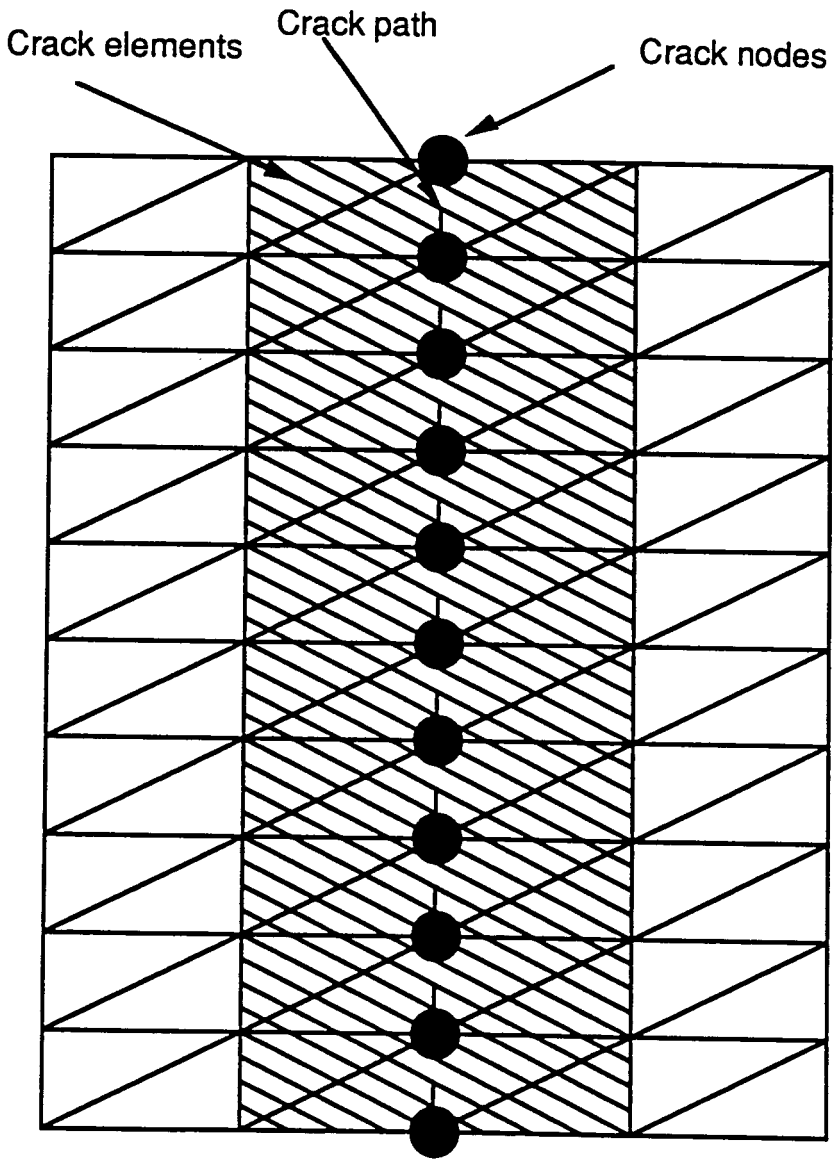

Figure 5.13. Elements used with weighted conductivity FEM.

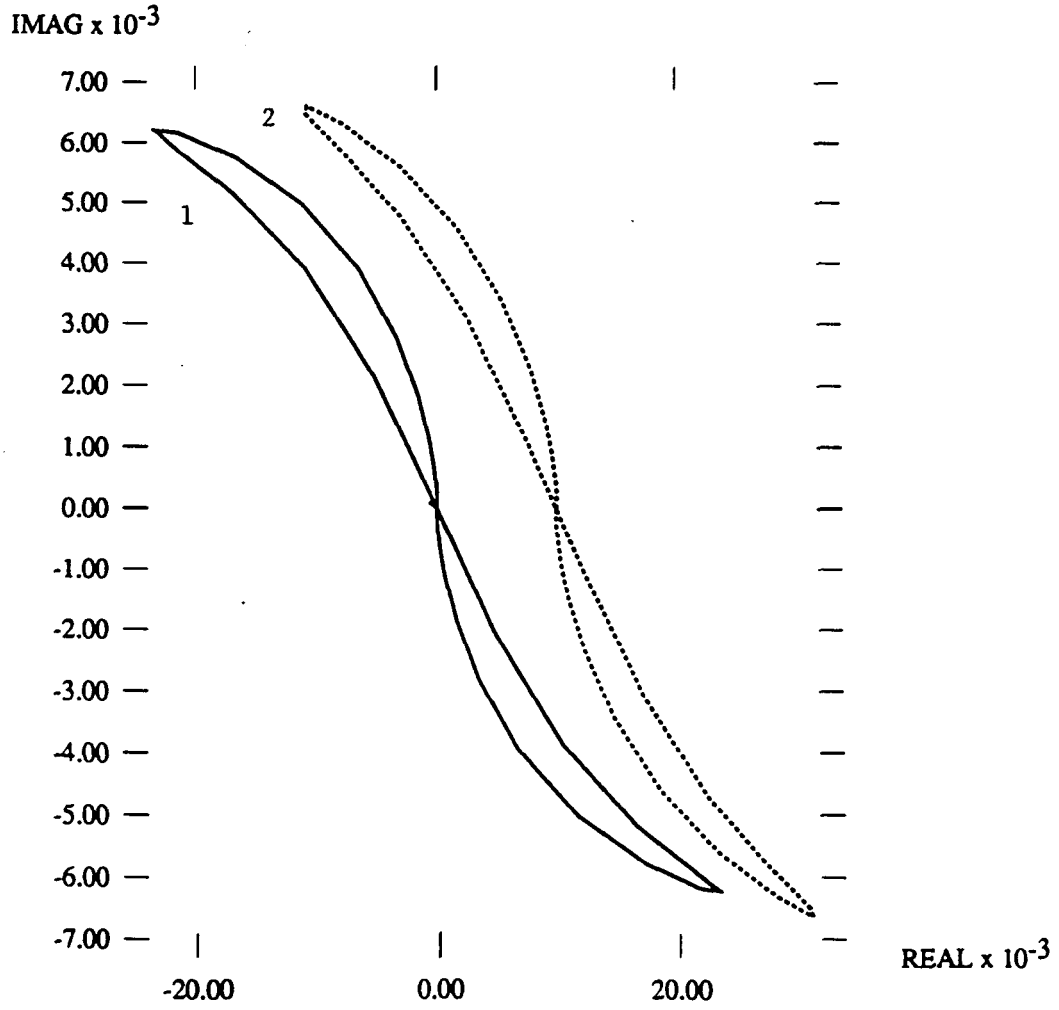

Figure 5.14. IPTs from (1) FEM axisymmetric thru-wall notch one element wide, (2) axisymmetric notch using weighted conductivity FEM.

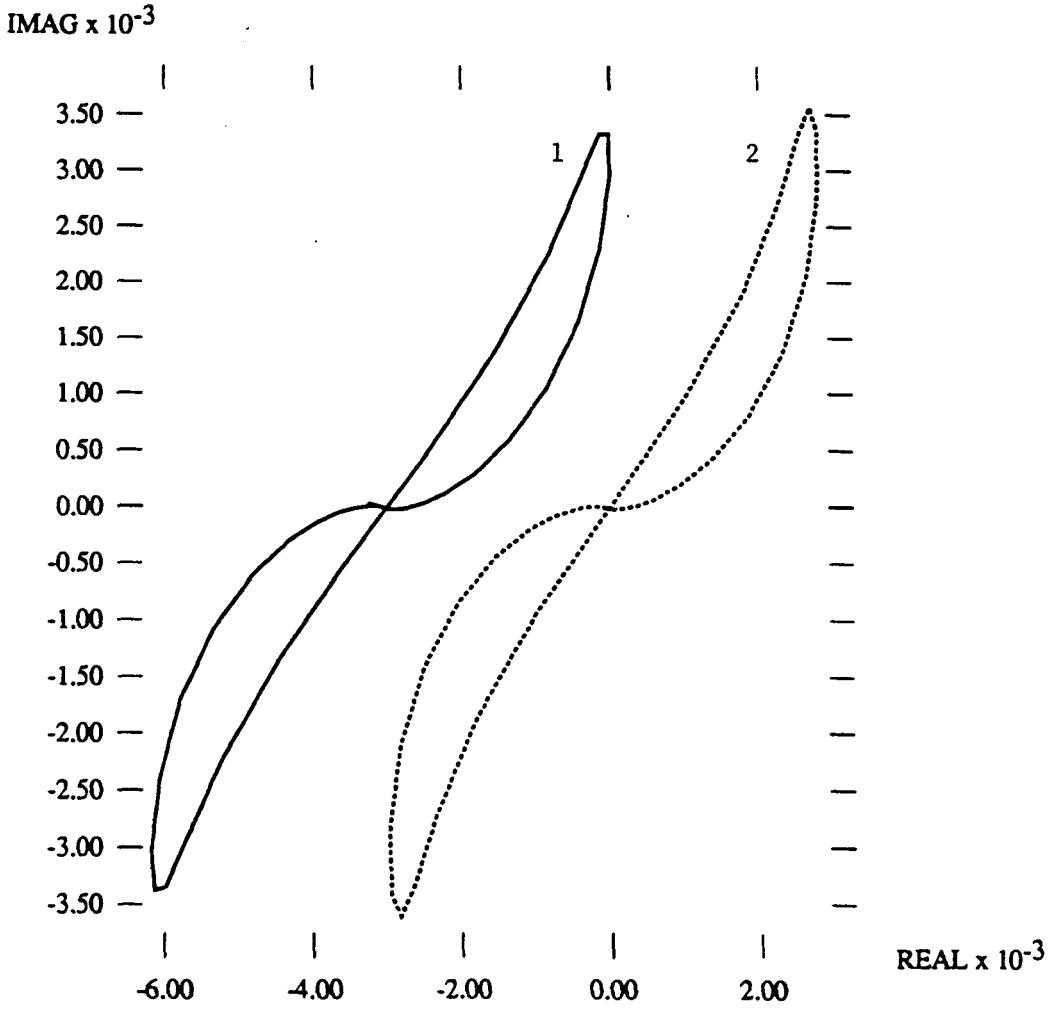

Figure 5.15. IPTs from (1) FEM 50% thru-wall axisymmetric notch one element wide, (2) 50% thru-wall axisymmetric notch using weighted conductivity FEM.

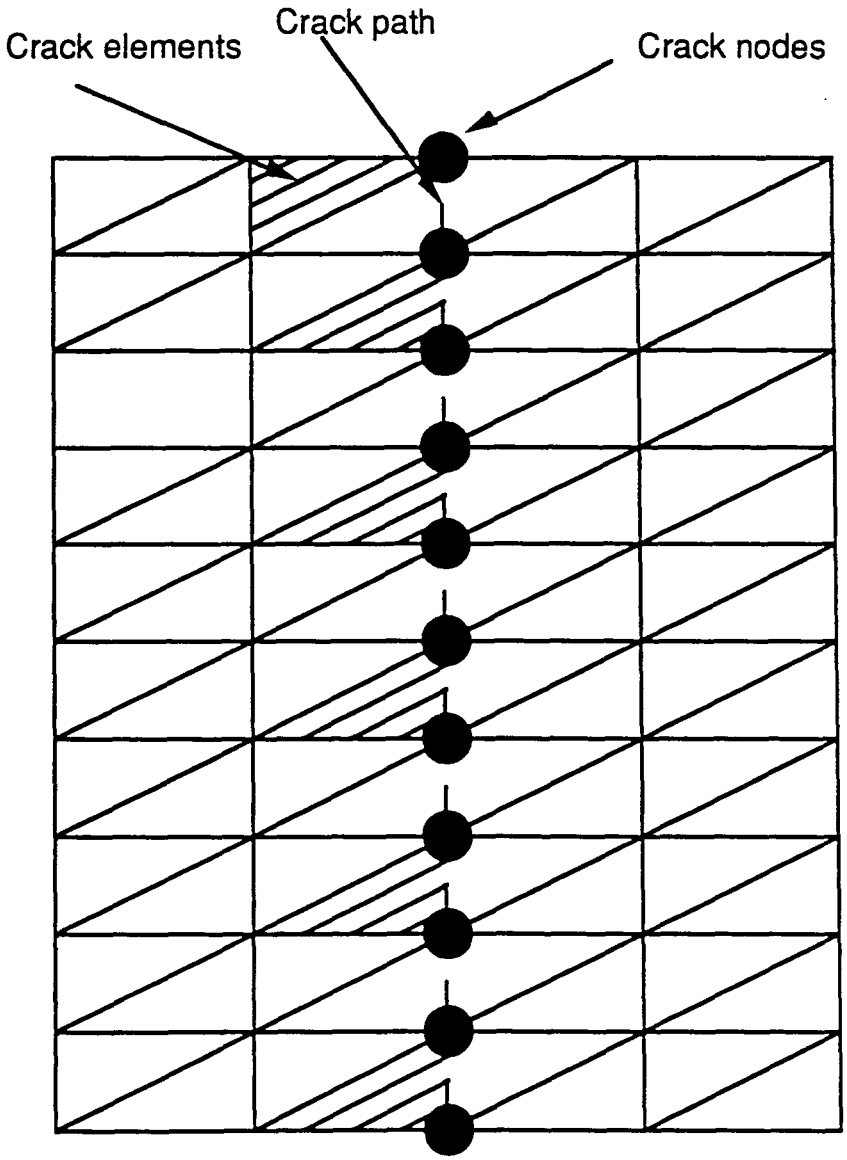

Figure 5.16. Elements used for smallest crack with weighted conductivity FEM.

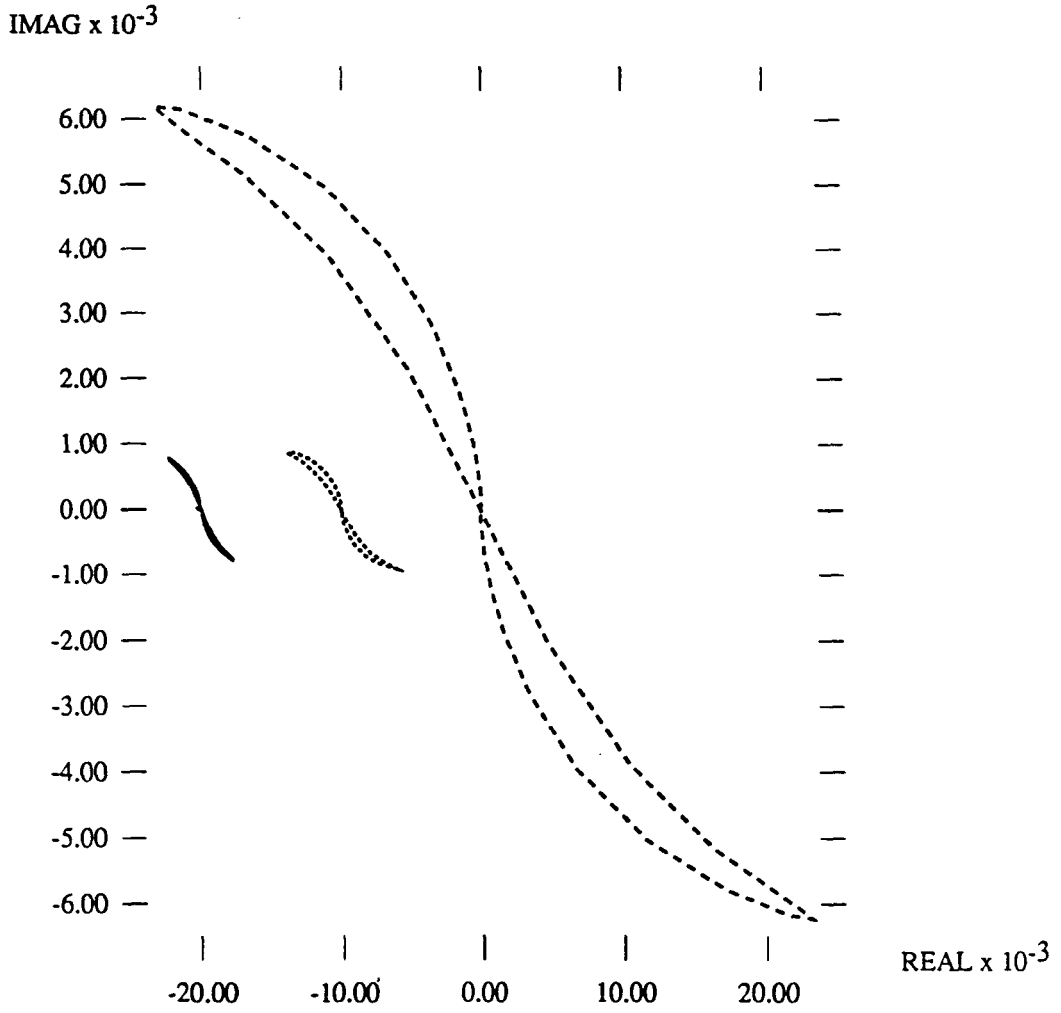

Figure 5.17. IPTs axisymmetric thru-wall notch (1) one element (0.012") wide from original 121X36 mesh, (2) using mesh of Figure 5.16 with weighted conductivity FEM and element width 0.012", (2) one element (0.0015") wide from mesh with aspect ratio 8:1.

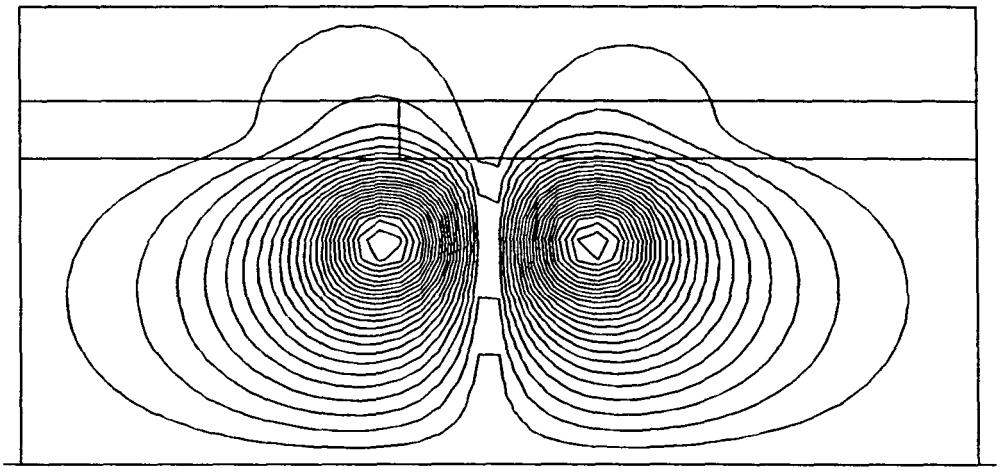

Figure 5.18. Plot of magnetic vector potential contours from a thru-wall notch one element wide with width 0.012".

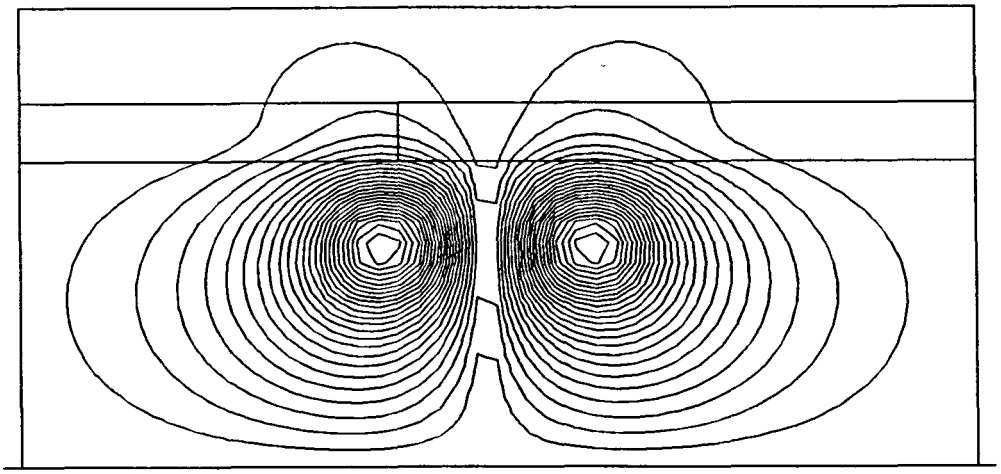

Figure 5.19. Plot of magnetic vector potential contours from a thru-wall notch using the the mesh of Figure 5.16 with weighted conductivity FEM and element width 0.012".

CHAPTER 6. SUMMARY

A. Discussion of Results

From the experimental results it can be seen that the fatigue cracks consistently gave larger IPTs than the EDM notches. This is surprising since the fatigue cracks have a width of approximately 0.0001", while the EDM notches are a minimum of 0.0065" and the EDM notches contain a resolidification region which tends to increase the signal. However, as mentioned in Chapter 4, the fatigue cracks produced in the stainless steel tubing had very tortuous growth paths. Though the width of the crack was only 0.0005", the entire crack path traversed a total width of around 0.008". It is widely known that a defect transverse to the direction of eddy currents produces a much larger signal than one which is parallel to the eddy currents. Thus, the larger than expected response from the fatigue cracks can be assumed to be due to the large total width of the crack path. Thus, when creating a reference standard for a fatigue crack, the type of crack produced is very important information to know in advance. Factors such as microcracking and fatigue crack path should be taken into account when the reference standard is produced. For instance, if a reference crack was made from a tortuous fatigue crack as produced here, it would be unlikely that it would be a reliable standard for a fatigue crack with a straight growth path.

It was also seen that an axisymmetric finite element model can be used to model eddy current responses from three-dimensional circumferential fatigue

cracks. Also, a method was introduced in which a small crack can be modeled with a relatively coarse mesh.

B. Future Work

Future work in this area would include more work with fatigue using better fatigue equipment. This would include equipment which could monitor fatigue growth and detect the presence of a fatigue crack much earlier than is possible with the human eye. Also, it would be very useful to be able to monitor the crack with an eddy current probe as the fatigue crack is growing. It would also be beneficial to use fatigue equipment which could produce longitudinal and circumferential fatigue cracks with growth paths ranging from straight to very tortuous. To accompany this it would also be useful to make EDM notches using rigid graphite blades with widths of approximately 0.001" or less. This would enable the researcher to investigate fatigue cracks and the type of reference standard needed for a particular fatigue crack.

Future finite element work would definitely include using a three-dimensional model for the fatigue crack responses. It would be beneficial to implement the three-dimensional code on a parallel supercomputer if possible. It would also be interesting to investigate the weighted conductivity approach of modeling infinitesimally narrow cracks with a three dimensional code. One major application of this method would be cracks with points of closure along the crack region.

REFERENCES

[1] McMaster, R.C., Nondestructive Testing Handbook, Vol. I, American Society for Nondestructive Testing, Inc., Columbus, Ohio, 1959.

[2] Quong, H., "SSME Heat Exchanger Coil Weld Nondestructive Inspection Review," BC 87-32, NASA Langley, 1987.

[3] Metals Handbook, Vol 11, Nondestructive Inspection and Quality Control, American Society For Metals, Metals Park, Ohio, 1976.

[4] Holt, R.C., "Eddy Current Testing of Small Diameter Tubing," Proceeding of the Third Annual Symposium On Nondestructive Testing of Aircraft and Missile Components, Western Periodicals Co., San Antonio, Texas, 1962.

[5] Rao, B. Shyamsunder, M., Kalyanasundaram, P., Bhattacharya, D. and Baldev, R., "Development of Eddy Current Test Techniques For Condition Monitoring of Pressure Tube/Calandria Tube Assemblies of Indian Pressurised Heavy Water Reactors," British Journal of NDT, Vol 33, No. 9, September, 1991, p. 437.

[6] Baker, R.A.. and Tombaugh, R.S., "Eddy Current Examination of Heat-Exchanger Tubing with Inside-Surface Pitting," Materials Evaluation, Vol. 48, Jan., 1990, p. 55.

[7] McMaster, R.C., Nondestructive Testing Handbook, Vol. II, American Society for Nondestructive Testing Inc., Columbus, Ohio, 1959.

[8] Libby, H., Introduction to Electromagnetic Nondestructive Test Methods, Krieger Publishing Co., New York, 1979.

[9] Office of the Assistant Secretary of Defense, Electromagnetic Testing (For Inspection of Material, Department of Defense, United States of America, 1965.

[10] Capobianco, T.E. and Ciciora, S.J., "Characterizing Differential Air-Core Eddy Current Probes," Review of Progress in Quantitative Nondestructive Evaluation, Vol. 10A, edited by D.O. Thompson and D.E. Chimenti Plenum Press, New York, 1989, p. 897.

[11] Cecco, V.S. and Van Drunen, G., "Recognizing the Scope of Eddy Current Testing," Research Techniques in Nondestructive Testing, Vol. VIII, edited by R.S. Sharpe. Academic Press, London, 1985.

[12] Verite, J.C., "A Coil Over A Crack. (Results For Benchmark Problem 8 of Team Workshop)," COMPEL-The International Journal for Computation and Mathematics in Electrical and Electronic Engineering, James and James Science Publishers Ltd., London, 1990, Vol. 9, No. 3, p155-167.

[13] Hagemaier, D.J., "Application of Eddy Current Impedance Plane Testing," Materials Evaluation, Vol. 42, July, 1984, p. 1035.

[14] Hagemaier, D.G., "Supplemental Inspections of Aging Aircraft," Materials Evaluation, Vol. 44, July, 1986, p. 989.

[15] Silk, M.G., Whapham, A.D. and Hobbs, C.P., "The Need for Defect Monitoring," Nondestructive Testing (Proc. 12th World Conference), edited by J. Boogaard and G.M. van Dijk, Elsevier Science Publisher B.B., Amsterdam, 1989.

[16] McClung, R.W., "ASTM Nondestructive Testing Standards Program," Nondestructive Testing Standards-A Review, edited by Harold Berger, American Society for Testing and Materials, Philadelphia, Pa., 1976.

[17] Zemberry, W.L., "Control Factors for Electrical-Discharge-Machined Reference Standards," Materials Evaluation, Vol. 28, January, 1970, p.81.

[18] Borman, R., "Cut Surface Quality-the pluses and minuses of EDM," Machining Source Book, ASM International, Metals Park, Ohio, 1988.

[19] Feil, J.M., "Eddy-Current Testing of Thin Nonferromagnetic Plate and Sheet Materials Using a Facsimile-Recording Data Display Method," Eddy-Current Characterization of Materials and Structures, , ASTM, Philadelphia, Pa., 1976.

[20] Doctor, P.G., et. al., "Pattern Recognition Methods for Classifying and Sizing Flaws Using Eddy Current Data," Eddy Current Characterization of Materials and Structures, ASTM, Philadelphia, Pa. 1976.

[21] Brown, C.L., et. al., "Automatic Detection, Classification, and Sizing of Steam-Generator Tubing Defects by Digital Signal Processing," Eddy

Current Characterization of Materials and Structures, ASTM, Philadelphia, Pa., 1976.

[22] Randle, W.R. and Woody, B.D., "Caution About Simulated Cracks In Steel For Eddy Current Testing," Materials Evaluation, Vol. 49, January, 1991, p. 277.

[23] Hartman, J., "Correlation of Eddy Current Response From EDM Notches and Tight Fatigue Cracks In Ferromagnetic Space Shuttle RSRM Components," Review of Progress in QNDE, Vol. 10A, opsit, 1991, p. 285.

[24] Hagemaier, D.A. and Register, J.A., "Mock Eddy Current Demonstration: Cracks Versus Notches," Materials Evaluation, Vol. 48, January, 1990, p. 50.

[25] Rummel, W.D., Moulder, J.G. and Nakagawa, N., "The Comparative Response of Cracks and Slots In Eddy Current Measurements," Review of Progress In QNDE, Vol. 10A, opsit, 1991, p. 277.

[26] Lord, W., "Applications of Numerical Field Modeling To Electromagnetic Methods of Nondestructive Testing," IEEE Transactions On Magnetics, Vol. MAG-19, No. 6, November, 1983, p. 2437.

[27] Lord, W. and Palanisamy, R., "Development of Theoretical Models for NDT Eddy Current Phenomena," Eddy Current Characterization of Materials and Structure, opsit, 1981, p. 5.

[28] Lord, W., "Prototype Eddy Current SSME Heat Exchanger Tubing Inspection System," NASA Interim Report, October, 1990.

[29] Ciarlet, P.G. and Lions, J.L., Handbook of Numerical Analysis, North-Holland Publishing, New York, 1991.

[30] Hildebrand, F.B., Introduction To Numerical Analysis, McGraw-Hill Book Company, New York, 1974.

[31] Isaacson, E. and Keller, H.B., Analysis of Numerical Methods, John Wiley and Sons, New York, 1966.

[32] Zienkiewicz, O.C., The Finite Element Method, McGraw-Hill Book Company, New York, 1977.

[33] Norrie, D.H. and Vries, G., The Finite Element Method, Academic Press, New York and London, 1973.

[34] Bickford, W.B., A First Course in the Finite Element Method, Irwin, Boston, 1990.

[35] Clough, R.W. "The Finite Element Method In Plane Stress Analysis," Proceeding 2nd ASCE Conference on Electronic Computation, Pittsburgh, PA. 1960.

[36] Oden, J.T. and Somogyi, D., "Finite Element Applications In Fluid Dynamics," Journal Engineering Mechanics Division, ASCE 95 (EM 4), 1968, p821-826.

[37] Lord, W., "Numerical Modeling of Electromagnetic NDT Phenomena," New Procedures in Nondestructive Testing (Proceedings), Edited by P. Holler, Springer-Verlag, Heidelberg, 1983.

[38] Lord, W. and Hwang, J.H., "Finite Element Modeling of Magnetic Field/Defect Interactions," ASTM Journal of Testing and Evaluation, Vol. 3, No. 1, January, 1975, p. 21-25.

[39] Lord, W. and Hwang, J.H., "Defect Characterization From Magnetic Leakage Fields," British Journal of Nondestructive Testing, Vol. 19. No. 1, January, 1975, p 14-18.

[40] Palanisamy, R. and Lord, W. "Finite Element Analysis of Eddy Current Phenomena," Materials Evaluation, Vol. 38, 1980, p. 39-43.

[41] Lord, W. and Palanisamy, R., "Finite Element Modeling of Electromagnetic NDT Phenomena," IEEE Transactions On Magnetics, Vol. MAG-15, No. 6, November 1979.

[42] Palanisamy, R., "Finite Element Eddy Current NDT Model," Ph.D. Dissertation, Colorado State University, 1980.

[43] Nath, S.N., "Remote Field Eddy Current Phenomena,", M.S. Thesis, Colorado State University, 1988.

[44] Gramz, M., et. al., "A Crack Element Concept For A FEM Analysis Of Eddy Current Distribution In A Long Cylindrical Bar With A Crack," Nondestructive Testing (Proc. 12th World Conference), opsit, 1989, p. 1035.

[45] Frost, N. E., Marsh, K. J., and Pook, L. P., Metal Fatigue, Clarendon Press, Oxford 1974.

[46] Suresh, S., Fatigue of Materials, Cambridge University Press, Cambridge, 1991.

[47] Bannantine, J.A., Comer, J.J. and Handrock, J.L., Fundamentals of Metal Fatigue Analysis, Prentice-Hall, Englewood Cliffs, New Jersey, 1990.

[48] Laird, C., "Mechanisms and Theories of Fatigue," Fatigue and Microstructure, American Society for Metals, Metals Park, Ohio, 1978.

[49] Fine, M.E., Ritchie, R.O., "Fatigue-Crack Initiation and Near-Threshold Crack Growth," Fatigue and Microstructure, American Society for Metals, Metals Park, Ohio, 1978.

[50] Starke, E. and Lutjering, G., "Cyclic Plastic Deformation and Microstructure," Fatigue and Microstructure, American Society for Metals, Metals Park, Ohio, 1978.

[51] Haworth, W., Singh, V., and Mueller, R., "Holographic Detection of Fatigue-Induced Surface Deformation and Crack Growth in a High Strength Aluminum Alloy," Metallurgical Transactions, 11A, 1980, p. 219-229.

[52] Bowman, H.J., " A Standard For Eddy Current Test," Metal Progress, July, 1962, p. 78.

[53] Siegfried, R.M., Wallace, J.P., Boser, G.A., Kunerth, D.C., "Quantitative Models for Eddy Current Analysis of Metal Solidification," Nondestructive Evaluation: Microstructural Characterization and Reliability Strategies, Edited by Otto Buck and Stanley M. Wolf, The Metallurgical Society of AIME, Warrendale, Pennsylvania, 1980.

[54] Buck, O., Schumbacher, D., and Seeger, A., "Electrical Resistivity Study of Lattice Defects Formed During Plastic Deformation of Copper Single Crystals," Physica Status Solidi (B), 60, 1973, p. 707-720.